



NAVAL POSTGRADUATE SCHOOL

MONTEREY, CALIFORNIA

DISSERTATION

**TRANSPORT IMAGING OF SPATIAL DISTRIBUTION OF
MOBILITY-LIFETIME ($\mu\tau$) PRODUCT IN BULK
SEMICONDUCTORS FOR NUCLEAR RADIATION
DETECTION**

by

David J. Phillips

June 2012

Dissertation Supervisor:

Nancy M. Haegel

Approved for public release; distribution is unlimited

THIS PAGE INTENTIONALLY LEFT BLANK

REPORT DOCUMENTATION PAGE			Form Approved OMB No. 0704-0188	
Public reporting burden for this collection of information is estimated to average 1 hour per response, including the time for reviewing instruction, searching existing data sources, gathering and maintaining the data needed, and completing and reviewing the collection of information. Send comments regarding this burden estimate or any other aspect of this collection of information, including suggestions for reducing this burden, to Washington headquarters Services, Directorate for Information Operations and Reports, 1215 Jefferson Davis Highway, Suite 1204, Arlington, VA 22202-4302, and to the Office of Management and Budget, Paperwork Reduction Project (0704-0188) Washington DC 20503.				
1. AGENCY USE ONLY (Leave blank)		2. REPORT DATE June 2012		3. REPORT TYPE AND DATES COVERED Dissertation
4. TITLE AND SUBTITLE: Transport Imaging of Spatial Distribution of Mobility-Lifetime ($\mu\tau$) Product in Bulk Semiconductors for Nuclear Radiation Detection				5. FUNDING NUMBERS
6. AUTHOR(S): David J. Phillips				
7. PERFORMING ORGANIZATION NAME(S) AND ADDRESS(ES) Naval Postgraduate School Monterey, CA 93943-5000				8. PERFORMING ORGANIZATION REPORT NUMBER
9. SPONSORING / MONITORING AGENCY NAME(S) AND ADDRESS(ES) Department of Homeland Security (DHS)/Domestic Nuclear Detection Office (DNDO)				10. SPONSORING / MONITORING AGENCY REPORT NUMBER
11. SUPPLEMENTARY NOTES: The views expressed in this thesis are those of the author and do not reflect the official policy or position of the Department of Defense or the U.S. Government. I.R.P. Protocol number N/A.				
12a. DISTRIBUTION / AVAILABILITY STATEMENT Approved for public release; distribution is unlimited				12b. DISTRIBUTION CODE
13. ABSTRACT (maximum 200 words)				
<p>The objective of this research is to advance the development of a micro-analysis technique for characterizing the charge transport properties in bulk semiconductor materials for room temperature nuclear radiation detection. The technique is applied to bulk semi-insulating thallium bromide (TlBr) and cadmium zinc telluride (CZT) and uses a two-dimensional diffusion model and transport imaging to make rapid contact-free measurements of the magnitude and spatial variation in the mobility-lifetime ($\mu\tau$) product at 2 μm resolution. The $\mu\tau$ product is a key measure of charge transport, and a uniform $\mu\tau$ product is critical for optimum energy resolution in gamma ray detectors. Spatial variations in the ambipolar diffusion length are observed in TlBr on a scale of $\sim 10 \mu\text{m}$, and the cathodoluminescence (CL) spectrum in TlBr at 5 K is reported. Using CL and photo-induced conductivity transient spectroscopy (PICTS), an empirical energy level diagram for Se and Pb defect levels in TlBr is reported. The $\mu\tau$ product in TlBr is generally found to decrease with increasing impurities/defects. The $\mu\tau$ product in TlBr and CZT is found to decrease with increasing temperature over the ranges of 8 K – 102 K and 5 K – 60 K, respectively. Transport imaging is applied for the first time to investigate the effects of Te inclusions in CZT and the role of photon recycling in TlBr and CZT.</p>				
14. SUBJECT TERMS: Transport Imaging, Cathodoluminescence, Mobility-Lifetime ($\mu\tau$) Product, Thallium Bromide, TlBr, Cadmium Zinc Telluride, CZT, Spatial Variation				15. NUMBER OF PAGES 204
				16. PRICE CODE
17. SECURITY CLASSIFICATION OF REPORT Unclassified		18. SECURITY CLASSIFICATION OF THIS PAGE Unclassified		19. SECURITY CLASSIFICATION OF ABSTRACT Unclassified
				20. LIMITATION OF ABSTRACT UU

NSN 7540-01-280-5500

Standard Form 298 (Rev. 2-89)
Prescribed by ANSI Std. Z39-18

THIS PAGE INTENTIONALLY LEFT BLANK

Approved for public release; distribution is unlimited

**TRANSPORT IMAGING OF SPATIAL DISTRIBUTION OF MOBILITY-
LIFETIME ($\mu\tau$) PRODUCT IN BULK SEMICONDUCTORS FOR NUCLEAR
RADIATION DETECTION**

David J. Phillips
Lieutenant Colonel, United States Army
B.S., United States Military Academy, West Point, 1995
M.S., University of Massachusetts, Lowell, 2005

Submitted in partial fulfillment of the
requirements for the degree of

DOCTOR OF PHILOSOPHY IN PHYSICS

from the

**NAVAL POSTGRADUATE SCHOOL
June 2012**

Author:

David J. Phillips

Approved by:

Nancy M. Haegel
Distinguished Professor of Physics
Dissertation Supervisor

Craig F. Smith
Research Professor

Gamani Karunasiri
Professor of Physics

Christopher Frenzen
Professor of Mathematics

Sebastian Osswald
Assistant Professor of Physics and MAE

Approved by:

Andres Larraza, Chair, Department of Physics

Approved by:

Douglas Moses, Vice Provost for Academic Affairs

THIS PAGE INTENTIONALLY LEFT BLANK

ABSTRACT

The objective of this research is to advance the development of a micro-analysis technique for characterizing the charge transport properties in bulk semiconductor materials for room temperature nuclear radiation detection. The technique is applied to bulk semi-insulating thallium bromide (TlBr) and cadmium zinc telluride (CZT) and uses a two-dimensional diffusion model and transport imaging to make rapid contact-free measurements of the magnitude and spatial variation in the mobility-lifetime ($\mu\tau$) product at 2 μm resolution. The $\mu\tau$ product is a key measure of charge transport, and a uniform $\mu\tau$ product is critical for optimum energy resolution in gamma ray detectors. Spatial variations in the ambipolar diffusion length are observed in TlBr on a scale of $\sim 10\ \mu\text{m}$, and the cathodoluminescence (CL) spectrum in TlBr at 5 K is reported. Using CL and photo-induced conductivity transient spectroscopy (PICTS), an empirical energy level diagram for Se and Pb defect levels in TlBr is reported. The $\mu\tau$ product in TlBr is generally found to decrease with increasing impurities/defects. The $\mu\tau$ product in TlBr and CZT is found to decrease with increasing temperature over the ranges of 8 K–102 K and 5 K–60 K, respectively. Transport imaging is applied for the first time to investigate the effects of Te inclusions in CZT and the role of photon recycling in TlBr and CZT.

THIS PAGE INTENTIONALLY LEFT BLANK

TABLE OF CONTENTS

I.	INTRODUCTION.....	1
A.	NUCLEAR SECURITY THREATS.....	1
B.	DETECTION CHALLENGES.....	2
C.	MATERIALS PROBLEM.....	4
D.	RESEARCH METHOD AND GOALS	6
E.	PUBLICATIONS AND PRESENTATIONS.....	7
II.	RADIATION SPECTROSCOPY AND THE $\mu\tau$ PRODUCT.....	9
A.	GAMMA-RAY RADIATION SPECTROSCOPY	9
B.	MOBILITY-LIFETIME PRODUCT.....	9
C.	DETECTOR RESOLUTION AND CHARGE COLLECTION	10
D.	MOBILITY-LIFETIME PRODUCT MEASUREMENT TECHNIQUES.....	13
III.	TRANSPORT IMAGING	15
A.	EXPERIMENTAL SETUP	15
B.	MATHEMATICAL MODEL OVERVIEW	16
C.	BULK SAMPLE 2D MATHEMATICAL MODEL AND ASSUMPTIONS.....	19
	1. Mathematical Model.....	19
	2. Model Assumptions.....	22
D.	TRANSPORT IMAGING EXAMPLE	23
IV.	INITIAL INVESTIGATION OF BULK THALLIUM BROMIDE	27
A.	OVERVIEW OF THALLIUM BROMIDE.....	27
	1. Properties of TlBr	27
	2. Transport Imaging in High Resistivity TlBr	29
B.	CRYSTAL GROWTH.....	29
C.	GLOW DISCHARGE MASS SPECTROMETRY.....	30
D.	CATHODOLUMINESCENCE	31
E.	PHOTOLUMINESCENCE	33
F.	ENERGY DISPERSIVE X-RAY SPECTROSCOPY	36
G.	TIME-OF FLIGHT SECONDARY ION MASS SPECTROMETRY.....	37
H.	TRANSPORT IMAGING—TEMPERATURE DEPENDENCE	39
V.	THALLIUM BROMIDE SAMPLES ZRC0937-07 AND ZRC0937-08.....	45
A.	CRYSTAL GROWTH.....	45
B.	GLOW DISCHARGE MASS SPECTROMETRY.....	46
C.	CATHODOLUMINESCENCE	48
D.	PHOTOLUMINESCENCE	50
E.	TRANSPORT IMAGING	51
	1. Effects of Doping	51
	2. Spatial Variation in Diffusion Length and $\mu\tau$ Product	56

VI.	DEFECT STUDY IN SELENIUM AND LEAD-DOPED THALLIUM BROMIDE.....	61
A.	DEFECT LEVELS	61
B.	CRYSTAL GROWTH.....	61
C.	GLOW DISCHARGE MASS SPECTROMETRY.....	62
D.	CATHODOLUMINESCENCE	63
E.	DEEP LEVELS IN THALLIUM BROMIDE.....	64
F.	TRANSPORT IMAGING	67
VII.	INITIAL INVESTIGATION IN BULK CADMIUM ZINC TELLURIDE	71
A.	OVERVIEW OF CADMIUM ZINC TELLURIDE	71
B.	CATHODOLUMINESCENCE	72
C.	TRANSPORT IMAGING	74
1.	Temperature Studies	74
2.	Effects of Inclusions	81
VIII.	FUTURE WORK.....	87
A.	OVERVIEW OF FUTURE WORK.....	87
B.	PHOTON RECYCLING.....	87
C.	GENERATION VOLUME	93
D.	HIGH-INJECTION MODEL	97
IX.	CONCLUSION	101
	APPENDIX A. CL MAP	103
	APPENDIX B. CL SPECTRA	105
	APPENDIX C. INTENSITY DISTRIBUTION AND FIT	109
	APPENDIX D. SPATIAL DISTRIBUTION	139
	APPENDIX E. MONTE CARLO SIMULATIONS	169
	LIST OF REFERENCES.....	175
	INITIAL DISTRIBUTION LIST	183

LIST OF FIGURES

Figure 1.	Comparison of energy resolution for natural background using high purity germanium, thallium-doped sodium iodide, and plastic scintillators. After [13].	4
Figure 2.	Simulated gamma-ray peak with FWHM and centroid energy E_0 . After [20].	10
Figure 3.	Contribution to FWHM due to Fano noise (ΔE_F), electronic noise (ΔE_E), and charge collection (ΔE_C). After [20].	11
Figure 4.	Experimental set up for CL and transport imaging using the electron beam from the SEM and an external CCD array camera.	15
Figure 5.	System schematic for transport imaging using the electron beam from the SEM and an external CCD array camera.	16
Figure 6.	Summary of the semiconductor material geometries (nanowire, thin film, or bulk sample), SEM excitation modes (red dot \equiv spot mode, red line \equiv line mode), and models (1D, 2D, or 3D). Arrows indicate diffusion directions.	17
Figure 7.	(a) The SEM generates a line of excess charge carriers across the bulk sample. The bulk sample is modeled as a series of semi-infinite planes, labeled A through N. (b) For each plane, the line source is modeled as a delta function at depth z_0 below the surface. The carrier concentration $u(x)$ is determined for each point on the x-axis of the plane, labeled $x = a_1 \dots a_N$.	19
Figure 8.	(a) SEM line scan luminescence image of TlBr crystal. (b) Planar and (c) Oblique views of a 10 μm segment (25 pixels) of the recombination luminescence intensity distribution. The diffusion length information is contained in the intensity distribution perpendicular to the line scan, along the x -axis. (d) Normalized mean recombination luminescence intensity distribution for the TlBr crystal. (e) Data from right side of distribution from Figure 4(d) and best-fit line from least squares fitting to the model.	25
Figure 9.	GDMS results for TlBr sample 45-S10.	30
Figure 10.	Cathodoluminescence map (false color) of TlBr sample 45-S10. Intensity variations are observed on a scale of $\sim 10 \mu\text{m}$.	31
Figure 11.	CL spectrum for TlBr sample 45-S10 at 11 K.	32
Figure 12.	CL spectrum for TlBr sample 45-S10 at 295 K.	33
Figure 13.	PL spectrum at 10 K for TlBr sample 45-S10. The dashed lines indicated Gaussian fits to the peaks.	34
Figure 14.	CL and PL spectra of TlBr sample 45-S10.	35
Figure 15.	EDX map for (a) thallium and (b) bromine.	36
Figure 16.	EDX spectrum for TlBr sample 45-S10.	37
Figure 17.	TOF-SIMS mapping showing elemental distribution of (a) thallium prior to sputtering, (b) thallium after sputtering, (c) bromine prior to sputtering, and (d) bromine after sputtering.	38

Figure 18.	TOF-SIMS mapping showing elemental distributions Na, Ca, K, Cu, F, and Cl before and after sputtering.....	39
Figure 19.	Evaluation of effects of beam current on intensity distribution at 20.0 keV in TlBr sample 45-S10.	40
Figure 20.	Normalized mean intensity distributions for TlBr sample 45-S10 for temperatures between 8 K and 102 K.	41
Figure 21.	Fit to TlBr sample 45-S10 at 8 K shown on (a) linear and (b) logarithmic scale.....	42
Figure 22.	Temperature dependence of (a) diffusion length and (b) $\mu\tau$ product for TlBr sample 45-S10.	43
Figure 23.	(a) Na/Al/Ag doped TlBr crystal (ZRC0937-07) and (b) Cu/Fe/Zn doped TlBr crystal (ZRC0937-08). The head region of each crystal contains fewer impurities than the tail region.	46
Figure 24.	GDMS results for (a) Na/Al/Ag doped TlBr and (b) Cu/Fe/Zn doped TlBr crystal.	47
Figure 25.	CL map at 295 K of (a) slice A and (b) slice D of Na/Al/Ag doped TlBr and (c) slice A and (d) slice C of Cu/Fe/Zn doped TlBr.	48
Figure 26.	CL map for $\lambda = 460$ nm at 11 K of (a) slices A and (b) slice C of Cu/Fe/Zn doped TlBr.	49
Figure 27.	(a-d) CL and (e-f) PL spectra for Na/Al/Ag doped TlBr and Cu/Fe/Zn doped TlBr.	50
Figure 28.	Comparison of the normalized mean recombination luminescence intensity distribution for (a) slices A and D of the Na/Al/Ag doped TlBr crystal, and (b) slices A and C of the Cu/Fe/Zn doped TlBr crystal. Note that the figures are plotted on a logarithmic scale to highlight small changes in the distributions.....	51
Figure 29.	Data and least squares fitting to the model for (a) (a) slices A and D of the Na/Al/Ag doped TlBr crystal, and (b) slices A and C of the Cu/Fe/Zn doped TlBr crystal.....	52
Figure 30.	Intensity distributions on different slices (A, C, or D) for random locations (L1, L2, or L3) for (a) Na/Al/Ag doped and (b) Cu/Fe/Zn doped TlBr crystals at 5 K.	53
Figure 31.	Diffusion lengths from different slices (A, C, or D) for random locations (L1, L2, and/or L3) for (a) Na/Al/Ag doped and (b) Cu/Fe/Zn doped TlBr crystals at 5 K.	54
Figure 32.	Diffusion lengths and one standard deviation from different slices (A, C, or D) for random locations (L1, L2, or L3) for (a) Na/Al/Ag doped and (b) Cu/Fe/Zn doped TlBr crystals at 5 K.	54
Figure 33.	(a) SEM area luminescence scan of $60\text{ }\mu\text{m} \times 85\text{ }\mu\text{m}$ region of slice C of the Cu/Fe/Zn doped TlBr crystal. Intensity variations are visible on a scale of $\sim 10\text{ }\mu\text{m}$. The location of a $40\text{ }\mu\text{m}$ line scan is indicated by the white line. (b) SEM line scan, divided into $2\text{ }\mu\text{m}$ segments. After [60].	57
Figure 34.	(b) Diffusion lengths are averaged over $2\text{ }\mu\text{m}$ sections of the line scan. The diffusion lengths vary between $4.6\text{ }\mu\text{m}$ and $11.2\text{ }\mu\text{m}$, with a mean of $7.1\text{ }\mu\text{m}$ and standard deviation of $2.0\text{ }\mu\text{m}$. After [60].	58

Figure 35.	Variations observed in diffusion length in TlBr and GaAs using spatially resolved transport imaging.....	59
Figure 36.	Impurity levels in Ge. The ionization energies are labeled in meV. Levels above the gap center (E_i) are donors, unless denoted as an acceptor (A). Levels below the gap center are acceptors, unless denoted as a donor (D). After [47].....	61
Figure 37.	TlBr crystals doped with either Se or Pb. Approximate locations of slices are shown in red. (a) For the Se doped TlBr crystal, slice C3 is shown, although slice C1 was used in this study. (b) For the Pb doped TlBr crystal, slice C1 was used.	62
Figure 38.	GDMS results for (a) Se doped TlBr and (b) Pb doped TlBr crystal.	62
Figure 39.	CL spectra at 295 K and 5 K for (a) Se doped TlBr and (b) Pb doped TlBr. A Gaussian fit to peak D is shown as a dashed line.....	63
Figure 40.	CL spectra at 5 K for (a) Se doped TlBr and (b) Pb doped TlBr.	64
Figure 41.	(a) PICTS spectrum and (b) Arrhenius plot. After [61].....	65
Figure 42.	Energy diagram showing mid-gap defect states related to Pb and Se dopants in TlBr. Diagram not to scale. After [61].....	67
Figure 43.	Intensity distributions for three random locations at 295 K and 5 K for (a) Se doped TlBr and (b) Pb doped TlBr.	67
Figure 44.	Intensity distributions for three random locations at 5 K for Se doped TlBr and Pb doped TlBr.....	68
Figure 45.	Least squares fitting to the data at 5 K for (a) Se doped TlBr and (b) Pb doped TlBr.	69
Figure 46.	Spatial variation in the diffusion lengths along 16 μm sections of the Se and Pb doped TlBr, averaged over 2 μm sections of the line scan images, at 5 K.....	70
Figure 47.	CL spectra at 295 K and 5 K for (a) CZT(ST1) and (b) CZT(372).	73
Figure 48.	CL spectra at 5 K for (a) CZT(ST1) and (b) CZT(372).	73
Figure 49.	CL mapping at 5 K for (a) CZT(ST1) and (b) CZT(372).	74
Figure 50.	Transport imaging at two locations, L1 and L2, for samples (a) CZT(ST1) and (b) CZT(372). Locations L1 and L2 represent widely separated locations on the crystals, up to 0.5 mm or more. L1 x492 and L1 x391, for example, represent sub-locations that may only be separated by 150 μm or less. The inset shows an overlay of the two line scan images at sub-locations L1 x250 and L1 x624.	75
Figure 51.	Comparison of intensity distribution at two different locations at 295 K for CZT(ST1) and CZT(372).	76
Figure 52.	Comparison of intensity distribution at 5 K for CZT(ST1) and CZT(372).	77
Figure 53.	Mathematical fits for diffusion length at 5 K for CZT(ST1) L1 x733 for data from (a) 2–12 μm and (b) 4–12 μm	80
Figure 54.	Normalized mean intensity distributions for CZT(372) for temperatures between 5 K and 60 K.....	80
Figure 55.	Temperature dependence of (a) diffusion length and (b) $\mu\tau$ product for CZT(372).	81

Figure 56.	Proposed explanation for non-uniform charge trapping due to Te inclusions. After [26].	82
Figure 57.	(a) Luminescence from CZT(ST1) from SEM operated in picture excitation mode. (b) Luminescence intensity from same region of CZT(ST1) crystal.	83
Figure 58.	(a) Optical image from SEM picture excitation mode, showing location of line scan in red. (b) Optical image from SEM line excitation mode. The data are extracted over the majority of the line scan (B-B') and over just the Te inclusion (A-A'). (c) Luminescence intensity distributions over the two regions.	84
Figure 59.	Schematic for investigating region of increased electron trapping associated with Te inclusions.	85
Figure 60.	Effects of photon recycling in a semiconductor.	88
Figure 61.	CL spectra at 5 K for CZT(372) and filter transmission spectra for (a) Short pass filters and (b) Long pass filters.	89
Figure 62.	Intensity distributions from transport imaging of CZT(372) at 5 K for unfiltered, short-pass filtered, and long-pass filtered conditions. The same data are shown with the y-axis plotted in (a) Intensity, as measured by counts recorded on the CCD array camera, and (b) Normalized scale, with each distribution normalized to its own maximum.	90
Figure 63.	CL spectra at 5 K for TlBr(Se) and filter transmission spectra for (a) Short pass filters and (b) Long pass filters	91
Figure 64.	Intensity distributions from transport imaging of TlBr(Se) at 5 K for unfiltered, short-pass filtered, and long-pass filtered conditions.	92
Figure 65.	Monte Carlo simulations for 20 keV electrons in TlBr showing (a) Electron trajectories, (b) Electron depth distribution, (c) Integrated energy density distribution in XZ plane, and (d) Integrated energy density distribution in XY plane.	94
Figure 66.	Monte Carlo simulations for 20 keV electrons in TlBr showing (a) Oblique and (b) Side views of the integrated energy density.	95
Figure 67.	Gaussian and Lorentzian fits to integrated energy distribution from Monte Carlo simulations with 20 keV electrons in TlBr.	96
Figure 68.	(a) Intensity distributions for n-type GaAs with beam energies from 5–30 kV, and (b) Gaussian and Lorentzian fits to the 20 keV intensity distribution. After [81].	97

LIST OF TABLES

Table 1.	Properties of TlBr.	28
Table 2.	GDMS dopant concentration, diffusion length, and $\mu\tau$ product at 5 K.	52
Table 3.	Diffusion length and $\mu\tau$ product at different locations on different slices of doped TlBr crystals at 5 K.	55
Table 4.	Activation energies, cross section, and trap type for identified deep levels. After [61]	65
Table 5.	Comparison of CL and PICTS data. After [61]	66
Table 6.	Diffusion length and $\mu\tau$ product at random locations on doped TlBr crystals at 5 K.	69
Table 7.	Properties of CZT. After [21]	71
Table 8.	Ambipolar diffusion length and $\mu\tau$ product for CZT(ST1) and CZT(372) at 295 K and 5 K.	78

THIS PAGE INTENTIONALLY LEFT BLANK

LIST OF ACRONYMS AND ABBREVIATIONS

CL	Cathodoluminescence
CCD	Charge Coupled Device
CCE	Charge Collection Efficiency
CdTe	Cadmium Telluride
CZT	Cadmium Zinc Telluride
EHP	Electron-Hole Pair
EDX	Energy Dispersive X-ray Spectroscopy
EAG	Evans Analytical Group
FWHM	Full Width at Half Maximum
GAO	Government Accounting Office
GDMS	Glow Discharge Mass Spectrometry
HPGe	High Purity Germanium
IAEA	International Atomic Energy Agency
IND	Improvised Nuclear Device
OM	Optical Microscope
PICTS	Photo-Induced Conductivity Transient Spectroscopy
PL	Photoluminescence
RDD	Radiological Dispersal Device
SEM	Scanning Electron Microscope
TlBr	Thallium Bromide

THIS PAGE INTENTIONALLY LEFT BLANK

ACKNOWLEDGMENTS

This work was supported by the DNDO Academic Research Initiative Grant NSF/ARI 083007.

I would like to thank my advisor, Dr. Nancy Haegel, for her professionalism, expertise, wisdom, and guidance throughout this experience. Dr. Haegel is an extraordinary professor and mentor, and I am blessed for the opportunity to learn from her.

Major Kevin Blaine, Professor Clyde Scandrett, and Professor Christopher Frenzen have been instrumental in the mathematical modeling used in this dissertation. I am thankful to work with such skilled mathematicians.

Our colleagues at the University of California, Berkeley, have made significant contributions to this work. I appreciate the opportunity to work with Holland Smith, Professor Eugene Haller, and Professor Daryl Chrzan.

I would like to thank Radiation Monitoring Devices, Inc. (RMD) for providing the TlBr samples and Redlen Technologies for providing the CZT samples.

My father has always loved exploration and engineering. He is the inspiration for this work.

I am forever grateful to my wife, Katrina, and our children for their love, patience, and encouragement during these graduate school years. Without their commitment and perseverance, I would not have been able to obtain this goal. Thank you.

I am thankful for the blessing from my Lord and Savior Jesus Christ to be able to study at the Naval Postgraduate School and pursue this goal of earning a doctorate degree.

THIS PAGE INTENTIONALLY LEFT BLANK

I. INTRODUCTION

A. NUCLEAR SECURITY THREATS

The United States faces significant threats in the area of nuclear security. The threats come from both state and non-state actors, each of whom may employ different methods of attack and delivery systems resulting in differing levels of consequences.

Potential state sources of nuclear weapons or fissile material include Iran, Russia, North Korea, and Pakistan [1]. Iran is currently a nation of key concern. A November 2011 report by the International Atomic Energy Agency (IAEA) found “credible” evidence that “Iran has carried out activities relevant to the development of a nuclear device” [2]. Iran, however, has continued to defy UN Security Council Resolution 1969 ordering it to suspend uranium enrichment operations [3], [4]. Terrorist groups have also actively sought nuclear weapons and fissile material for use against the United States. In 1994, for example, al Qaeda failed in an attempt to purchase uranium, but a 2004 report by the National Commission on Terrorist Attacks on the United States asserts “al Qaeda continues to pursue its strategic objective of obtaining a nuclear weapon . . . [and] remains interested in using a radiological dispersal device” [5].

Nuclear terrorism by a rogue state or group could take several forms. A group could employ a nuclear weapon or threaten its use in order to gain leverage. It may create an improvised nuclear device (IND) from illegally-obtained nuclear materials. It might release a radiological dispersal device (RDD) from radioisotopes designed for medical, research, or commercial use. Additionally, a terrorist cell could target installations that use radioactive materials, such as nuclear power plants [6].

Depending on the type of nuclear attack, the outcome could be catastrophic. One threat, with low probability but high consequence, is the detonation of a nuclear weapon in a major U.S. city. A ten-kiloton weapon detonated at Grand Central Station in Manhattan, New York, could potentially result in 500,000 instant fatalities, with hundreds of thousands of additional injuries and economic loss of over \$1 trillion [1].

In order to launch an attack against the United States using a nuclear weapon, IND, or RDD, a terrorist group may need to smuggle the weapon into the U.S., or smuggle in the weapon components and then assemble it in the U.S. The weapon or its components could be hidden in a vehicle, train, or ship, concealed in personal luggage at an airport, or even walked across an area of unprotected border [7], [8].

B. DETECTION CHALLENGES

There are many complex and intertwined challenges to detecting illicit fissile or radioactive materials to protect against the nuclear threat. A few of these challenges are considered here.

The vast borders of the United States and the sheer volume of cargo entering the U.S. each year confound radiation detection. In 2004, Admiral James Loy, former Deputy Secretary of the Department of Homeland Security, summarized the formidable scope of the problem facing the United States [9]:

We must secure nearly 7,500 miles of land border with Canada and Mexico, across which more than 500 million people, 130 million motor vehicles, and 2.5 million rail cars pass every year. We also patrol almost 95,000 miles of shoreline and navigable waters, and 361 ports that see 8,000 foreign flag vessels, 9 million containers of cargo, and nearly 200 million cruise and ferry passengers every year. We have some 422 primary airports and another 124 commercial service airports that see 30,000 flights and 1.8 million passengers every day. There are approximately 110,000 miles of highway and 220,000 miles of rail track that cut across our nation, and 590,000 bridges dotting America's biggest cities and small towns.

As of 2002, U.S. Customs was only physically inspecting 2% of the cargo entering the United States each year [10]. Due to increased awareness of the nuclear threat, by 2006 approximately 80% of the incoming cargo at port facilities was screened [11].

Detection and identification of radioactive materials depend on many factors, including the material quantity and decay scheme, the detection method (passive detection or active interrogation), the time allowed for detection, the distance between the source and the detector, the presence of shielding, and the knowledge of the operator. In passive detection, the detector simply detects radiation emitted from a source. In active

interrogation, however, a neutron or photon source bombards the source material, and the detector detects the secondary radiation that the source emits as a result of the bombardment [12]. Highly enriched uranium (HEU) is one of the materials of greatest concern. Unfortunately, it is also one of the most difficult to detect by passive means. Its low level of radioactivity and the nature of its radiation make it relatively easy to shield and therefore avoid detection [8]; depending on the purity of the HEU and the presence of shielding, hours of monitoring may be required to detect the HEU. In contrast, there are many legitimate sources of radiation that are easily detectable through passive means, including radiopharmaceuticals and many commercial goods such as ceramic tiles, fertilizers, and kitty litter. These legitimate sources can trigger radiation monitors, causing false alarms and costly delays [10], [13], [14].

In screening for radiation, the U.S. must balance two competing requirements – high sensitivity and high throughput. High sensitivity is required to distinguish between illicit radioactive materials such as HEU and legitimate sources such as radiopharmaceuticals. High throughput is required so as not to impede the flow of commerce [13]. The Government Accounting Office (GAO) has documented cases where officials at U.S. ports of entry have sacrificed sensitivity for throughput. In one instance, the sensitivity of portal monitors was reduced in order to limit the frequency of nuisance alarms from naturally occurring radioactive materials. In another case, officials allowed trucks to pass through portal monitors at speeds greater than optimal for the detection of nuclear material [8], [13]. These cases highlight the magnitude of the detection problem. By 2006, the U.S. had screened 80 million cargo containers with radiation portal monitors, which triggered 318,000 false alarms. Most of the false alarms came from naturally occurring radioactive materials, and none of the alarms were attributed to illicit radioactive materials. Advanced detectors are therefore required that will allow for more accurate detection of illicit radioactive materials with fewer false alarms [15].

Current detection technology fails to meet the new demands of homeland defense. National security applications require ruggedized instruments that can rapidly measure the energy and identify the type of incident radiation from gamma and neutron sources.

For most applications, detection of gamma rays with energies between 10 keV and 10 MeV is needed. In the lab and some limited field applications, cryogenically cooled high purity germanium (HPGe) semiconductor detectors can identify the isotopic signature of gamma rays with the required sensitivity and spectral resolution. The cooling requirement, however, excludes the use of HPGe for many national security needs. Instead, many hand-held radionuclide identification devices use inorganic scintillators such as thallium-doped sodium iodide and many radiation portal monitors used at borders to scan vehicles use scintillating plastics such as polyvinyl toluene. These HPGe substitutes have poor energy resolution, as shown in Figure 1, which makes identification of detected radionuclides difficult. Neutron detection for neutrons arising from fissile material is also required. Currently, however, there is no commercially available portable instrument for rapidly identifying neutron spectra. Advanced radiation detector materials are therefore needed to meet the needs of national security [9], [16].

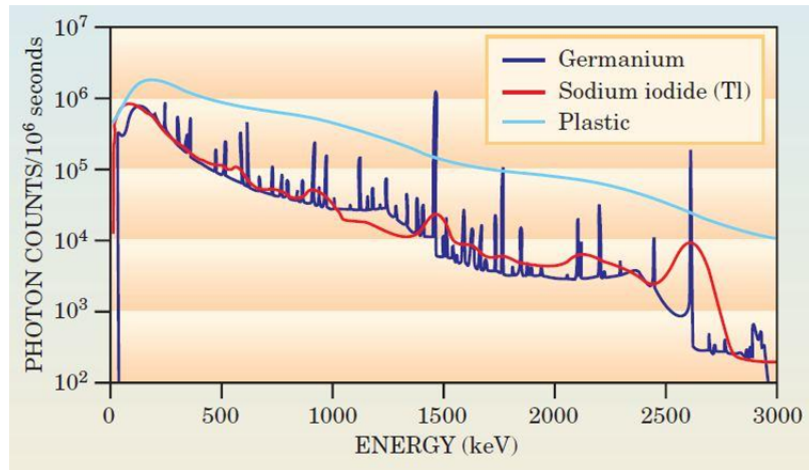


Figure 1. Comparison of energy resolution for natural background using high purity germanium, thallium-doped sodium iodide, and plastic scintillators. After [13].

C. MATERIALS PROBLEM

Two primary classes of solid-state radiation detection materials are scintillators and semiconductors. With both inorganic scintillators and semiconductors, incident radiation produces electron-hole pairs (EHPs) in the materials. For scintillation detectors,

these EHPs are further converted to optical photons. These photons traverse the material to the electrodes, where they are collected and converted to an electrical signal. For semiconductors, the EHPs themselves are the final carriers of information; under the application of a strong electric field, these free carriers move to the electrodes, where they produce a current pulse that is proportional to the number of charge carriers collected. In general, semiconductor detectors have better resolution than scintillation detectors. This is due in part to the direct conversion of EHPs to electrical signal in semiconductors, without the intermediary step of converting EHPs to photons as required in scintillation detectors [16].

Decades of research and development are required to grow crystals with suitable properties for use as semiconductor radiation detectors. Researchers have investigated materials that can deliver the same energy resolution as Ge while operating at room temperature as far back as the introduction of lithium-drifted Ge detectors in the 1960s [17]. Typically, however, new semiconductor materials have only been discovered at a rate of approximately once per decade [16]. This pace is inadequate for the needs of national security.

One of the challenges in characterizing and developing new radiation detection materials is that key indicators of detector performance, such as charge carrier lifetime, are not intrinsic properties of the material. Instead, carrier lifetime depends on the nature of both the impurities and native defects in the material, which in turn depends on the crystal growth process. First principles theories therefore cannot be used to reliably predict suitable detector material candidates. Instead, each candidate material must undergo a painstaking experimental process to develop a viable crystal growth method, improve the material properties to allow measurement and characterization, and refine the material properties to ensure high performance detector operation [17].

In the past, the pace and effectiveness of discovery of new candidate materials for radiation detection have been limited by a tendency to validate material performance only through fabrication and testing of actual radiation detectors [16]. New methods are therefore necessary that can probe the material properties of interest without requiring the cost and time burden of full device fabrication.

D. RESEARCH METHOD AND GOALS

To accelerate the development of existing materials and the discovery of new materials for gamma ray detectors, there are several critical research needs. Two of these needs are improved characterization of detector material properties and improved models of radiation-detection physics in detector materials [16]. This research aims to contribute to both.

The critical national security need for gamma ray detection is the ability to identify individual radionuclides. Each radionuclide emits a unique distribution of gamma radiation energies. To identify a radionuclide, high resolution energy spectroscopy is therefore essential [16]. For high energy resolution, a semiconductor detector needs uniform charge transport. A key measure of charge transport is the mobility-lifetime ($\mu\tau$) product, which is discussed in greater detail in Chapter II. A uniform $\mu\tau$ product across a detector results in high energy resolution, whereas variations in the $\mu\tau$ product degrade energy resolution [18].

This research focuses on quantifying variations in the $\mu\tau$ product in bulk semiconductors through materials characterization and modeling. A micro-characterization technique called transport imaging is being developed at the Naval Postgraduate School. Transport imaging is a contact-free all-optical technique that allows one to determine the $\mu\tau$ product of a sample, without the need for contact fabrication or device processing.

The broad objective of this research is to use a 2D carrier diffusion model in TlBr and CZT to demonstrate the application of transport imaging as a micro-analysis tool for characterizing the charge transport properties in bulk semiconductors for nuclear radiation detection. The specific goals of this research are to:

- Advance the development of a rapid assessment micro-characterization technique to determine the magnitude and spatial variation in the $\mu\tau$ product at 2 μm resolution.
- Investigate the dependence of the $\mu\tau$ product on temperature and doping in TlBr and CZT.

- Contribute to the development of a defect level map of Se and Pb in TlBr.
- Investigate the impact of Te inclusions on charge transport in CZT.
- Investigate the effects of photon recycling on diffusion length in TlBr and CZT.

E. PUBLICATIONS AND PRESENTATIONS

As a result of this research, the author wrote, contributed to, or presented the following:

D. J. Phillips, K. E. Blaine, L. J. Cirignano, G. Ciampi, and N. M. Haegel, "Cathodoluminescence and spatial variation in mobility-lifetime ($\mu\tau$) product in bulk doped thallium bromide," *IEEE Trans. Nucl. Sci.*, submitted.

H. M. Smith, D. J. Phillips, I. D. Sharp, J. W. Beeman, D. C. Chrzan, N. M. Haegel, E. E. Haller, G. Ciampi, H. Kim, and K. S. Shah, "Electronic effects of Se and Pb dopants in TlBr," *Appl. Phys. Lett.*, vol. 100, no. 20, pp. 202102-1 – 202102-4, 2012.

K. E. Blaine, D. J. Phillips, C. L. Frenzen, C. Scandrett, and N. M. Haegel, "Three-dimensional transport imaging for the spatially resolved determination of carrier diffusion length in bulk materials," *Rev. Sci. Instrum.*, vol. 83, pp. 043702-1 – 043702-7, 2012.

D. J. Phillips, N. M. Haegel, K. E. Blaine, H. Kim, G. Ciampi, L. Cirignano, "Spatial variation in mobility-lifetime product in bulk TlBr and CZT," Presented at *APS March Meeting*, Boston, MA, 1 March 2012.

THIS PAGE INTENTIONALLY LEFT BLANK

II. RADIATION SPECTROSCOPY AND THE $\mu\tau$ PRODUCT

A. GAMMA-RAY RADIATION SPECTROSCOPY

When a gamma-ray enters a semiconductor radiation detector, an “energy cascade” is initiated, converting a single quantum of radiation through a series of interactions with electrons and atomic nuclei to a distribution of electrons and holes that produce a current signal in an instrument readout system. The cascade begins when an absorbed gamma-ray creates primary electrons, predominantly through photoelectric, Compton, and pair production interactions. These primary electrons then undergo a series of quantum energy transfer processes, producing electrons, photons, plasmons, and phonons [16]. The cascade ultimately results in thermalized EHPs with energies on the order of 1 eV, phonons, and atoms displaced by elastic energy transfers. Under the application of a strong electric field, these thermalized EHPs are swept out of the detector medium and recorded as a current pulse. The current pulse is proportional to the number of charge carriers collected, and therefore the energy of the initial radiation [16]. This process is the basis for gamma-ray spectroscopy.

If the charge collection process is incomplete due to limited carrier transport and/or carrier trapping, a lower current pulse will be recorded, resulting in an inaccurate evaluation of the energy of the initial radiation. This translates into a broadening of the peak in the energy spectrum and lower detector resolution [19].

B. MOBILITY-LIFETIME PRODUCT

The $\mu\tau$ product is a key measure of charge transport in a semiconductor. It is comprised of two components—the drift mobility, μ_d , (commonly referred to as simply the mobility, μ), and the recombination lifetime, τ , (commonly referred to as simply the lifetime, τ). The mobility determines the drift velocity, v_d , which is the speed at which charges move through a material under the application of an electric field, E , through the relationship

$$v_d = \mu E \quad (1)$$

The lifetime is the average time that carriers exist before recombining, becoming trapped, or scattering. Together, the $\mu\tau$ product determines the drift length, λ , and diffusion length, L , for free carriers in a semiconductor. The drift length is a measure of the average distance that free carriers move through a material due to an applied electric field before recombining. The drift length is given by

$$\lambda = \mu\tau E \quad (2)$$

The diffusion length is a measure of the average distance that charges move through a material due to diffusion before recombining. The diffusion length is given by

$$L = \sqrt{\frac{k_B T}{e} \mu\tau} \quad (3)$$

where k_B is the Boltzmann constant, T is the temperature in K, and e is the fundamental unit of charge.

C. DETECTOR RESOLUTION AND CHARGE COLLECTION

The resolution of a gamma-ray detector is commonly defined as the energy peak full-width at half maximum (FWHM, or ΔE) divided by the centroid of the energy peak E_0 , given by

$$R = \frac{FWHM}{E_0} = \frac{\Delta E}{E_0}. \quad (4)$$

By convention, resolution is quoted as a percent [20]. An idealized detector response and FWHM is shown graphically in Figure 2.

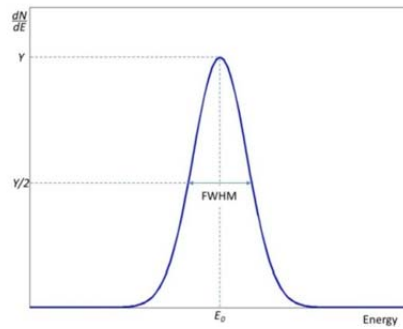


Figure 2. Simulated gamma-ray peak with FWHM and centroid energy E_0 . After [20].

The resolution of a detector depends on the FWHM, and the FWHM depends primarily on three factors—carrier statistics, electronic noise, and charge carrier collection. Each factor contributes to peak broadening in the energy spectrum. The FWHM is given by

$$\Delta E = \sqrt{(\Delta E_F)^2 + (\Delta E_E)^2 + (\Delta E_C)^2} . \quad (5)$$

The first term, ΔE_F , represents Fano noise and accounts for the inherent statistical fluctuations in the number of charge carriers created. The second term, ΔE_E , represents electronic noise and is dominated by leakage or dark current. The final term, ΔE_C , arises from incomplete charge collection [20].

Figure 3 shows the relative contribution to peak broadening from each term for an HPGe detector with a volume of 86 cm³. The greatest contribution comes from incomplete charge collection [20]. Variations in the $\mu\tau$ product within the detector affect this term.

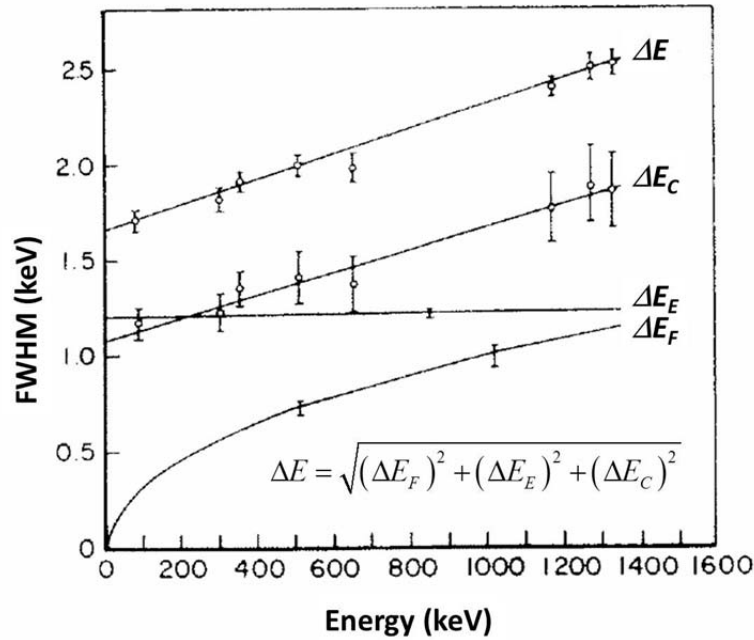


Figure 3. Contribution to FWHM due to Fano noise (ΔE_F), electronic noise (ΔE_E), and charge collection (ΔE_C). After [20].

The influence of variations in the $\mu\tau$ product on detector resolution can be seen indirectly by considering the charge collection efficiency (CCE). The CCE is a ratio of the initial amount of charge Q_0 created by EHPs due to the absorption of a gamma-ray to the total charge induced Q on the electrodes of the detector, or

$$CCE = \frac{Q}{Q_0}. \quad (6)$$

Ideally, a detector would have a CCE of unity, meaning all created charge is collected. In real semiconductors, however, carrier diffusion and carrier trapping result in the loss of carriers and reduced charge at the electrodes [21]. Statistical models and curve-fitting methods have been extensively developed to determine the CCE [22], [23].

One common curve-fitting technique for determining the actual CCE is using the Hecht method. A radiation source such as a laser or an alpha emitter is used to generate charge near the detector cathode or anode. The induced charge signal is then measured as a function of the bias voltage across the detector [24]. The $\mu\tau$ product is obtained by curve fitting to the Hecht equation, given by

$$CCE = \frac{\lambda_e}{L} \left\{ 1 - \exp \left[- \left(\frac{L - x_0}{\lambda_e} \right) \right] \right\} + \frac{\lambda_h}{L} \left\{ 1 - \exp \left(- \frac{x_0}{\lambda_h} \right) \right\} \quad (7)$$

where L is the detector thickness, x_0 is the distance from the cathode to the point of charge creation, and λ_e and λ_h are the drift length of electrons and holes, respectively. The drift lengths are

$$\lambda_e = (\mu\tau)_e E \quad (8)$$

$$\lambda_h = (\mu\tau)_h E \quad (9)$$

where $(\mu\tau)_e$ and $(\mu\tau)_h$ are the $\mu\tau$ products of electrons and holes, respectively. Small ratios of λ/L for either electrons or holes reduce the CCE, resulting in peak broadening in the energy spectrum [21]. Spatial variations in the $\mu\tau$ products also cause variations in these ratios, also contributing to peak broadening.

The influence of variations in the $\mu\tau$ product on detector resolution can be seen directly in certain cases. One case is considered here. Typically, the contribution of charge collection to peak broadening has been determined by the semi-empirical formula

$$\Delta E = \sqrt{(\Delta E_F)^2 + (\Delta E_E)^2 + (2.355)^2 a_1 E^{a_2}} \quad (10)$$

where a_1 and a_2 are semi-empirical constants determined by best-fitting [21]. Kozoresov (2005), however, has shown that for pixelated detectors,

$$\Delta E = \sqrt{(\Delta E_F)^2 + (\Delta E_E)^2 + (2.355)^2 G(E) E^2} \quad (11)$$

where the trap factor $G(E)$ can be given in closed form as

$$G(E) = \left(\frac{L_0(E)}{\lambda_e} \right)^2 \quad (12)$$

where $L_0(E)$ is the photon absorption length [25]. Here, it is possible to see directly that variations in the $\mu\tau$ product would result in variations in the trap factor, which contributes to peak broadening.

D. MOBILITY-LIFETIME PRODUCT MEASUREMENT TECHNIQUES

Several techniques are available for measuring the material uniformity and variations in the $\mu\tau$ product of a semiconductor. These methods include alpha particle response characterization [26], high resolution mapping techniques using synchrotron X-rays, nuclear microprobes and ion microbeams, [27] – [29] and transport imaging [30]. Except for transport imaging, all of the mapping techniques require device processing and some form of the Hecht equation to extract the $\mu\tau$ product.

One limiting assumption of the Hecht relation is that charge trapping is uniform within the bulk of the material and detrapping is negligible [19], [31]. Real crystals, however, have inhomogeneities in charge trapping. Additionally, the $\mu\tau$ products obtained using the Hecht relationship are average values over the intercontact distance. Therefore, although a map of the $\mu\tau$ product is generated, the $\mu\tau$ products represent averages over a large distance, with distances ranging from millimeters to centimeters or more, depending on the type of detector. While this is relevant for detector performance,

it is limited in advancing the type of micro-scale characterization that will be required for more fundamental understanding of material properties and the actual role of various defects and dopants that limit performance.

Transport imaging is a unique imaging method based on the use of a scanning electron microscope (SEM) that allows measurements of the diffusion length and extraction of the $\mu\tau$ product in luminescent materials without the need for device processing, applied electric fields, or averaging over large intercontact distances. In transport imaging, the SEM generates free charge carriers in a semiconductor, and a charged coupled device (CCD) array camera records the motion of these charge carriers as they diffuse by imaging the distribution of their recombination luminescence. The technique has been applied previously to obtain $\mu\tau$ products in bulk GaAs, minority carrier lifetimes in heteroepitaxial GaInP, and minority-carrier diffusion lengths in ordered GaInP [32] – [35]. This work will advance the application of transport imaging as a micro-analysis tool for the characterization of bulk materials for nuclear radiation detectors.

III. TRANSPORT IMAGING

A. EXPERIMENTAL SETUP

Cathodoluminescence (CL) is the emission of light from a material under excitation by an electron beam. In order to apply transport imaging to materials, the samples must have a CL signature. For CL, samples are placed on the continuous-flow cold stage of a JEOL 840A scanning electron microscope (SEM) and may be cooled with liquid helium. Temperatures from 300 K to 5 K can be obtained. The electron beam is incident normal to the sample. In this work, the SEM beam excitation energies varied between 10.0 keV and 20.0 keV, the probe currents ranged from 3×10^{-10} A to 6×10^{-10} A, and the magnifications ranged from 1000 \times to 2000 \times . An Oxford CL system with a 0.25 m path length monochromator was used to perform spectroscopy. The detector is a thermoelectrically cooled photomultiplier with response from 300–900 nm. Spectroscopy can be performed for emission obtained with the SEM operating in either spot or picture (area) mode. It is also possible to acquire CL area maps in either panchromatic or monochromatic mode. The SEM and CL system are shown in Figure 4.

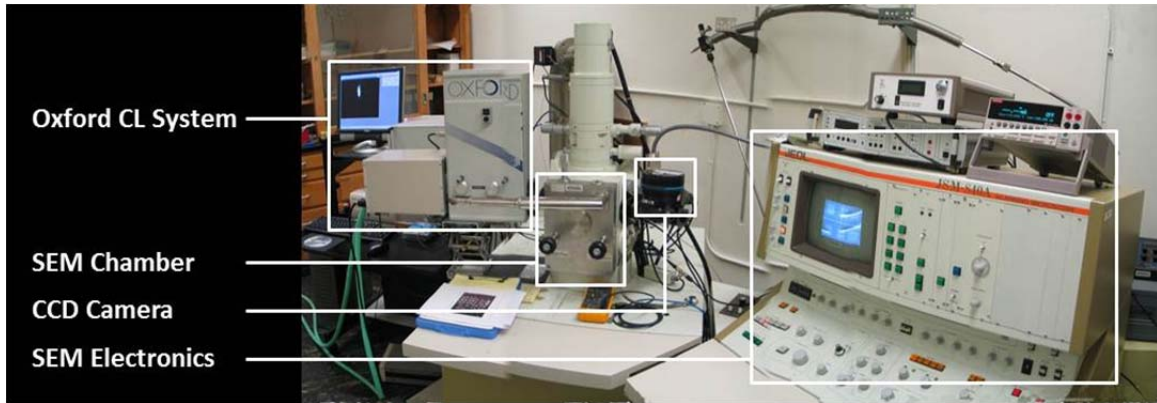


Figure 4. Experimental set up for CL and transport imaging using the electron beam from the SEM and an external CCD array camera.

For transport imaging, an optical microscope is inserted into the vacuum chamber of the SEM using a retractable arm. A small hole, or objective pipe, in the microscope

allows passage of the electron beam. A 45 degree mirrored surface collects the luminescence and directs it through a light guide to a 1284 pixel \times 1472 pixel thermoelectrically-cooled Si CCD array camera external to the SEM chamber. The pixel size on the CCD camera is $6.8\text{ }\mu\text{m} \times 6.8\text{ }\mu\text{m}$, and the magnification of the optical microscope is $\sim 20\times$, resulting in optical images with spatial resolution of $\sim 400\text{ nm/pixel}$. The setup for transport imaging is shown in Figures 4 and 5.

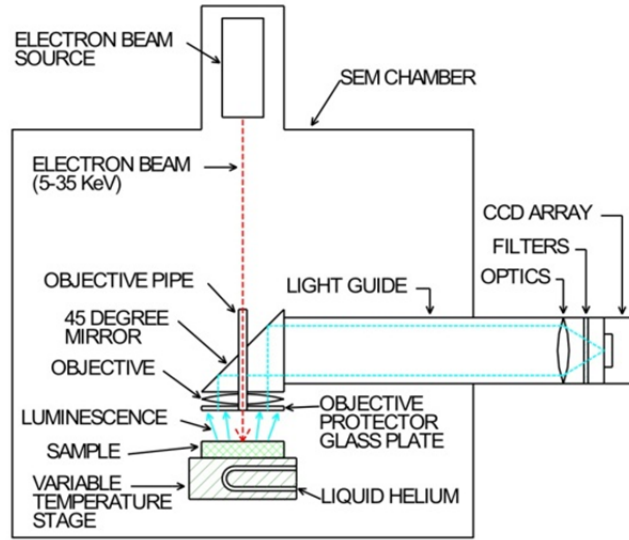


Figure 5. System schematic for transport imaging using the electron beam from the SEM and an external CCD array camera.

B. MATHEMATICAL MODEL OVERVIEW

In transport imaging, the electron beam of the SEM generates the EHP charge carriers in the semiconductor material. The charge carriers can diffuse through the material and recombine at different locations, emitting light. The CCD array camera records the location and intensity of the recombination luminescence. By fitting a model to the recorded intensity distribution, it is possible to extract the diffusion length and calculate the $\mu\tau$ product.

The model (1D, 2D, or 3D) employed in transport imaging to extract the diffusion length depends on the semiconductor material geometry (nanowire, thin film, or bulk sample) and the SEM excitation mode (spot or line mode). In the following section, we

review the models for the study of nanowires and thin films, and then describe the extension to bulk samples that is applied in this work. The semiconductor material geometries, SEM excitation modes, and models are summarized in Figure 6.

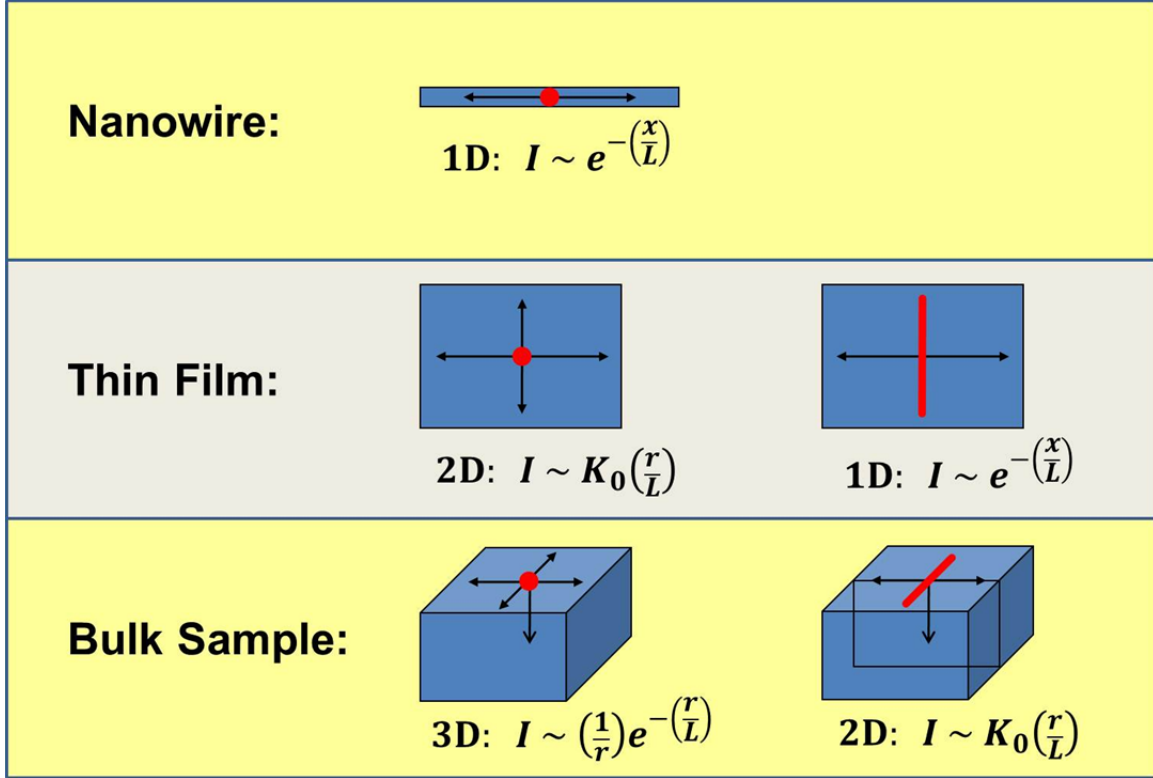


Figure 6. Summary of the semiconductor material geometries (nanowire, thin film, or bulk sample), SEM excitation modes (red dot \equiv spot mode, red line \equiv line mode), and models (1D, 2D, or 3D). Arrows indicate diffusion directions.

For nanowires, the SEM beam is operated in spot mode, and a 1D model is applied. The intensity of recorded light I is given by

$$I \sim e^{-\left(\frac{x}{L}\right)} \quad (13)$$

where x is the horizontal distance from the SEM beam. The 1D model for transport imaging has been applied previously to GaN nanowires using near field optical microscopy [36].

For thin films, the SEM beam may be operated in either spot mode or line mode, providing either a quasi point source or 1D line source for carrier excitation. For spot mode, a 2D diffusion model is applied, and the intensity of recorded light is given by

$$I \sim K_0\left(\frac{r}{L}\right) \quad (14)$$

where K_0 is a modified zeroth order Bessel function of the second kind, and r is the radial distance $\left(r = \sqrt{x^2 + y^2}\right)$ from the point source in the plane of the thin film to an arbitrary location (x,y) where recombination occurs and light is generated. The 2D model for transport imaging in thin films has been applied previously to the study of ordered GaInP for solar cell applications [35]. To take advantage of symmetry, the SEM may also be operated in line mode for thin films. This reduces a 2D problem to a 1D problem. For line excitation in thin films, a 1D model is applied, and the intensity of the recorded light is given by Equation (13). The 1D excitation model for transport imaging in thin films has been applied previously to the study of dislocation networks in heteroepitaxial GaInP [34], [35].

For bulk samples, the SEM beam may be operated in either spot mode or line mode. For spot mode excitation, a 3D diffusion model is applied, and the intensity of recorded light is given by

$$I \sim \left(\frac{1}{r}\right) e^{-\left(\frac{r}{L}\right)} \quad (15)$$

where r is the radial distance $\left(r = \sqrt{x^2 + y^2 + z^2}\right)$ from the point source on the surface to an arbitrary location (x,y,z) in the bulk sample where light is generated [37]. By again taking advantage of symmetry, the problem may be reduced from 3D to 2D by operating the SEM in line mode. For line mode excitation, a 2D diffusion model is applied, and the intensity of the recorded light is obtained by integration through the bulk (z -direction) in Equation (14), with the modification that $r = \sqrt{x^2 + y^2 + z^2}$. The 2D model for transport

imaging in bulk samples has been applied for the first time to GaAs by Blaine [32], [33]. For this present work in TlBr and CZT, the 2D model is also applied, as described in greater detail below.

C. BULK SAMPLE 2D MATHEMATICAL MODEL AND ASSUMPTIONS

1. Mathematical Model

A mathematical model has been developed by Blaine [32], [33] to extract the diffusion length L and the mobility-lifetime product $\mu\tau$ from the luminescence distribution using the 2D model for transport imaging in bulk material. The model is briefly described here.

In the 2D model for bulk samples, the SEM is used to generate a line of charge along the y -direction of the sample, as shown in Figure 7(a). The rate of charge generation per unit length is given the symbol g [charge/cm·s]. When electrons impact the bulk sample, they create a generation volume of EHP charge carriers [EHPs/cm³] below the surface of the sample, primarily through photoelectric, Compton, and pair production interactions. The centroid of the generation volume is modeled as a delta function at the position $x = 0$ and depth $z = z_0$ below the surface, as shown in Figure 7(b).

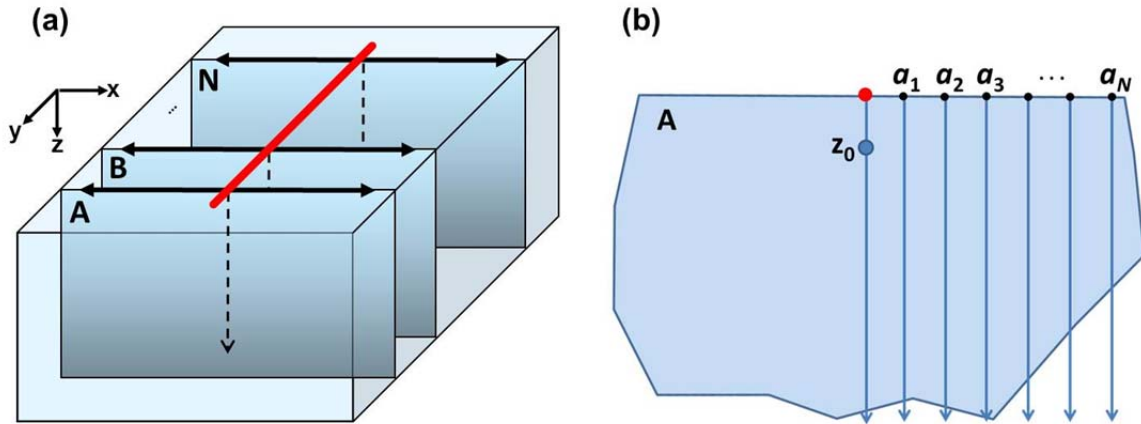


Figure 7. (a) The SEM generates a line of excess charge carriers across the bulk sample. The bulk sample is modeled as a series of semi-infinite planes, labeled A through N. (b) For each plane, the line source is modeled as a delta function at depth z_0 below the surface. The carrier concentration $u(x)$ is determined for each point on the x -axis of the plane, labeled $x = a_1 \dots a_N$.

The charge carriers created in the generation volume diffuse and recombine. The concentration of charge carriers at any location \vec{r} in the material is given by the symbol $u(\vec{r})$. In the 2D model, both the line source of excitation and the bulk sample are modeled as infinite in the y -direction. This is a valid assumption as long as the length of line source is much greater than the carrier diffusion length in the material. Under this condition, there is no change in the carrier concentration along the y -direction. As a result,

$$u(\vec{r}) = u(x, z). \quad (16)$$

With this simplification, the bulk sample can be treated as set of semi-infinite planes, labeled A through N in Figure 7(a), with diffusion in the x and z directions only. Analysis can therefore be restricted to a single plane. Analysis of the SEM line source on the bulk sample has therefore been reduced to analysis for a point source in a plane.

The diffusion of charge carriers is governed by the continuity equation. The time rate of change of the charge carrier concentration depends on the rate of charge carrier generation by the SEM beam, the rate of recombination, and carrier diffusion, given by

$$\frac{\partial}{\partial t} u(\vec{r}, t) = G - R + \frac{1}{e} (\nabla \cdot \vec{J}) \quad (17)$$

where $u(\vec{r}, t)$ is the charge carrier concentration at position \vec{r} and time t , G is the charge carrier concentration generation rate, R is the charge carrier concentration recombination rate, e is the fundamental unit of charge, and \vec{J} is the current density.

For transport imaging with the beam operating in line mode, the time required for the beam to raster back and forth is short compared to the selected exposure time, and the integrated dwell time for the beam at any point is very long compared to the carrier lifetime. This creates steady-state conditions for the charge carrier distribution. Under steady-state conditions,

$$\frac{\partial}{\partial t} u(\vec{r}, t) = 0. \quad (18)$$

The charge carrier generation rate is given by

$$G = g \cdot \delta(x) \delta(z - z_0). \quad (19)$$

The charge carrier recombination rate under steady-state conditions is

$$R = \frac{u(\vec{r})}{\tau} \quad (20)$$

where τ is the recombination lifetime. The current density in the absence of an electric field is

$$\vec{J} = eD\nabla u(\vec{r}) \quad (21)$$

where D is the ambipolar diffusion constant. The ambipolar diffusion constant is related to the relevant diffusion length through the relationship

$$L = \sqrt{D\tau} . \quad (22)$$

Combining Equations (16) through (22) results in

$$\nabla^2 u(x, z) - \frac{1}{L^2} u(x, z) + \frac{g}{D} \delta(x) \delta(z - z_0) = 0 . \quad (23)$$

Two boundary conditions are specified. The first boundary condition forces the excess carrier concentration to zero at large distances from the source. This condition is given by

$$u(x, z) \rightarrow 0 \text{ as } \sqrt{x^2 + z^2} \rightarrow \infty . \quad (24)$$

The second boundary condition introduces the surface recombination velocity S and specifies that the diffusion of charge carriers normal to the surface is proportional to the charge carrier concentration near the surface. This condition is given by

$$D \frac{\partial}{\partial z} u(x, z) = Su(x, z) \text{ at } z = 0 . \quad (25)$$

In order to fit the model to the luminescence data collected through transport imaging, it is necessary to solve Equation (23) for $u(x, z)$ subject to the boundary conditions given by Equations (24) and (25). After solving for $u(x, z)$, it is necessary to integrate $u(x, z)$ through the depth of the material, from $z = 0$ to infinity, since below band gap photons can escape from the bulk of the material. This results in a model solution for the excess carrier concentration $u(x)$ for each point on the x -axis of the plane, labeled $x = a_1 \dots a_N$ for plane A in Figure 7(b). The analytic model solution for the integrated excess carrier concentration, as derived by Blaine in [32], is

$$u(x) = A \left\{ \int_{\frac{x}{L}}^{\infty} K_1(t) \sqrt{t^2 - \left(\frac{x}{L}\right)^2} dt + \int_{z_0}^{\infty} K_0\left(\frac{\sqrt{t^2 + x^2}}{L}\right) \frac{e^{\left(\frac{S}{D}\right)(z_0 - t)} - 1}{L} dt \right\} \quad (26)$$

where K_0 is the zeroth-order modified Bessel function of the second kind, K_1 is the first order modified Bessel function of the second kind, and

$$A = \frac{gL}{\pi D}. \quad (27)$$

The model solution in Equation (26) is based on the assumption that the recorded luminescence intensity is proportional to the integrated carrier concentration $u(x)$. The model is fit to the normalized luminescence intensity data to obtain the diffusion length. The fitting is done using the Levenberg-Marquardt algorithm to minimize the square residual [32], [33].

The diffusion length is related to the $\mu\tau$ product by combining Equation (22) with the Einstein relationship, given by

$$D = \frac{k_B T}{e} \mu \quad (28)$$

where k_B is the Boltzmann constant and T is the temperature in K. Combining Equations (22) and (28) results in

$$L = \sqrt{\frac{k_B T}{e} \mu \tau}. \quad (29)$$

Equation (29) allows for the extraction of the $\mu\tau$ product from the diffusion length obtained from the fit of Equation (26).

2. Model Assumptions

Two key assumptions of the model are low injection conditions and constant lifetime. When excess EHPs are created in a semiconductor, the spontaneous radiative lifetime for band to band recombination is given by

$$\tau_R = \frac{n_e}{R} = \left[\frac{N_c N_v}{A k_B T (n_0 + p_0)} \right] \left[1 + \left(\frac{n_e}{n_0 + p_0} \right) \right]^{-1} \quad (30)$$

where n_e is the excess carrier concentration, R is the recombination rate, N_c is the density of states at the conduction band edge, N_v is the density of states at the valence band edge, A is the Einstein A coefficient, k_B is the Boltzmann constant, T is the temperature, n_0 is the equilibrium electron concentration, and p_0 is the equilibrium hole concentration. Under low injection conditions in n -type material, $n_e \ll n_0$, resulting in

$$\tau_R = \left(\frac{N_c N_v}{A k_B T} \right) \left(\frac{1}{n_0 + p_0} \right). \quad (31)$$

Typically, the coefficients of the carrier concentrations are combined into one coefficient, where

$$B = \frac{A k_B T}{N_c N_v}. \quad (32)$$

Combining Equations (31) and (32) yields

$$\tau_R = \frac{1}{B(n_0 + p_0)}. \quad (33)$$

For n -type doping, where $n_0 \gg p_0$ and $n_0 = N_D$, Equation (33) reduces to

$$\tau_R = \frac{1}{B N_D}. \quad (34)$$

Thus, the model for detecting, for example, the minority carrier (hole) diffusion length in n -type material, is based on a single constant lifetime under low-injection conditions [38].

D. TRANSPORT IMAGING EXAMPLE

This section presents a detailed example of the transport imaging technique. A sample of TlBr doped with copper, iron, and zinc is used for demonstration.

For transport imaging in a bulk sample, the SEM beam is operated in line mode to generate a line of charge carriers along the y -direction of the sample, as shown in the image of the recombination luminescence in Figure 8(a). To avoid edge effects, in this example a 10 μm segment is extracted from the center of the $\sim 60 \mu\text{m}$ line scan image; segments of other lengths may be chosen, with 40 μm segments most commonly selected.

Planar and oblique views of the recombination luminescence intensity distributions from the extracted 10 μm segment are shown in Figures 8(b) and 8(c). Note that since the resolution of the imaging system is 0.4 $\mu\text{m}/\text{pixel}$, the 10 μm segment is comprised of 25 individual pixels along the y -direction. This results in 25 separate intensity distributions in the 10 μm segment.

The diffusion length information is contained in the intensity distribution perpendicular to the line scan, along the x -axis. Each of the 25 distributions shown in Figure 8(c) or 8(d) is normalized, and then averaged to create Figure 8(d). Often, there is a small bump to the left of the peak due to a reflection in the optical system, although this bump is not visible in visible in Figure 8(d). Therefore, by convention, data from only one side of the peak ($x > 0$) in Figure 8(d) are used for least squares fitting to the model.

Figure 8(e) shows the normalized mean intensity distribution data and the best-fit line from the model given by Equation (26). For this example fit, data were taken beginning at $x = 4 \mu\text{m}$ to avoid effects of the generation volume. The model provides the diffusion length as one of the fitting parameters. This diffusion length is then used in Equation (29) to calculate the $\mu\tau$ product.

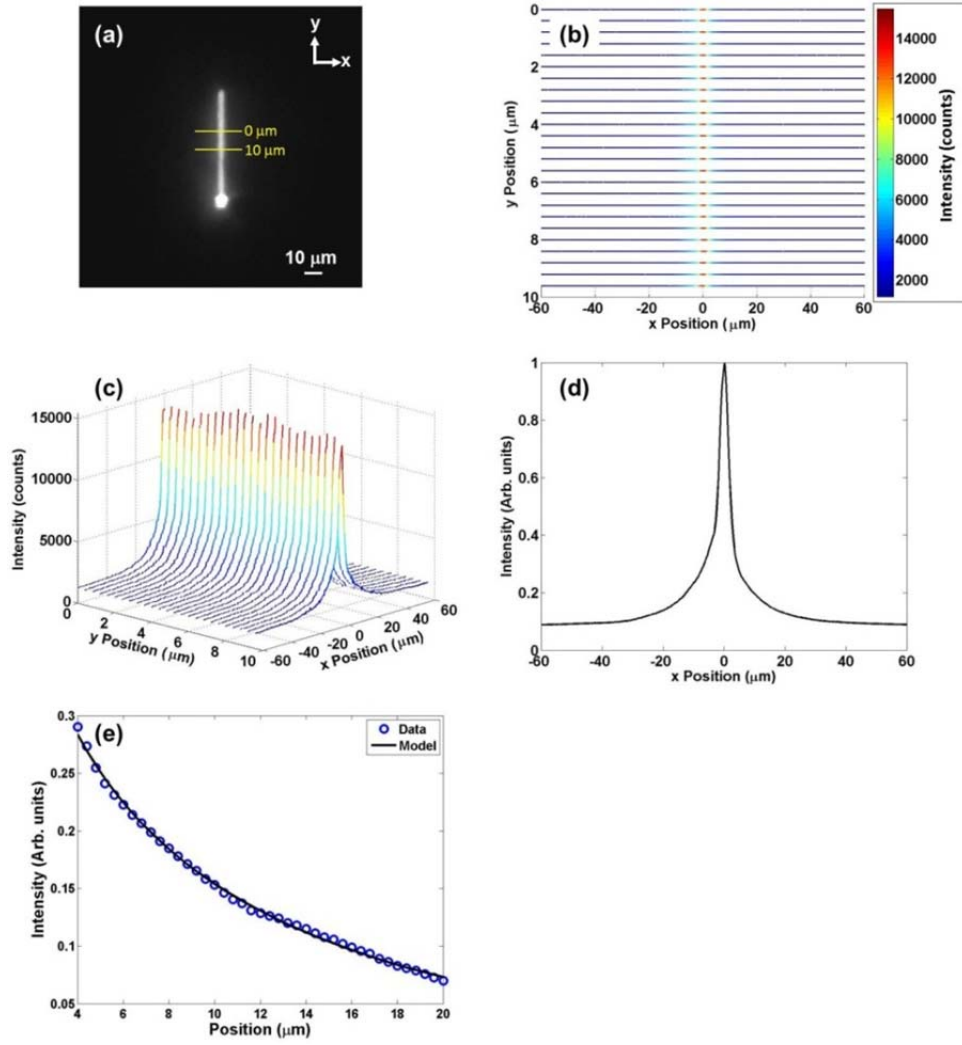


Figure 8. (a) SEM line scan luminescence image of TlBr crystal. (b) Planar and (c) Oblique views of a 10 μm segment (25 pixels) of the recombination luminescence intensity distribution. The diffusion length information is contained in the intensity distribution perpendicular to the line scan, along the x -axis. (d) Normalized mean recombination luminescence intensity distribution for the TlBr crystal. (e) Data from right side of distribution from Figure 4(d) and best-fit line from least squares fitting to the model.

THIS PAGE INTENTIONALLY LEFT BLANK

IV. INITIAL INVESTIGATION OF BULK THALLIUM BROMIDE

A. OVERVIEW OF THALLIUM BROMIDE

1. Properties of TlBr

TlBr is an attractive compound semiconductor alternative to HPGe for room temperature radiation detection and gamma spectroscopy [39]. Its high density (7.56 g/cm^3) and atomic number ($Z_{\text{Tl}} = 81$, $Z_{\text{Br}} = 35$) result in high photon attenuation and detection efficiency [16], [40]. The wide indirect bandgap (2.68 eV) and high room-temperature resistivity ($\sim 10^{10} \text{ } \Omega \text{ cm}$) of TlBr reduce leakage current and shot noise [41], [21]. TlBr has a simple cubic crystal structure and a low melting point (460 °C), which makes it easy to grow single crystals [42]. Advances in TlBr purification techniques and growth processes have led to steady improvements in the mobility-lifetime products of electrons and holes, $(\mu\tau)_e$ and $(\mu\tau)_h$, respectively. Values of $(\mu\tau)_e$ of $6.5 \times 10^{-3} \text{ cm}^2/\text{V}$ and $(\mu\tau)_h$ of $\sim 4 \times 10^{-4} \text{ cm}^2/\text{V}$ at 300 K have recently been reported that are comparable to those of cadmium telluride (CdTe) and Cadmium Zinc Telluride (CZT). With cooling to 18° C and depth correction techniques, energy resolutions of $< 1\%$ (FWHM) for the 662 keV peak of ^{137}Cs have been achieved for TlBr array detectors [40]. Table 1 summarizes select properties of TlBr.

Table 1. Properties of TlBr.

Property	Value	Reference
Atomic Number	$Z_{\text{Tl}}: 81, Z_{\text{Br}}: 35$	[43]
Density	7.56 g/cm^3	[43]
Bandgap	2.68 eV	[43]
Resistivity	$\sim 10^{10} \Omega\cdot\text{cm}$	[43]
Electron Mobility	$40 (\text{cm}^2/\text{V}\cdot\text{s})$	[44]
Hole Mobility	$12 (\text{cm}^2/\text{V}\cdot\text{s})$	[44]
Electron $\mu\tau$ Product	$6.5 \times 10^{-3} \text{ cm}^2/\text{V}$	[40]
Hole $\mu\tau$ Product	$\sim 4 \times 10^{-4} \text{ cm}^2/\text{V}$	[40]
Melting Point	$460 \text{ }^\circ\text{C}$	[21]
Crystal Structure	Cubic (CsCl)	[21]

Despite recent advances in crystal growth and purification, challenges remain before TlBr can be widely deployed as a room temperature nuclear radiation detector. It displays significant ionic conductivity under bias, which degrades detector performance over time. Additionally, the origin of its good transport properties ($\mu\tau$ product) and high resistivity are not well understood [45], [46].

Semiconductors such as TlBr with high resistivity ($> \sim 10^7 \Omega\cdot\text{cm}$) are classified as semi-insulating [47]. High resistivity is generally achieved through the intrinsic nature of the material, purification, or compensation doping. Most materials are far from intrinsic, and purification is required. Ge has been made semi-insulating through purification of electrically active dopants to the level of $\sim 10^{10} \text{ cm}^{-3}$ and by cooling. For most materials, however, such pure purification levels are not achievable, and compensation of existing impurities is necessary. Dopants may be introduced or defects may be controlled in order to create deep levels that compensate shallow donors or acceptors and “pin” the Fermi level near the center of the bandgap [48], [49]. Unfortunately, the same deep levels that ensure high resistivity are also often highly efficient recombination centers and carrier traps, which can reduce the $\mu\tau$ product of the material [44], [50].

In TlBr, the origin of the high resistivity is not well understood, and competing models have been proposed. Du (2010) has shown theoretically that low energy native

defects do not induce deep electron traps in TlBr, and that the dominant native defects in TlBr are Schottky defects (pairs of Tl and Br vacancies) which pin the Fermi level near the middle of the bandgap [45]. Elshazly (2010), however, argues that the pinning of the Fermi level in TlBr is due to the presence of deep level traps that compensate shallow level traps [44]. The contributions of ionic conductivity must also be fully investigated in order to understand and isolate the electronic contributions.

TlBr is also not a well-characterized semiconductor material, and much more work remains to be done to develop high volume, well-controlled growth and performance. Because transport imaging isolates only electronic transport, it can play a role in this work.

2. Transport Imaging in High Resistivity TlBr

As a semi-insulating material with the Fermi level pinned near the middle of the gap, the concentration of electrons and holes in TlBr is very low and approximately equal [32], [43]. The luminescence that we measure in transport imaging will therefore be due to recombination of the EHPs that we created with the SEM beam. In transport imaging, no electric field is applied to the sample. The EHPs therefore diffuse together as excitons. The diffusion of charge carriers is limited by the mobility of the slower carrier, which is the hole in TlBr. The diffusion length measured is therefore, to first order, an ambipolar diffusion length. The mathematical fit to the model subsequently generates an ambipolar $\mu\tau$ product.

B. CRYSTAL GROWTH

Analysis in TlBr began with sample 45-S10 from crystal ZR26-45YD. The detector-grade crystal was grown by Radiation Monitoring Devices, Inc. (RMD) for making planar and array detectors. For crystal growth, a synthesized 5N purity TlBr compound was purchased from a commercial vendor and used as the starting material. The crystal went through 100 passes of zone refining and purification before being grown by the travelling molten zone method. It was grown in an open boat under a HBr and Ar mix gas flow.

C. GLOW DISCHARGE MASS SPECTROMETRY

Glow discharge mass spectrometry (GDMS) was performed by Evans Analytical Group (EAG) to determine impurity concentrations. GDMS is an important characterization technique for TlBr because it can detect a wide range of impurities. The current state of TlBr is such that it can contain many different types of impurities in the concentration range of 10^{15} – 10^{19} cm⁻³. GDMS results for sample 45S-10 are shown in Figure 9. The impurities that remain in the crystal in the highest concentrations after zone refining and growth are aluminum (65 ppm wt, 1.1×10^{19} cm⁻³), silicon (2.3 ppm wt, 3.7×10^{17} cm⁻³), and barium (3.3 ppm wt, 1.1×10^{17} cm⁻³). These residual levels indicate that sample 45-S10 is unintentionally highly doped.

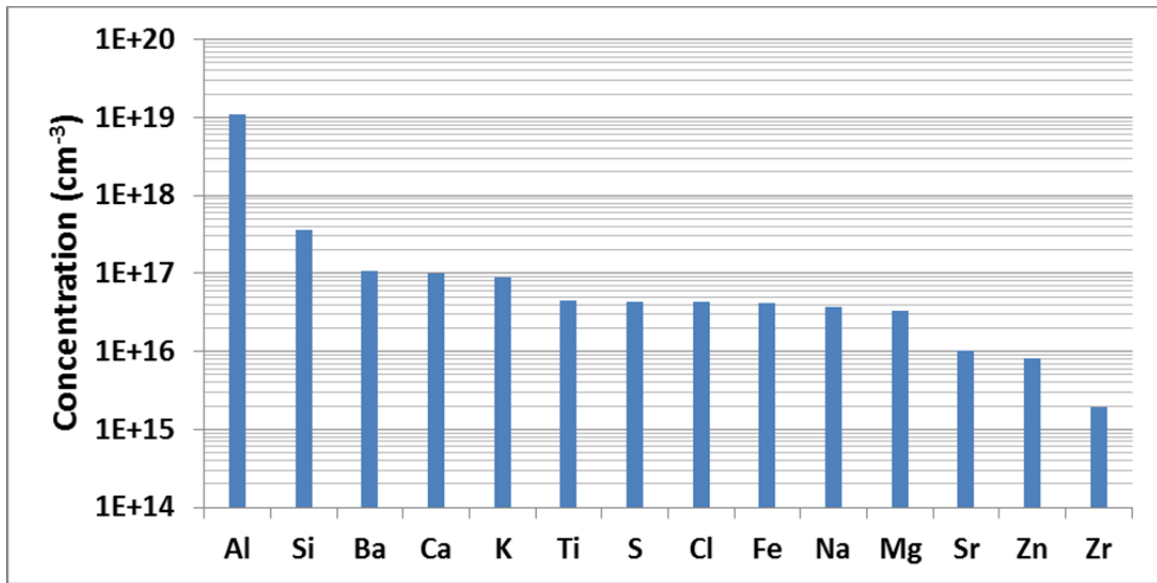


Figure 9. GDMS results for TlBr sample 45-S10.

D. CATHODOLUMINESCENCE

In order to perform transport imaging on a sample, the sample must have a CL signature. CL mapping and spectroscopy were performed on TlBr sample 45-S10 to determine if the samples would luminesce. Since TlBr is an indirect band gap material, it was not known if TlBr would emit sufficient luminescence. To our knowledge, only one previous report exists for CL in TlBr, and the spectra was obtained at 95 K and showed limited signal to noise ratio [51].

Room temperature panchromatic CL mapping was performed on sample 45-S10, as shown in Figure 10. The SEM operating parameters were 20.0 kV, 6×10^{-10} A, and 2000 \times magnification. Due to the depth of penetration of the SEM beam, effects of surface contamination are negligible. Intensity variations are observed on a scale of ~ 10 μm . It is this type of spatial variation that can be quantitatively studied with transport imaging.

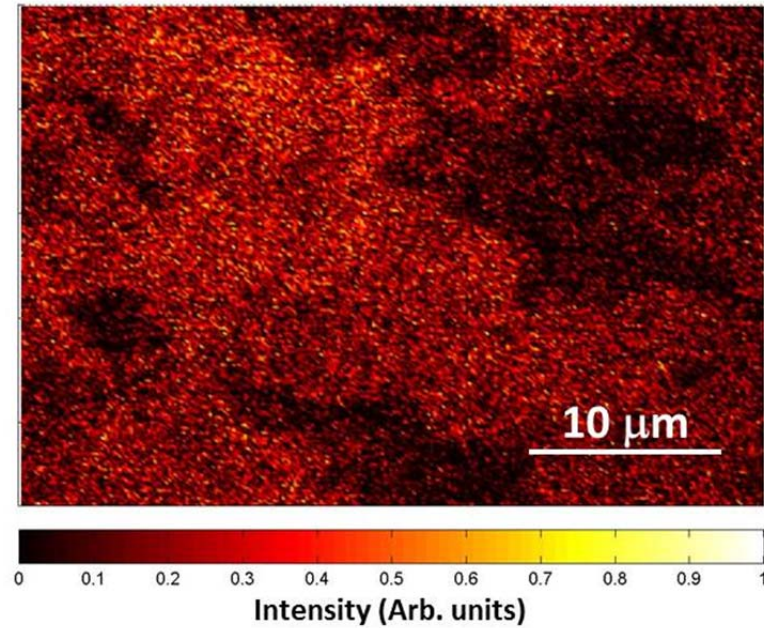


Figure 10. Cathodoluminescence map (false color) of TlBr sample 45-S10. Intensity variations are observed on a scale of ~ 10 μm .

CL spectra were measured for TlBr sample 45-S10 at 11 K and 295 K. For the CL system, the slits were set to 1 mm, and the step size was 1 nm.

The CL spectrum at 11 K is shown in Figure 11. Four peaks, labeled A through D, are observed: A at 411 nm (3.02 eV), B at 461 nm (2.69 eV), C at 477 nm (2.60 eV), and D at 691 nm (1.80 eV). Peaks A and B are consistent with reported values for the direct and indirect gap of TlBr at 3.02 eV and 2.68 eV, respectively [52]. The origin of peak C at 2.60 eV is unknown. Peak C may represent a phonon replica of the LO phonon associated with peak B. The energy separation between peaks A and B is 90 meV. Inelastic neutron scattering experiments in TlBr have shown energy separations between phonon replicas of 13.9 meV. Shimizu (1974), however, has observed 26 meV separations between successive photoluminescence peaks in TlBr [53]. Peak C may therefore represent the third phonon replica of peak A. The spectrum also shows a broad peak at 691 nm (1.80 eV), which can be attributed to defect-related luminescence.

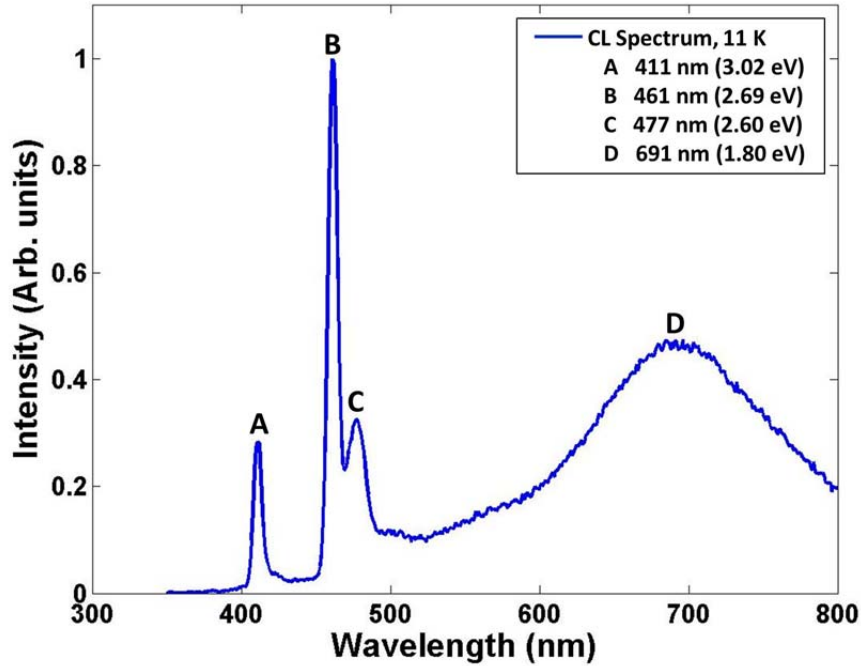


Figure 11. CL spectrum for TlBr sample 45-S10 at 11 K.

The CL spectrum at 295 K is shown in Figure 12. Gaussian fits to two peaks are included in the figure. Two features are noticeable in the room temperature spectrum.

First, a broad peak at 416 nm (2.98 eV) is now present in place of the sharp peak at 461 nm (2.69 eV) seen in the 11 K spectrum. Second, the defect luminescence peak is now located at ~ 575 nm (2.16 eV).

CL has been demonstrated in TlBr at both warm and cold temperatures. The CL peaks in TlBr are an unexplored area of research. To accurately assign all peaks, more detailed spectroscopy studies are required. For the purposes of transport imaging, however, there is a distinct luminescence signature, clearly attributable to bulk TlBr, which can be used to image carrier diffusion and recombination.

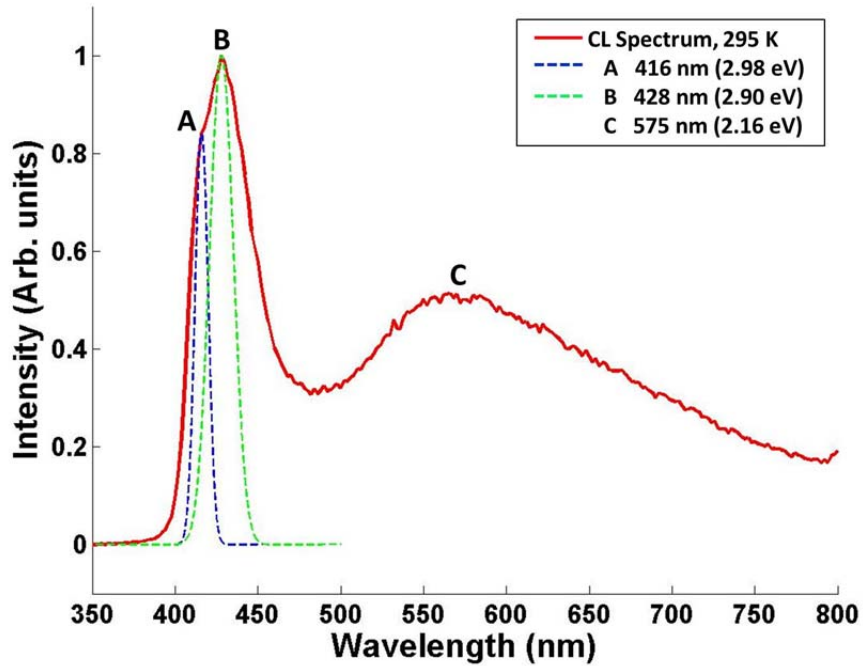


Figure 12. CL spectrum for TlBr sample 45-S10 at 295 K.

E. PHOTOLUMINESCENCE

Photoluminescence (PL) was also performed on sample 45-S10. The PL system, located at the University of California, Berkeley, is comprised of a HeCd laser with an excitation wavelength of 325 nm, a UV/VIS spectrometer with a Si PMT detector, a 385 nm cutoff filter, and a thermoelectric cooler. The laser was operated at maximum power of 50 mW, and measurements were recorded at a sample temperature of 10 K.

The PL spectrum and Gaussian fits to the peaks are shown in Figure 13. Six peaks, labeled A through F, were observed: A at 414 nm (3.00 eV), B at 428 nm (2.90 eV), C at 475 nm (2.61 eV), D at 487 nm (2.55 eV), E at 503 nm (2.47 eV), and F at 644 nm (1.93 eV).

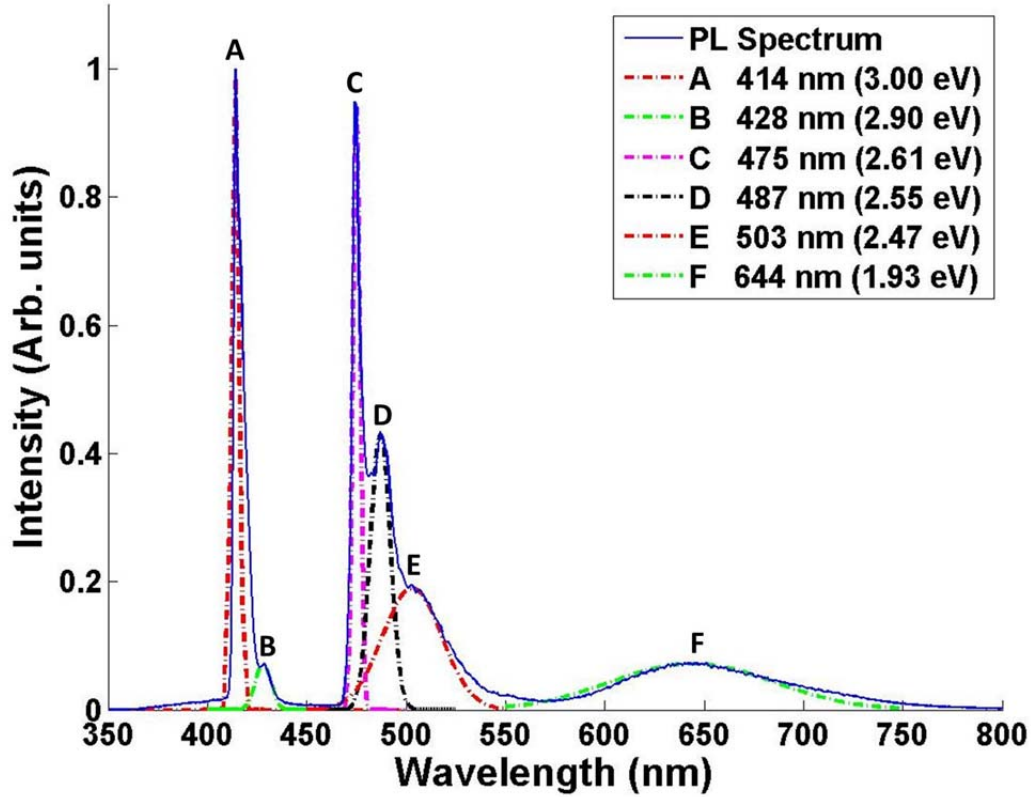


Figure 13. PL spectrum at 10 K for TlBr sample 45-S10. The dashed lines indicated Gaussian fits to the peaks.

Peaks A and C are consistent with the direct and indirect bandgaps for TlBr. The origins of peaks B, D, and E are unknown. The energy separation between peaks A and B is 98.0 meV. As suggested for the CL spectra, Peak B may represent a phonon replica of the LO phonon associated with peak A. Similarly, peaks D and E are separated from peak C by energies of 64.3 meV and 145 meV, respectively. These peaks could therefore represent phonon replicas of peak C. It is also possible, however, that peaks B, D, and E, are not phonon replicas. They could instead be associated with defect-mediated

recombination. Peak F is associated with broad defect luminescence. Further doping experimentation and detailed spectroscopy are required to determine what levels the impurities introduce into TlBr.

Figure 14 compares the CL and PL data for TlBr sample 45-S10. The CL and PL peaks at the direct gap (~ 3.0 eV) are closely matched. At the indirect gap, CL shows a peak at 2.69 eV (CL peak B), whereas PL shows a peak at 2.61 eV (PL peak C). The other peaks are more difficult to match. High resolution variable temperature CL and PL comparison studies are a prime area for future research.

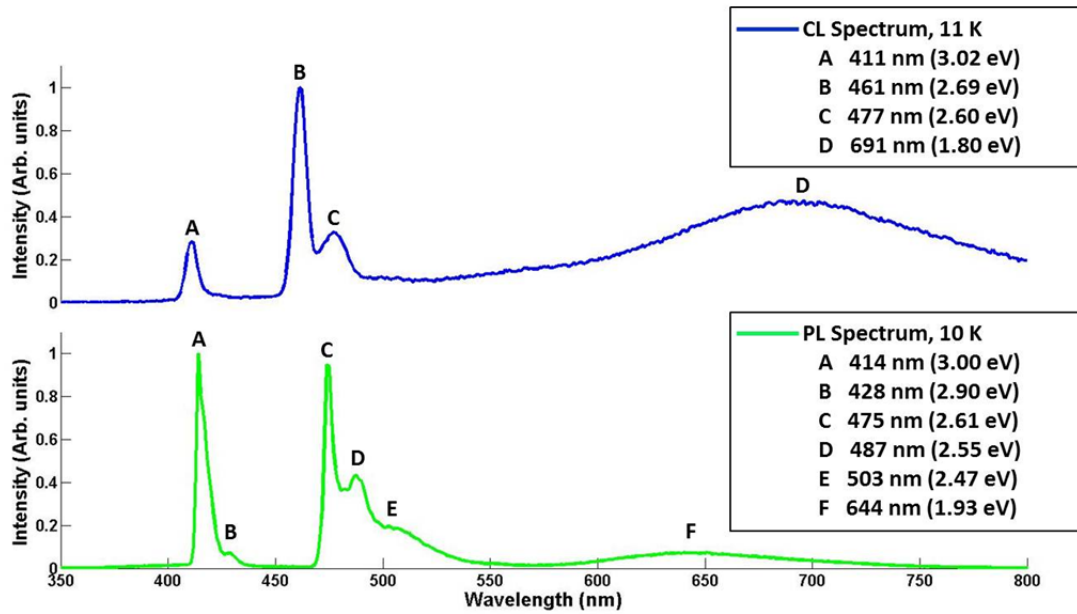


Figure 14. CL and PL spectra of TlBr sample 45-S10

F. ENERGY DISPERSIVE X-RAY SPECTROSCOPY

CL mapping shows spatial variations in the luminescence of the TlBr samples, but the technique does not give information as to any chemical origin of the variations. Energy dispersive X-ray spectroscopy (EDX) was performed to determine if the variations reflect non-uniform distribution of the impurities. In EDX analysis, an electron beam bombards a sample, and a detector records the characteristic X-rays emitted in order to determine the elemental composition of the sample. EDX was performed at 15.0 kV, 2000 \times magnification, and 295 K.

EDX mapping of TlBr sample 45-S10 was performed. Figure 15(a) shows the distribution of $M \alpha_1$ X-rays from thallium. Figure 15(b) shows the distribution of $L \alpha_{1,2}$ X-rays from bromine. Both distributions are uniform. This indicates that the thallium and bromine are uniformly mixed, as expected, or that the non-uniformity is below the detection limit for EDX (0.1–1 at. %) [54].

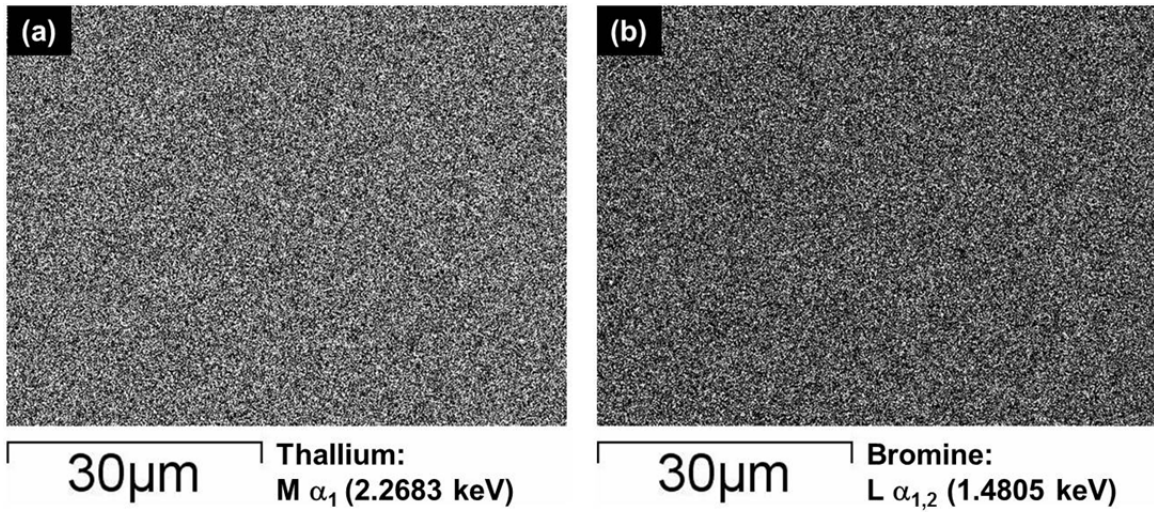


Figure 15. EDX map for (a) thallium and (b) bromine.

The characteristic X-ray spectrum for the TlBr sample is shown in Figure 16. EDX spectroscopy primarily detected characteristic X-rays from thallium and bromine. No other elements were detected above the EDX detection limits. This is consistent with the GDMS results, which shows dopant/impurity levels below 10^{19} cm^{-3} .

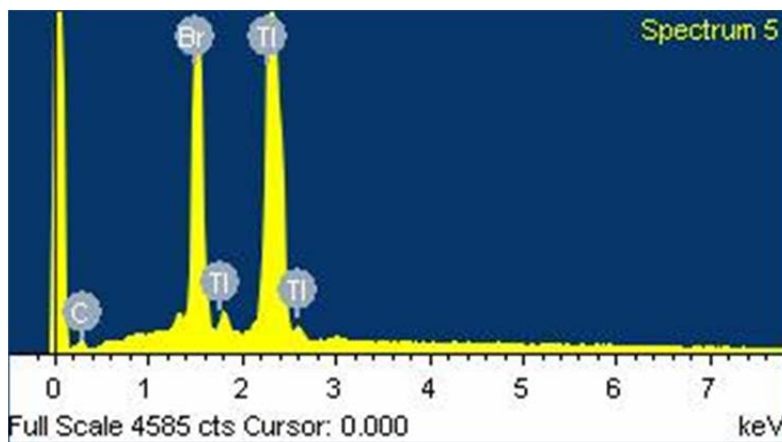


Figure 16. EDX spectrum for TlBr sample 45-S10.

G. TIME-OF FLIGHT SECONDARY ION MASS SPECTROMETRY

In order to better understand the origin of the spatial variation observed in the CL maps, time-of-flight secondary ion mass spectrometry (TOF-SIMS) mapping was performed by EAG. The author traveled to the laboratories of EAG in Sunnyvale, CA, to observe the analysis.

TOF-SIMS focuses a pulsed beam of Ga ions onto the surface of the sample. Secondary ions are generated by a sputtering process. Mass spectrometry then provides information about the molecular and elemental species present on the surface. The detection limit is 10^7 – 10^{10} at/cm² sub-monolayer. For mapping, the ion beam is rastered across the surface of the sample. The lateral resolution is ~ 0.20 μm [55]. The samples were sputtered for 70 ns, with surface removal rate of ~ 1 angstrom/second, resulting in a total material removal to a depth of ~ 7 nm. Typically, the sputtering process removes contaminants on the surface.

Figure 17 shows TOF-SIMS maps for thallium and bromine in TlBr sample 45-S10. Figures 17(a) and 17(c) show maps for thallium and bromine prior to sputtering, and Figures 17(b) and (d) shown maps for thallium and bromine after sputtering. In each case, the maps of the unsputtered surfaces depict large intensity variations. This indicates that either the surface has contaminants that prevent detection of an underlying uniform thallium bromide matrix, or that the thallium bromide matrix itself is not homogenous,

with regions of high thallium or bromine concentration in one location, and regions of low concentration in another location. The maps of the sputtered surfaces are nearly uniform in their intensities, with some darker lines that may reflect scratches on the surface. The uniformity of the intensity indicates that the thallium bromide matrix is largely homogenous, and that the sputtering process has removed surface contamination.

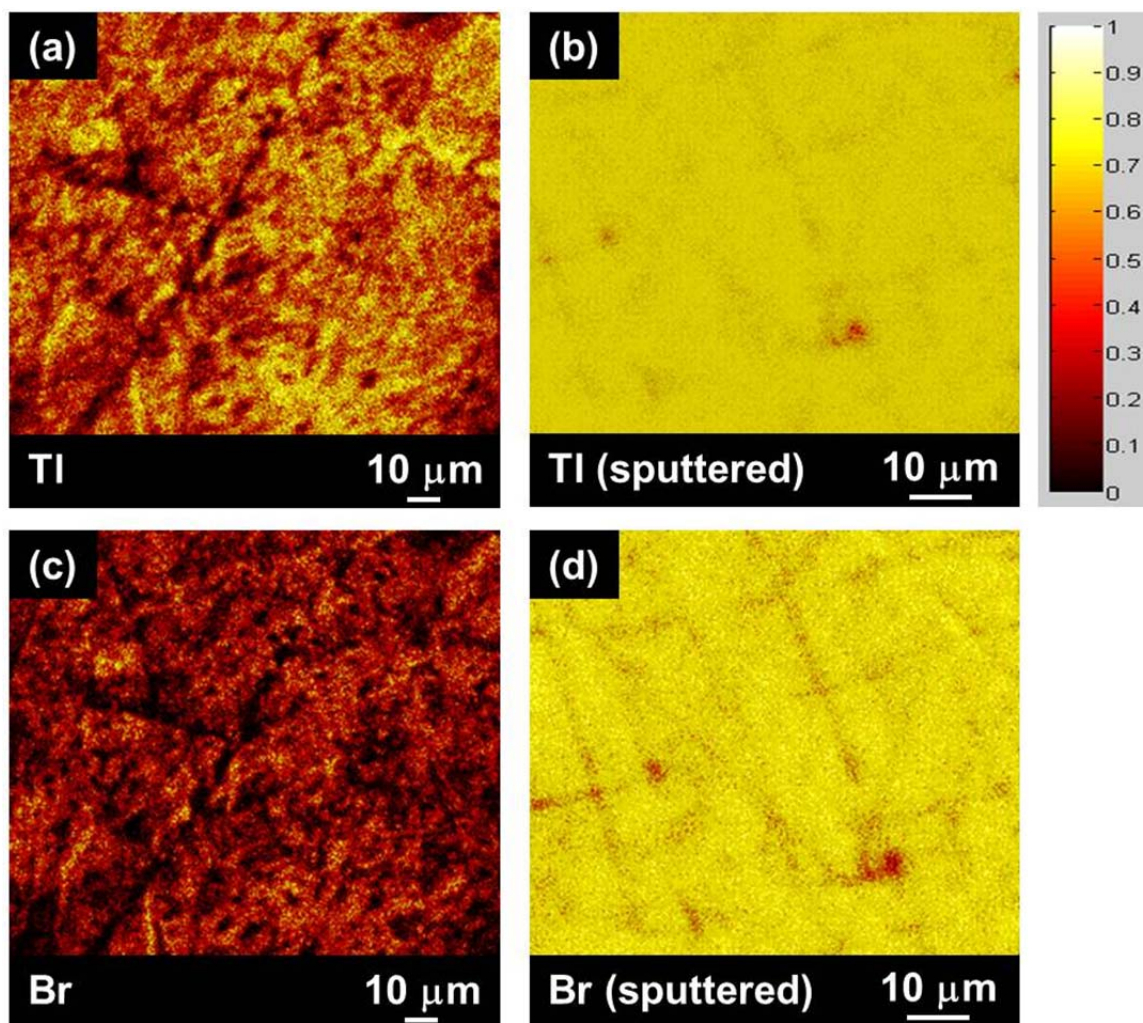


Figure 17. TOF-SIMS mapping showing elemental distribution of (a) thallium prior to sputtering, (b) thallium after sputtering, (c) bromine prior to sputtering, and (d) bromine after sputtering.

TOF-SIMS maps for Na, Ca, K, Cu, F, and Cl are shown in Figure 18. For each element, an unsputtered and sputtered image is shown. Sputtered images for Na, Ca, and

K shown in Figure 18(b), (d), and (f) all depict intensity variations on a scale of $\sim 10\text{--}20\text{ }\mu\text{m}$. This indicates nonuniformity in the distribution of these impurities. The intensity for Cu in Figure 18(g) and (h) is low, but the sputtered image appears to depict some nonuniformity. For F and Cl, and sputtered images in Figure 18(j) and (i) also show low intensity variation, again indicating nonuniformity in impurity distribution.

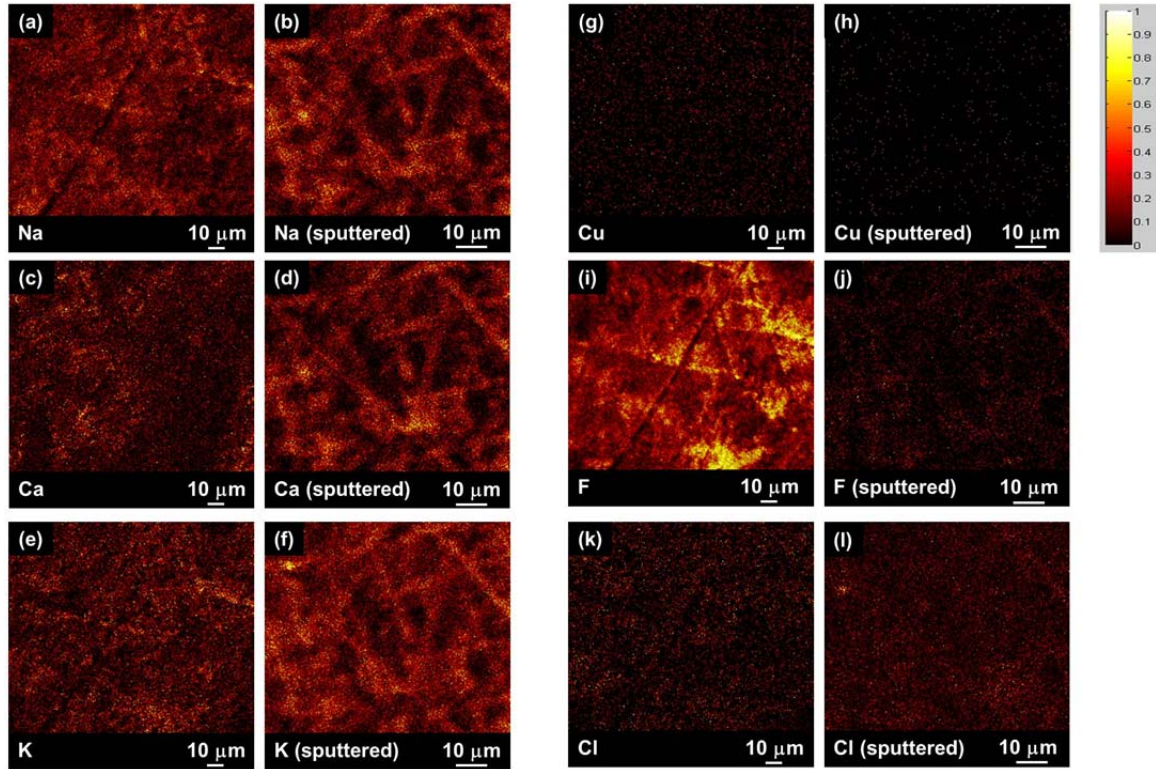


Figure 18. TOF-SIMS mapping showing elemental distributions Na, Ca, K, Cu, F, and Cl before and after sputtering.

H. TRANSPORT IMAGING—TEMPERATURE DEPENDENCE

For transport imaging on TlBr sample 45-S10, the effect of SEM operating current first was investigated in order to determine the optimum operating parameters. Figure 19 shows a comparison of the intensity distributions at 20.0 keV for currents of 1×10^{-10} A, 3×10^{-10} A, and 6×10^{-10} A for 100 lines averaged from a line scan. The distributions show good reproducibility for currents of 3×10^{-10} A, and 6×10^{-10} A. An operating current of 1×10^{-10} A shows higher variations in the distribution beginning at

about 30 μm from the peak, possibly attributable to increased noise and background effects. Higher beam currents introduce undesirable surface effects due to local heating, whereas lower beam currents reduce the intensity to such a level that focusing the instrument is difficult. As a result, an operating current of 3×10^{-10} A was found to be optimal, and it was used whenever possible.

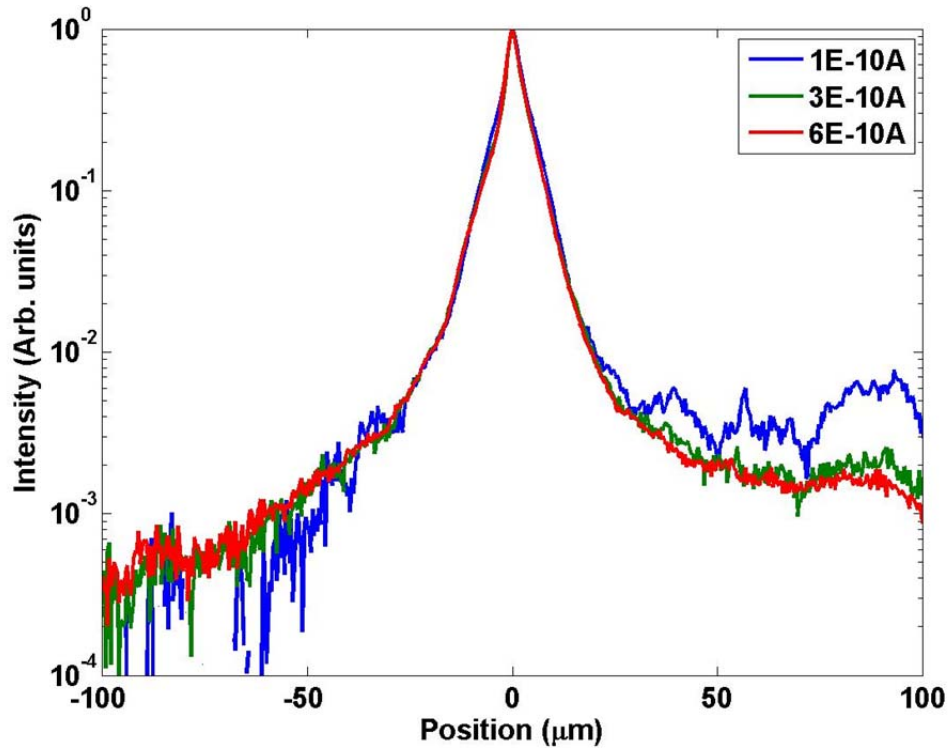


Figure 19. Evaluation of effects of beam current on intensity distribution at 20.0 keV in TlBr sample 45-S10.

The effects of temperature on transport properties in TlBr sample 45-S10 were also studied. Figure 20 shows the normalized mean intensity distributions for 10 different temperatures. The SEM operating parameters were 20.0 keV and 3×10^{-10} A. The variation with temperature indicates that bulk material properties are playing a measurable role in the luminescence distribution.

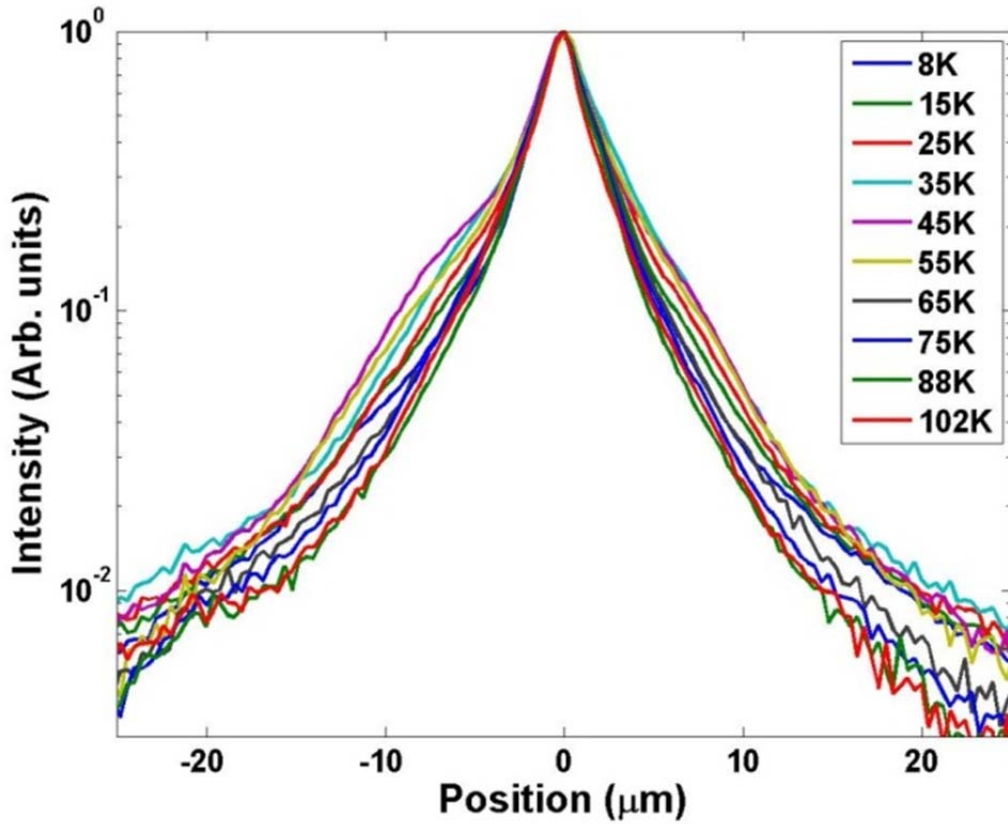


Figure 20. Normalized mean intensity distributions for TlBr sample 45-S10 for temperatures between 8 K and 102 K.

Figure 21 shows a representative fit of the data at a temperature of 8 K. As highlighted in the semilog plot in Figure 21(b), the fit deviates from the data at $\sim 15 \mu\text{m}$ from the source. The cause of this deviation has not yet been resolved, but it may be due to background subtraction limitations.

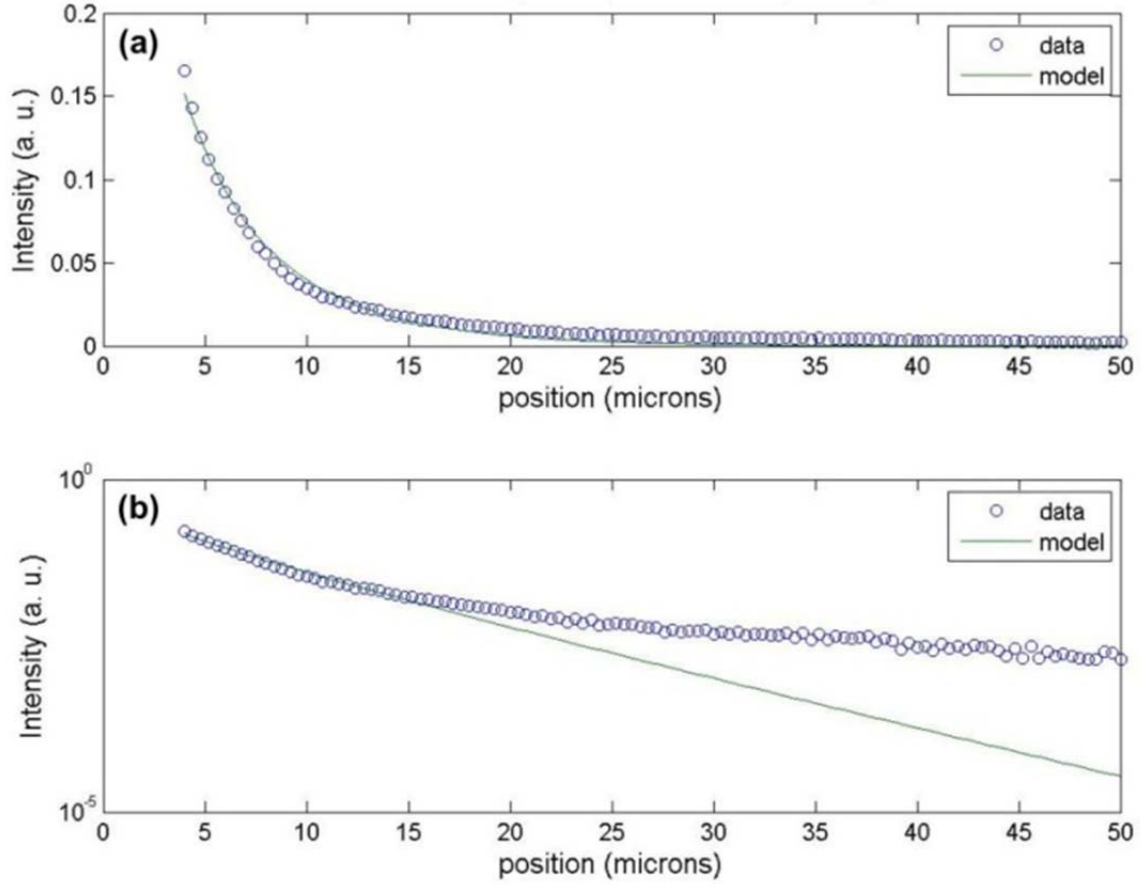


Figure 21. Fit to TlBr sample 45-S10 at 8 K shown on (a) linear and (b) logarithmic scale.

Figure 22 shows plots of temperature vs. diffusion length and temperature vs. $\mu\tau$ product obtained by fitting the data in Figure 20 to the model. The $\mu\tau$ product decreases with increasing temperature over the range of 8 K–102 K. Owens (2003) and Onodera (2007) have reported on the temperature dependence of the $\mu\tau$ products for electrons and holes over temperature ranges of 265 K–278 K and 233 K–313 K, respectively [56], [57]. To the author's knowledge, this work presents the first report of the ambipolar $\mu\tau$ product over the range of 8 K–102 K.

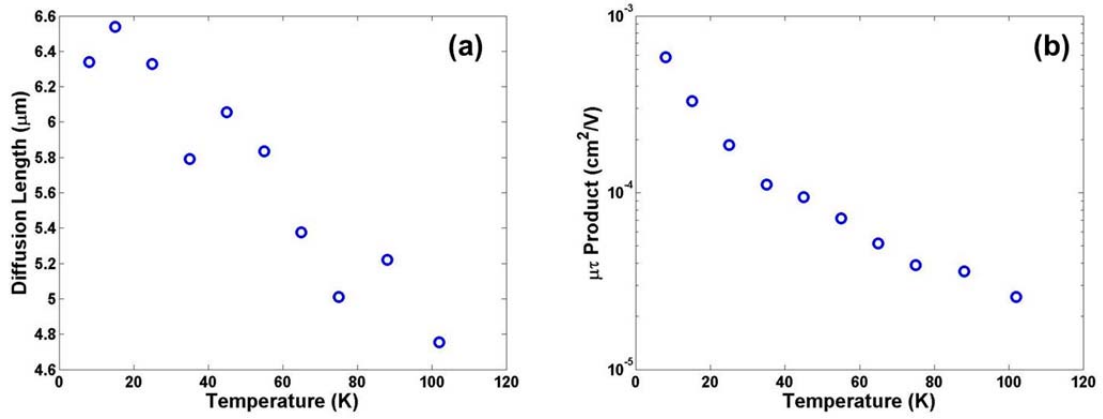


Figure 22. Temperature dependence of (a) diffusion length and (b) $\mu\tau$ product for TlBr sample 45-S10.

Based on these initial results, which demonstrated the feasibility of bulk transport imaging in TlBr, further studies were performed to investigate the effects of doping and spatial variations.

THIS PAGE INTENTIONALLY LEFT BLANK

V. THALLIUM BROMIDE SAMPLES ZRC0937-07 AND ZRC0937-08

A. CRYSTAL GROWTH

RMD provided slices from two different TlBr crystals doped with different impurities. RMD grew these crystals to investigate the efficiency of zone refining in removing various impurities. A synthesized 5N purity TlBr compound was purchased from a commercial vendor and used as the starting material. Crystal ZRC0937-07 was doped 1% atomic with 5N purity beads of NaBr, AlBr₃, and AgBr. This crystal will be referred to as “Na/Al/Ag doped.” Crystal ZRC0937-08 was doped 1% atomic with 5N purity beads of CuBr₂, FeBr₂, and ZnBr₂. This crystal will be referred to as “Cu/Fe/Zn doped.” Each crystal was sealed in a 10-mm diameter ampule under HBr atmosphere. The crystals were zone refined in a horizontal configuration for 100 passes using a travelling molten zone method. Crystal growth was done as a last step at a slow speed to promote single crystal growth. The grown crystals were cut into ~1-mm thick slices using a diamond wire saw. The slices were grinded with a 30 microns alumina grit slurry to remove surface damages due to the wire saw cutting. They were then polished with a 0.9 microns alumina grit slurry. The slices were etched with 2% Br in methanol. The grown crystals in their sealed ampules are shown in Figure 23.

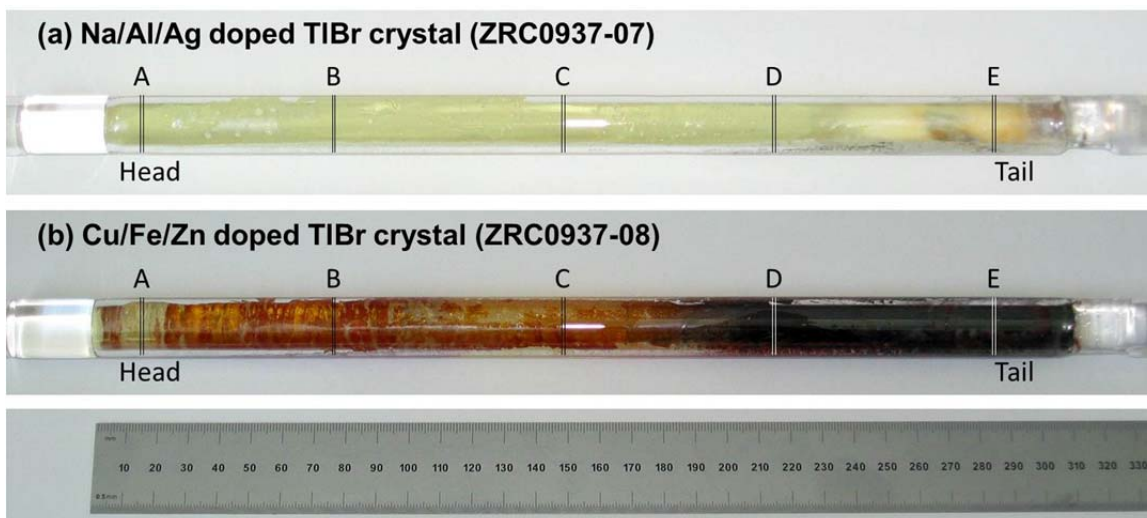


Figure 23. (a) Na/Al/Ag doped TlBr crystal (ZRC0937-07) and (b) Cu/Fe/Zn doped TlBr crystal (ZRC0937-08). The head region of each crystal contains fewer impurities than the tail region.

Due to the segregation of impurities during zone refining, the head region of each crystal contains lower impurity concentrations than the tail region. RMD provided slices from different regions of the crystal for analysis. For the Na/Al/Ag doped crystal, RMD provided slices A and D, as shown in Figure 23(a). For the Cu/Fe/Zn doped sample, RMD provided slices A, C, and D, as shown in Figure 23(b).

B. GLOW DISCHARGE MASS SPECTROMETRY

RMD had EAG perform GDMS on TlBr slices near to the ones provided here for analysis. Figures 24(a) and (b) show the GDMS results for the Na/Al/Ag doped TlBr crystal and the Cu/Fe/Zn doped TlBr crystal, respectively.

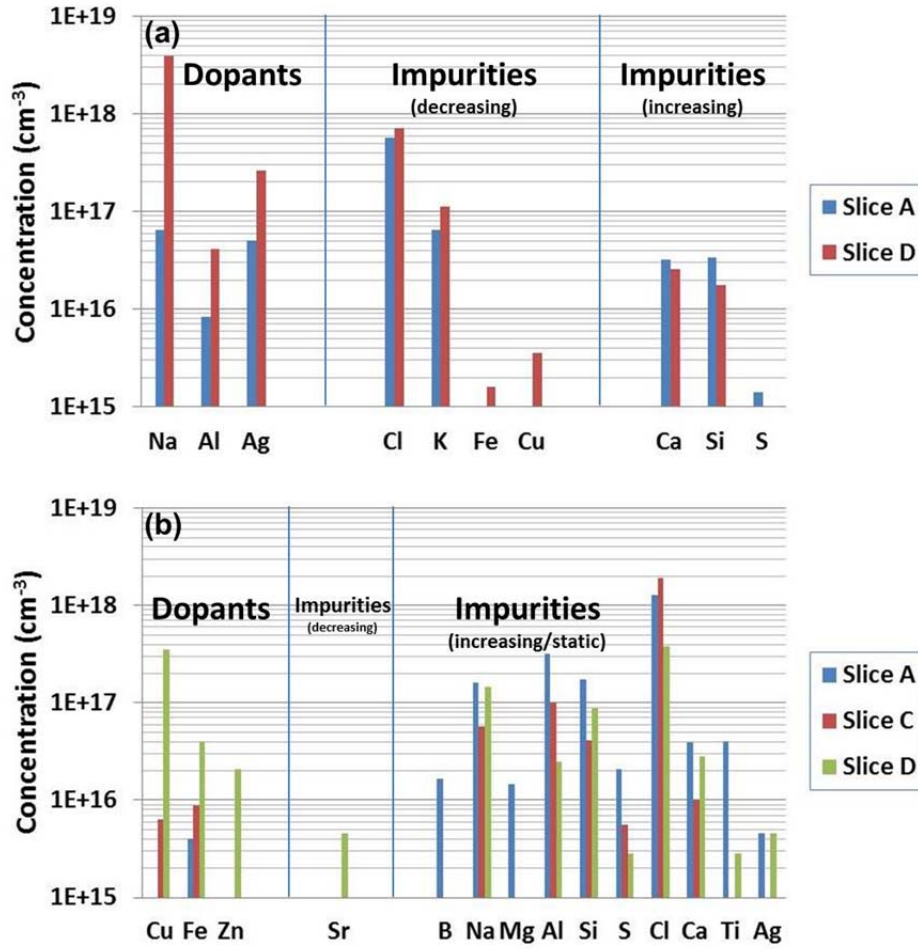


Figure 24. GDMS results for (a) Na/Al/Ag doped TlBr and (b) Cu/Fe/Zn doped TlBr crystal.

Figure 24(a) shows that concentrations of the dopants Na, Al, and Ag decrease from slice D to A (tail to head) in the Na/Al/Ag doped TlBr crystal. The majority of the impurities in this crystal also decrease in concentration from slice D to A. Figure 24(b) shows that the concentrations of dopants Cu, Fe, and Zn in the Cu/Fe/Zn doped TlBr crystal also decrease from slice D to A. The majority of the impurities in this crystal, however, increases in concentration or remain the same from slices D to A. The GDMS data indicates that these crystals, although zone refined, still have high concentrations of both dopants and impurities.

C. CATHODOLUMINESCENCE

Room temperature (295 K) CL mapping was performed on slices A and D of the Na/Al/Ag doped TlBr crystal and on slices A and C of the Cu/Fe/Zn doped TlBr samples, as shown in Figure 25. The SEM operating parameters were 20.0 kV, 1×10^{-9} A, and $2000\times$ magnification. The CL system was operated in panchromatic mode to capture emitted light at all wavelengths. The samples with higher impurity concentrations (slice D of Na/Al/Ag doped TlBr and slice C of Cu/Fe/Zn doped TlBr) show intensity variations on a scale of $\sim 10\ \mu\text{m}$.

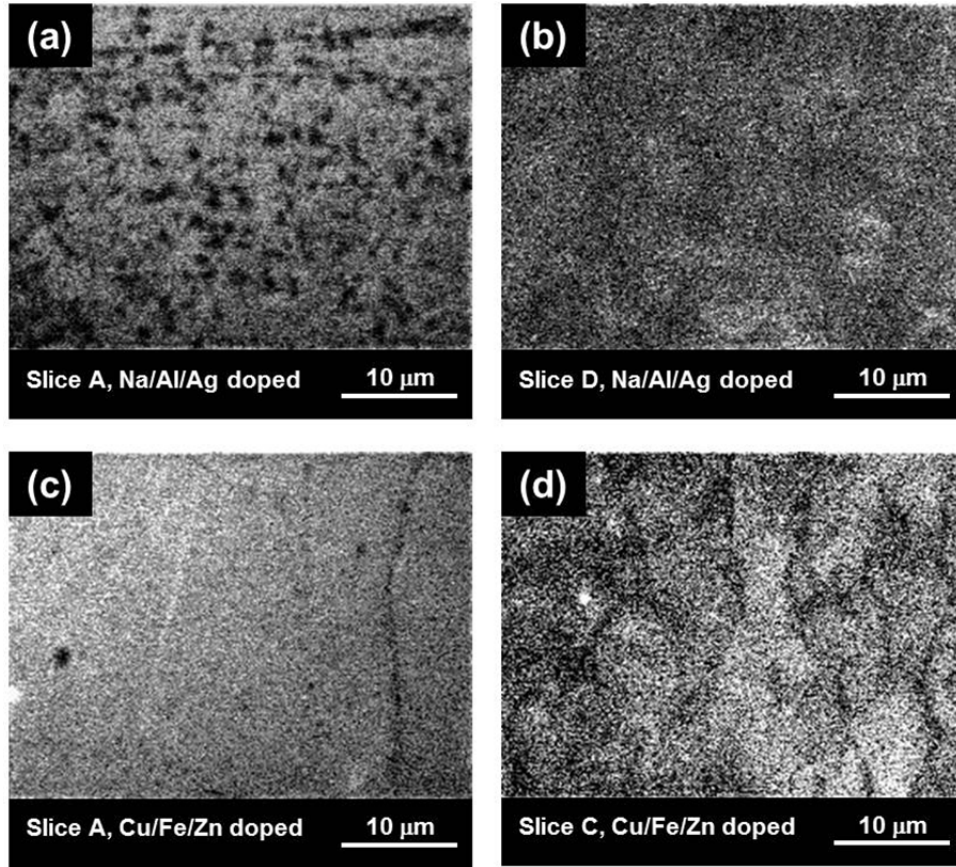


Figure 25. CL map at 295 K of (a) slice A and (b) slice D of Na/Al/Ag doped TlBr and (c) slice A and (d) slice C of Cu/Fe/Zn doped TlBr.

The room temperature luminescence patterns differ for slices A and C of the Cu/Fe/Zn doped TlBr, as seen in Figure 25(c) and (d). Slice A exhibits nearly uniform

intensity, whereas slice C shows spatial variations in the intensity on a scale of $\sim 10\ \mu\text{m}$. CL mapping was repeated on these two slices at 11 K with SEM operating parameters of 20.0 kV, 3×10^{-10} A, and 2000 \times magnification. The CL system was set to 460 nm (2.70 eV) to capture band edge luminescence. The CL maps are shown in Figure 26. Both slices now show intensity variations on a scale of $\sim 10\ \mu\text{m}$.

Slice A of the Cu/Fe/Zn doped sample showed uniform intensity at room temperature, as seen in Figure 25(c), but spatial variation at 11 K, as seen in Figure 26(a). It is likely that slice A is actually non-uniform in material composition, but that the intensity of light emitted at 295 K is simply too low to reflect this non-uniformity. It is also possible that slice A has regions that are more uniform than others, and that the CL map at 295 K was taken from one of these more uniform regions.

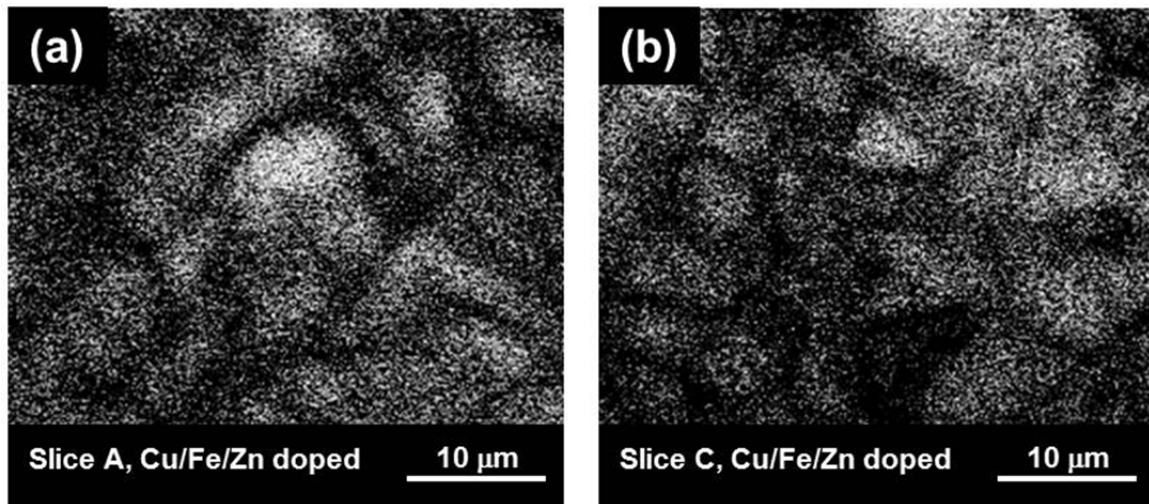


Figure 26. CL map for $\lambda = 460\ \text{nm}$ at 11 K of (a) slices A and (b) slice C of Cu/Fe/Zn doped TlBr.

CL spectra were measured for the Na/Al/Ag and Cu/Fe/Zn doped TlBr samples at 10 K or 11 K. The SEM operating parameters were 20.0 kV, 3×10^{-10} A, and 2000 \times magnification. For the CL system, the slits were set to 1.5 mm, and the step size was 1 nm. Figure 27(a-d) shows the CL spectra. All four spectra show the direct band gap at $\sim 410\ \text{nm}$ (3.02 eV) and the indirect band gap at $\sim 460\ \text{nm}$ (2.70 eV).

D. PHOTOLUMINESCENCE

PL was also performed on the Na/Al/Ag and Cu/Fe/Zn doped samples at 11 K using the PL system at the University of California, Berkeley. Figure 27(e-f) shows the CL spectra. All four spectra show the direct band gap at ~ 415 nm (3.00 eV) and the indirect gap at ~ 475 nm (2.61 eV). One sees that the midgap defect luminescence is more prominent in the CL spectra. This is most likely due to the larger energy density created by electron beam excitation, resulting in more phonon-assisted transitions. This should be a topic of further study.

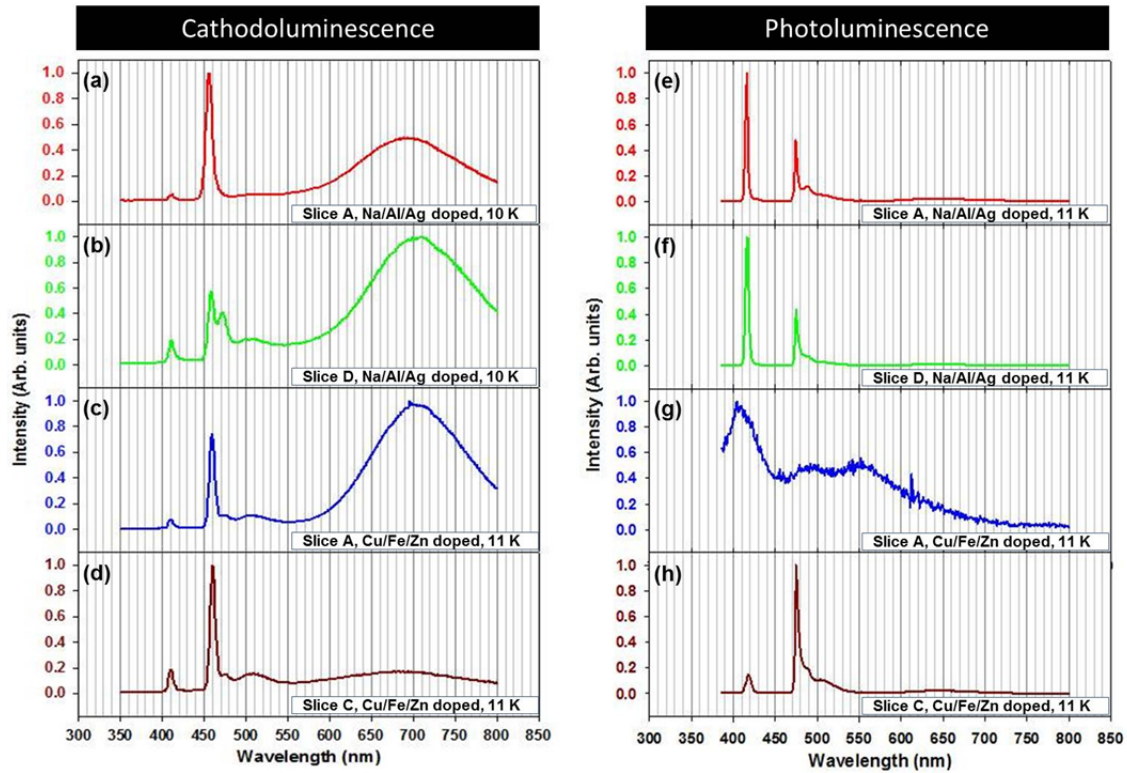


Figure 27. (a-d) CL and (e-f) PL spectra for Na/Al/Ag doped TlBr and Cu/Fe/Zn doped TlBr.

E. TRANSPORT IMAGING

1. Effects of Doping

The effect of overall doping concentrations on transport properties at 5 K was studied in the Na/Al/Ag doped and Cu/Fe/Zn doped TlBr crystal. First, single locations on each slice from each crystal were compared. Figure 28(a) shows a comparison of the averaged intensity distributions for slices A and D of the Na/Al/Ag doped TlBr crystal. Figure 28(b) shows a similar comparison for slices A and C of the Cu/Fe/Zn doped TlBr crystal. In each case, the intensity distribution is broader for slice A, the slice with the lower dopant concentration. This broadening indicates a larger $\mu\tau$ product, most likely associated with longer carrier lifetimes in the samples with lower impurity concentrations.

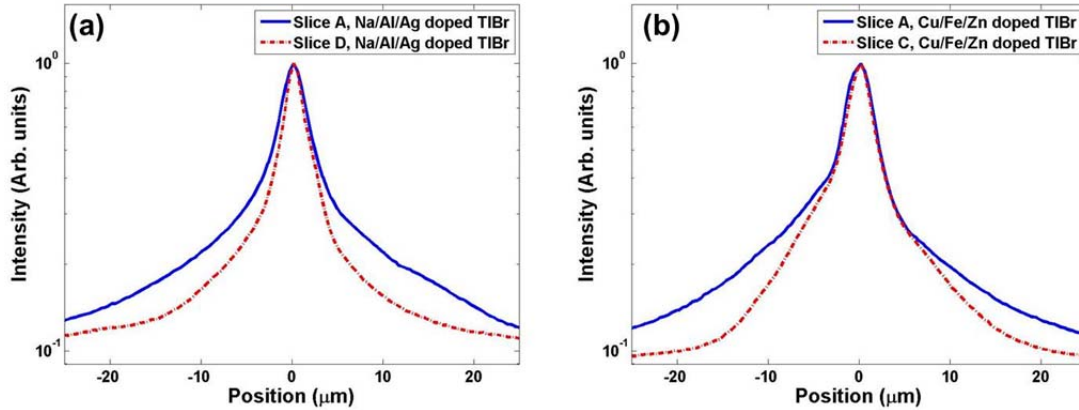


Figure 28. Comparison of the normalized mean recombination luminescence intensity distribution for (a) slices A and D of the Na/Al/Ag doped TlBr crystal, and (b) slices A and C of the Cu/Fe/Zn doped TlBr crystal. Note that the figures are plotted on a logarithmic scale to highlight small changes in the distributions.

Figure 29 shows the data and best fit lines from least square fitting to the model for slices A and D of the Na/Al/Ag doped TlBr crystal and for slices A and C of the Cu/Fe/Zn doped TlBr crystal. The first data point used for each fit is 4 μm from the source in order to avoid effects due to the generation volume created by the SEM beam.

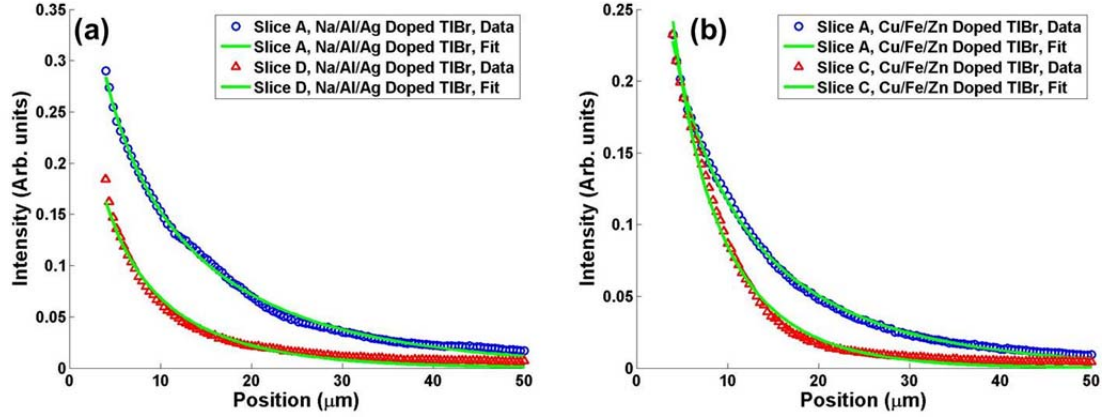


Figure 29. Data and least squares fitting to the model for (a) (a) slices A and D of the Na/Al/Ag doped TlBr crystal, and (b) slices A and C of the Cu/Fe/Zn doped TlBr crystal.

Table 2 shows the averaged ambipolar diffusion lengths and ambipolar $\mu\tau$ product for the four slices shown in Figure 29. The $\mu\tau$ product is higher in the samples with the lower impurity levels. This result is consistent with reported improvements in the electron $\mu\tau$ product and spectroscopic performance with improved material purification, although our measurements for the $\mu\tau$ product are dominated by the hole mobility, given the ambipolar nature of the diffusion [39], [40], [58], [59].

Table 2. GDMS dopant concentration, diffusion length, and $\mu\tau$ product at 5 K.

TlBr Crystal	Slice	GDMS Dopant Concentration (cm^{-3})			Diffusion Length, L_d (μm)	$\mu\tau$ Product (cm^2/V)
		Na	Al	Ag		
Na/Al/Ag doped	A	6.5×10^{16}	8.4×10^{15}	5.1×10^{16}	21	1.0×10^{-2}
	D	4.0×10^{18}	4.2×10^{16}	2.6×10^{17}	12	3.3×10^{-3}
Cu/Fe/Zn doped	A	$< 7.1 \times 10^{14} \text{ a}$	4.1×10^{15}	$< 6.9 \times 10^{14} \text{ a}$	18	7.7×10^{-3}
	C	6.4×10^{15}	9.0×10^{15}	$< 6.9 \times 10^{14} \text{ a}$	9.0	1.9×10^{-3}

^aBelow GDMS detection limit for given element

The data in Table 2 give a snapshot of the transport properties at one location on each slice and provide a gross estimate of how the transport properties change at different locations down the crystal ingot. The next step is to probe multiple locations on each slice to investigate how the uniformity of the $\mu\tau$ product varies within a slice.

Multiple random locations on each slice were sampled to investigate the uniformity of the $\mu\tau$ product across each slice. Figure 30(a) shows the intensity distributions for the Na/Al/Ag doped TlBr sample for slices A and D at random locations L1 and L2. Figure 30(b) shows the intensity distributions for the Cu/Fe/Zn doped TlBr sample for slices A, C, and D at random locations L1, L2, and L3.

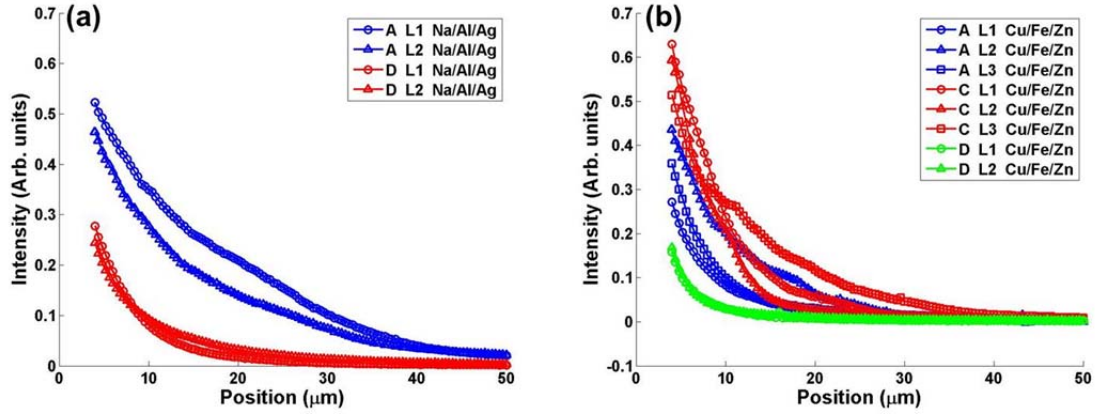


Figure 30. Intensity distributions on different slices (A, C, or D) for random locations (L1, L2, or L3) for (a) Na/Al/Ag doped and (b) Cu/Fe/Zn doped TlBr crystals at 5 K.

Figure 31 shows the extracted diffusion length for each slice from least squares fitting of the data to the model.

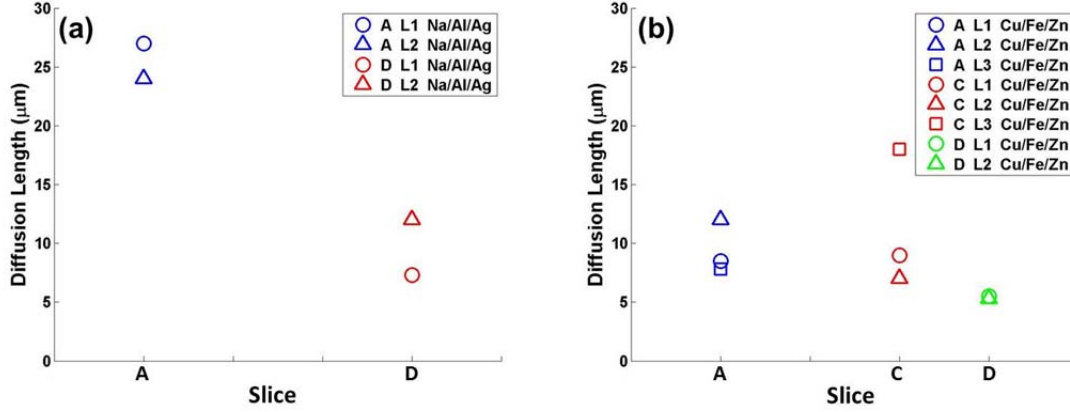


Figure 31. Diffusion lengths from different slices (A, C, or D) for random locations (L1, L2, and/or L3) for (a) Na/Al/Ag doped and (b) Cu/Fe/Zn doped TlBr crystals at 5 K.

The data from Figure 31 are re-plotted in Figure 32 to show the mean and one standard deviation of the diffusion length.

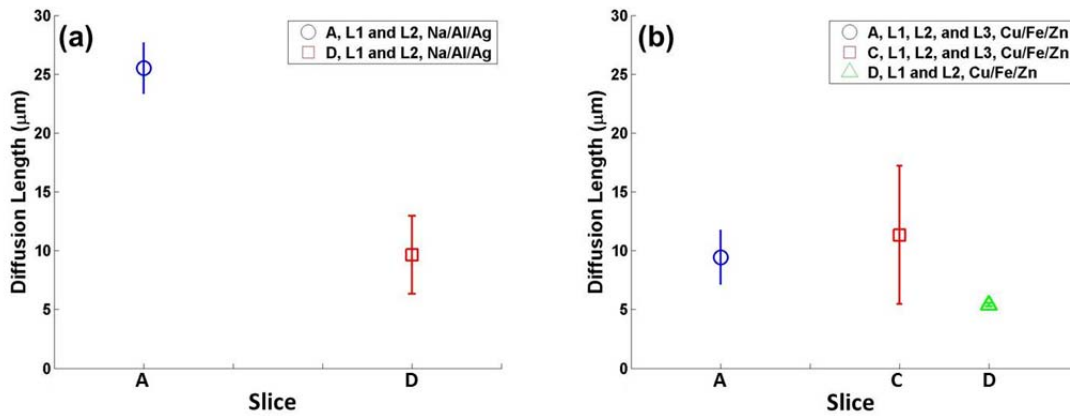


Figure 32. Diffusion lengths and one standard deviation from different slices (A, C, or D) for random locations (L1, L2, or L3) for (a) Na/Al/Ag doped and (b) Cu/Fe/Zn doped TlBr crystals at 5 K.

The data shown in Figures 31 and 32 are summarized in Table 3. The associated $\mu\tau$ products and one standard deviation are also shown in the table.

Table 3. Diffusion length and $\mu\tau$ product at different locations on different slices of doped TlBr crystals at 5 K.

TlBr Crystal	Slice	Location	Diffusion Length, L_d (μm)	$L_d \pm 1\sigma$ (μm)	$\mu\tau$ Product (cm^2/V)	$\mu\tau \pm 1\sigma$ (cm^2/V)
Na/Al/Ag doped	A	L1	27	26 ± 2	1.7×10^{-2}	$(1.5 \pm 0.3) \times 10^{-2}$
		L2	24		1.3×10^{-2}	
	D	L1	7.3	9.6 ± 3.3	1.2×10^{-3}	$(2.3 \pm 1.4) \times 10^{-3}$
		L2	12		3.3×10^{-3}	
Cu/Fe/Zn doped	A	L1	8.5	9.6 ± 2.5	1.7×10^{-3}	$(2.2 \pm 1.2) \times 10^{-3}$
		L2	12		3.6×10^{-3}	
		L3	7.8		1.4×10^{-2}	
	C	L1	9.0	11 ± 6	1.9×10^{-3}	$(3.4 \pm 3.4) \times 10^{-3}$
		L2	7.0		1.1×10^{-3}	
		L3	18		7.3×10^{-3}	
	D	L1	5.5	5.4 ± 0.2	7.1×10^{-4}	$(6.8 \pm 0.4) \times 10^{-4}$
		L2	5.3		6.5×10^{-2}	

We can draw several conclusions from the data in Table 3. For the Na/Al/Ag doped crystal, as we move down the crystal ingot from slice D to A (tail to head), the transport properties generally improve, consistent with overall reduction in impurity concentration due to zone refining. Within a slice, however, a comparison of the random locations shows that there is still significant variation in the transport properties across each slice. For the Cu/Fe/Zn doped sample, as we move down the crystal ingot from slice D to A, the transport properties do not strictly follow the expected trend of improvement. Instead, on average, slice C showed better transport properties than slice A. We can understand this variation by examining the transport properties of the random locations within slice C. Location 3 (L3) on slice C had a diffusion length double that of the other two locations on the slice. Most likely, L3 on slice C was a localized region of low dopant or impurity concentration. This again indicates significant variation in the

transport properties, most likely due to uneven distribution of dopants and impurities, both down the crystal ingot and across each slice.

The CL maps of TlBr in Figures 25 and 26 showed spatial variations in the intensity, indicating an uneven distribution of impurities or defects. The TOF-SIMS imaging in Figures 17 and 18 also depicted variations in the impurity distribution. Transport imaging on multiple locations on each slice as shown in Figure 31 and 32 and summarized in Table 3 indicates that variations in these impurities or defects affect transport properties in the semiconductor. The next step is to use transport imaging to probe the scale of these variations.

2. Spatial Variation in Diffusion Length and $\mu\tau$ Product

The ambipolar diffusion lengths and ambipolar $\mu\tau$ products reported in Tables 2 and 3 are average values over 40 μm regions of the TlBr slices at 5 K. By taking advantage of the resolution of the imaging system, however, we can obtain better spatial resolution. Transport imaging provides the ability to probe spatial variations in the diffusion length and $\mu\tau$ products at a resolution of 2 μm [60]. This micro-scale technique is demonstrated on slice C of the Cu/Fe/Zn doped crystal.

Figure 33(a) shows an optical image of a 60 $\mu\text{m} \times 85 \mu\text{m}$ SEM area luminescence scan at a random location on slice C of the Cu/Fe/Zn doped crystal at 5 K. The SEM operating parameters were 20.0 keV, 3×10^{-10} A, 2000 \times magnification. This image shows significant spatial variation on a scale of $\sim 10 \mu\text{m}$. The image was acquired by exposing the sample to the SEM beam and recording the resulting luminescence on the CCD camera with an exposure time of 600 s. This image is similar to a CL map, but slightly different in that the luminescence information is obtained during area SEM excitation, rather than point by point. The location of a 40 μm line scan is indicated in Figure 33(a) by the red line. The line scan image is shown in Figure 33(b). This image was acquired with an exposure time of 90 s. The line scan is divided into twenty sections, each 2 μm in length.

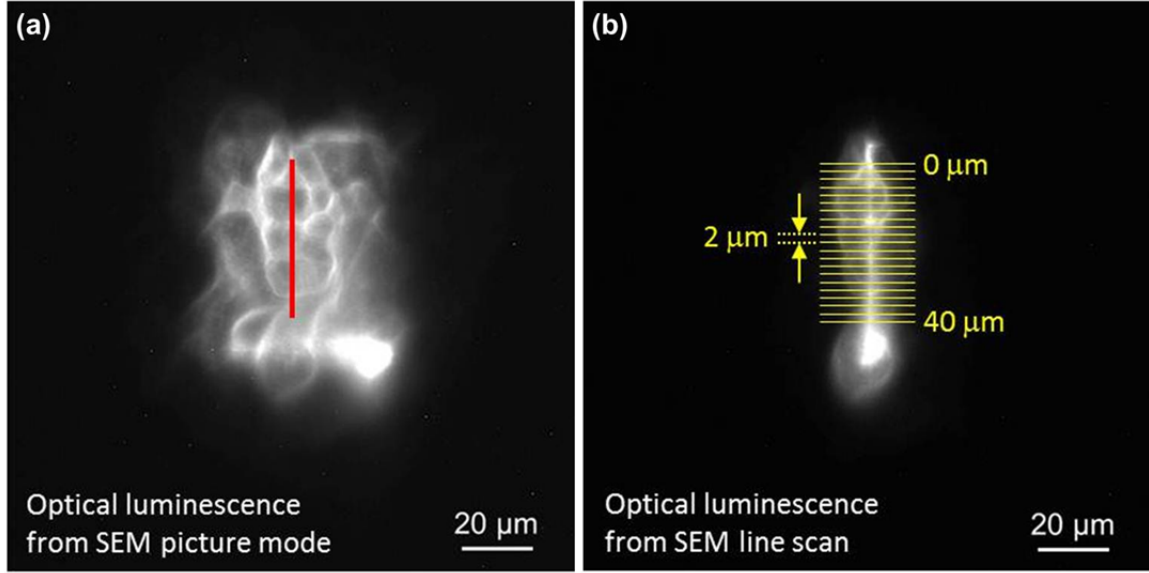


Figure 33. (a) SEM area luminescence scan of $60\text{ }\mu\text{m} \times 85\text{ }\mu\text{m}$ region of slice C of the Cu/Fe/Zn doped TlBr crystal. Intensity variations are visible on a scale of $\sim 10\text{ }\mu\text{m}$. The location of a $40\text{ }\mu\text{m}$ line scan is indicated by the white line. (b) SEM line scan, divided into $2\text{ }\mu\text{m}$ segments. After [60].

The ambipolar diffusion length is determined from the mean intensity distribution over each $2\text{-}\mu\text{m}$ section. The results are shown in Figure 34. The best-fit ambipolar diffusion lengths range from $4.6\text{ }\mu\text{m}$ to $11.2\text{ }\mu\text{m}$, with a mean of $7.1\text{ }\mu\text{m}$ and standard deviation of $2.0\text{ }\mu\text{m}$. The corresponding $\mu\tau$ products range from $4.9 \times 10^{-4}\text{ cm}^2/\text{V}$ to $2.9 \times 10^{-3}\text{ cm}^2/\text{V}$, with a mean of $1.3 \times 10^{-3}\text{ cm}^2/\text{V}$ and standard deviation of $6.8 \times 10^{-4}\text{ cm}^2/\text{V}$. These results demonstrate that, for these materials, CL luminescence variations are indicative of material variations that affect the ambipolar $\mu\tau$ product [60].

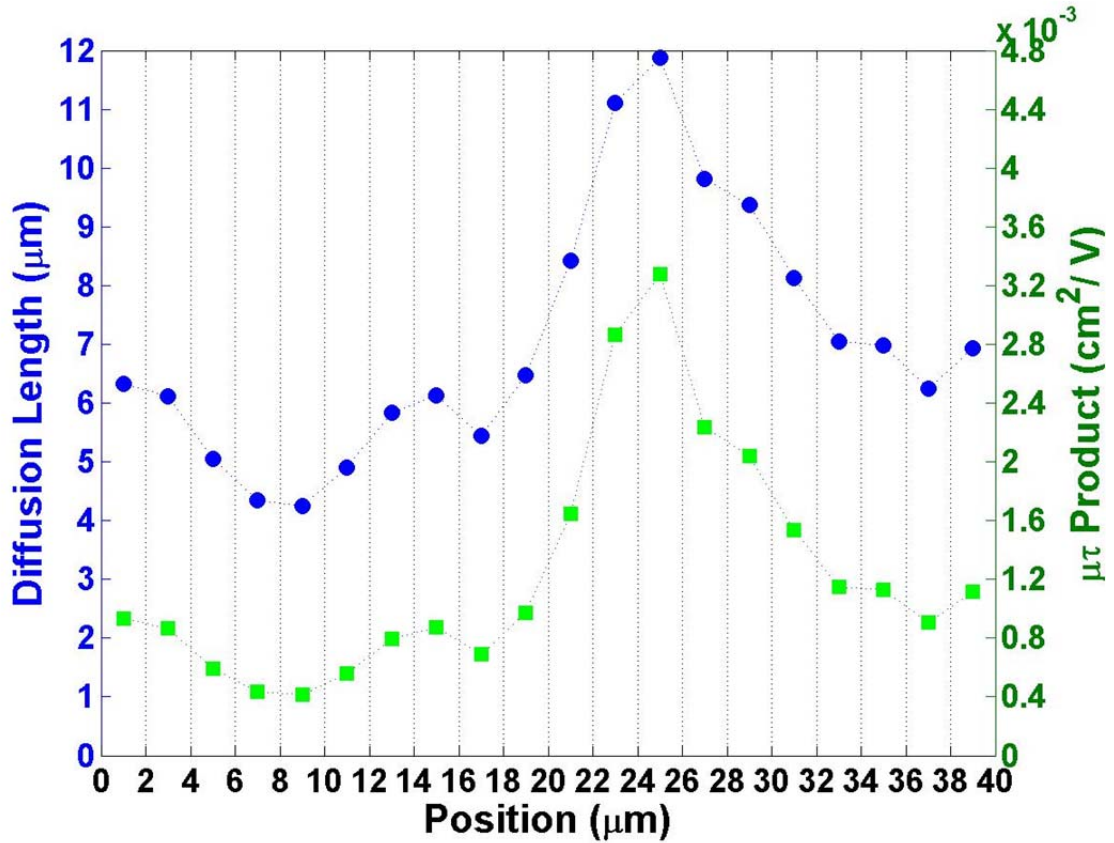


Figure 34. (b) Diffusion lengths are averaged over 2 μm sections of the line scan. The diffusion lengths vary between 4.6 μm and 11.2 μm , with a mean of 7.1 μm and standard deviation of 2.0 μm . After [60].

Crystal growers could use spatially resolved transport imaging as a micro-analysis technique to assess the quality of a crystal, without the need for contacts or device fabrication. Figure 35 shows a comparison of transport imaging for TlBr at 5 K and *n*-type GaAs at 295 K. The figure shows that TlBr has a higher diffusion length, but that the crystal contains regions of nonuniformity that will likely affect detector performance. In contrast, although the GaAs sample has a lower diffusion length, the material is more uniform. Transport imaging can therefore provide rapid, yet still quantitative, assessment of how variations in crystal growth affect material uniformity. Further investigation may also provide a way to correlate the variations observed in transport imaging with detector resolution.

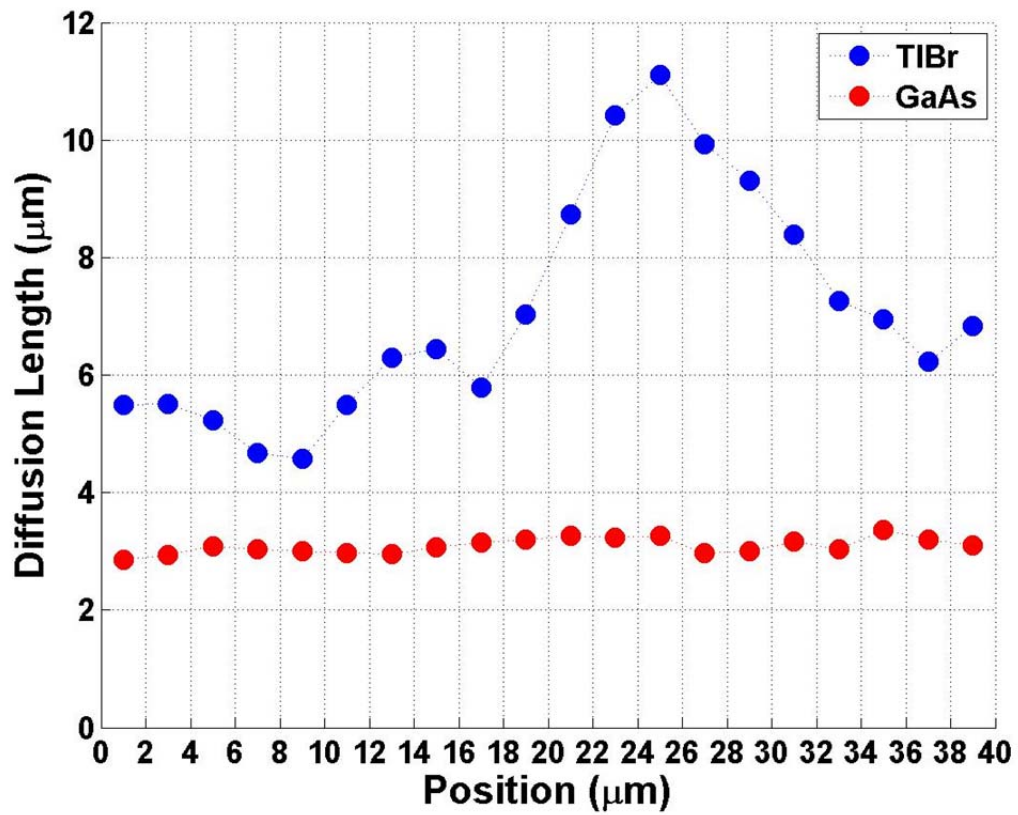


Figure 35. Variations observed in diffusion length in TlBr and GaAs using spatially resolved transport imaging.

THIS PAGE INTENTIONALLY LEFT BLANK

VI. DEFECT STUDY IN SELENIUM AND LEAD-DOPED THALLIUM BROMIDE

A. DEFECT LEVELS

The level of numerous defect states in the bandgaps of Ge, Si, and GaAs are well known. Figure 36 shows a typical impurity level diagram for Ge. Diagrams like this have emerged as a result of over 40 years of research in Ge crystal growth, diffusion behavior, and materials characterization. For TlBr, however, theoretical and experimental research on the location of impurity levels is just now beginning to emerge [46], [61]. Cathodoluminescence in TlBr doped with Se and Pb can contribute to an understanding of the location of these impurity levels.

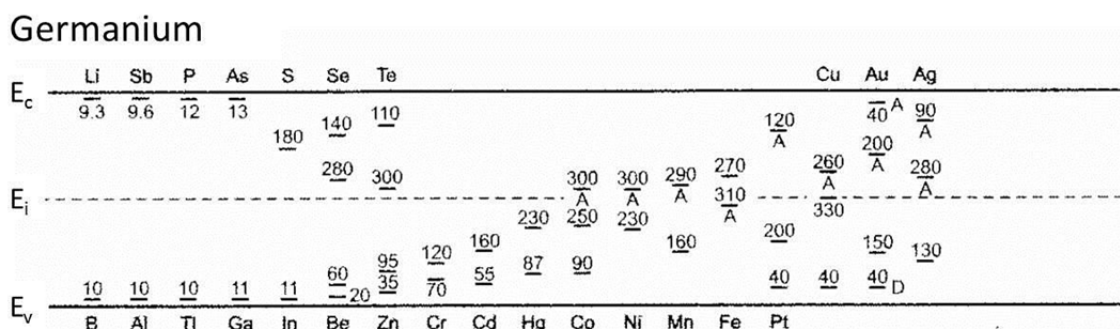


Figure 36. Impurity levels in Ge. The ionization energies are labeled in meV.
 Levels above the gap center (E_i) are donors, unless denoted as an acceptor (A).
 Levels below the gap center are acceptors, unless denoted as a donor (D).
 After [47].

B. CRYSTAL GROWTH

TlBr crystals doped with either Se or Pb were investigated in this study. The crystals were grown by RMD using the Vertical Bridgeman technique. One crystal was nominally doped with 100 ppm Tl_2Se , and the other crystal was nominally doped with 100 ppm PbBr_2 . The crystals are shown in Figure 37. The figure shows the grown crystals and the approximate locations of the slices, indicated by red lines. For each crystal, slice C1 was used for our analysis.

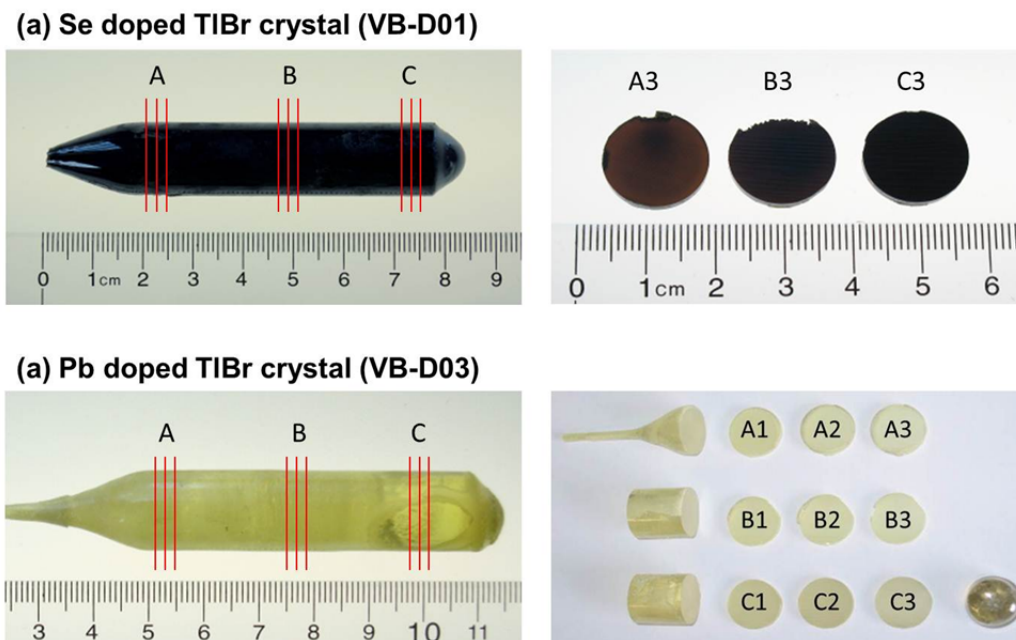


Figure 37. TlBr crystals doped with either Se or Pb. Approximate locations of slices are shown in red. (a) For the Se doped TlBr crystal, slice C3 is shown, although slice C1 was used in this study. (b) For the Pb doped TlBr crystal, slice C1 was used.

C. GLOW DISCHARGE MASS SPECTROMETRY

GDMS was performed by EAG on the Se and Pb doped TlBr crystals. For the Se doped crystal, GDMS was performed on slice C1, the same slices used in this study. For the Pb doped crystal, GDMS was performed on slice C2, the slice next to the one used in this study. The GDMS results are shown in Figure 38. The Se doped crystal shows high levels of both Se and Cl. The Pb doped crystal shows high levels of Pb, C, N, and Cl.

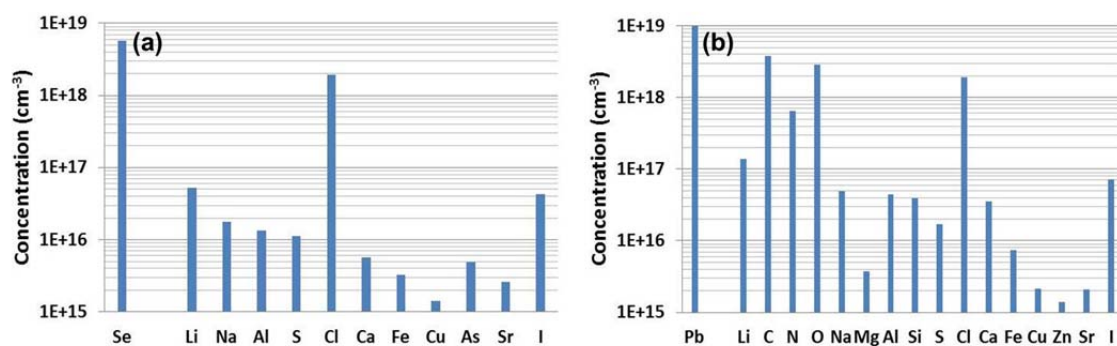


Figure 38. GDMS results for (a) Se doped TlBr and (b) Pb doped TlBr crystal.

D. CATHODOLUMINESCENCE

Room temperature (295 K) and low temperature (5 K) CL spectroscopy were performed on the Se and Pb doped TlBr slices to confirm the presence of a CL signature. The SEM operating parameters were 1×10^{-9} A and $500\times$ magnification. The spectra for the Se and Pb doped TlBr slices are shown in Figure 39. The spectrum for the Pb doped sample in Figure 39(b) includes Gaussian fits to peak C and D.

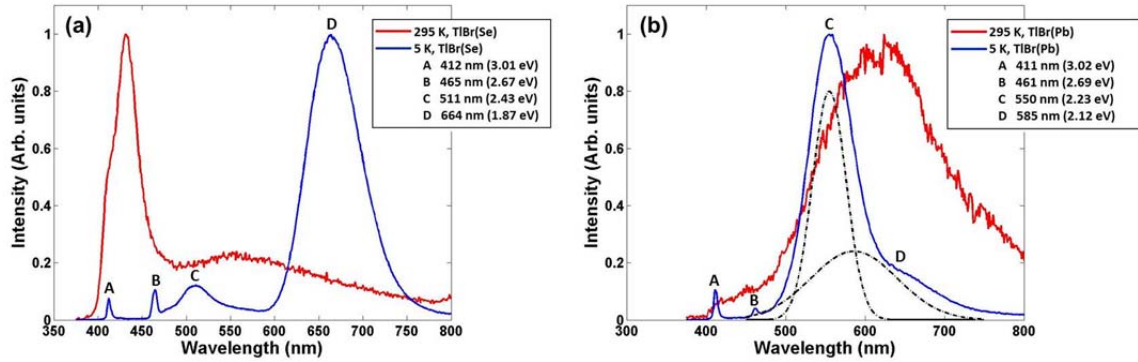


Figure 39. CL spectra at 295 K and 5 K for (a) Se doped TlBr and (b) Pb doped TlBr. A Gaussian fit to peak D is shown as a dashed line.

Figure 40 compares the spectra for the Se and Pb doped samples at 5 K. The Se doped sample shows peaks at 3.01 eV and 2.67 eV (A and B) due to direct and indirect excitons [53]. The spectrum also shows a defect peak at 2.43 eV (C) and a wide defect band at 1.87 eV (D). The Pb doped sample also shows the direct and indirect peaks at 3.02 eV and 2.69 eV (A and B). The peak at 2.43 eV observed in the Se doped sample is absent. The Pb doped sample shows additional peaks at 2.23 eV (C) and 2.12 eV that were not observed in the Se doped sample.

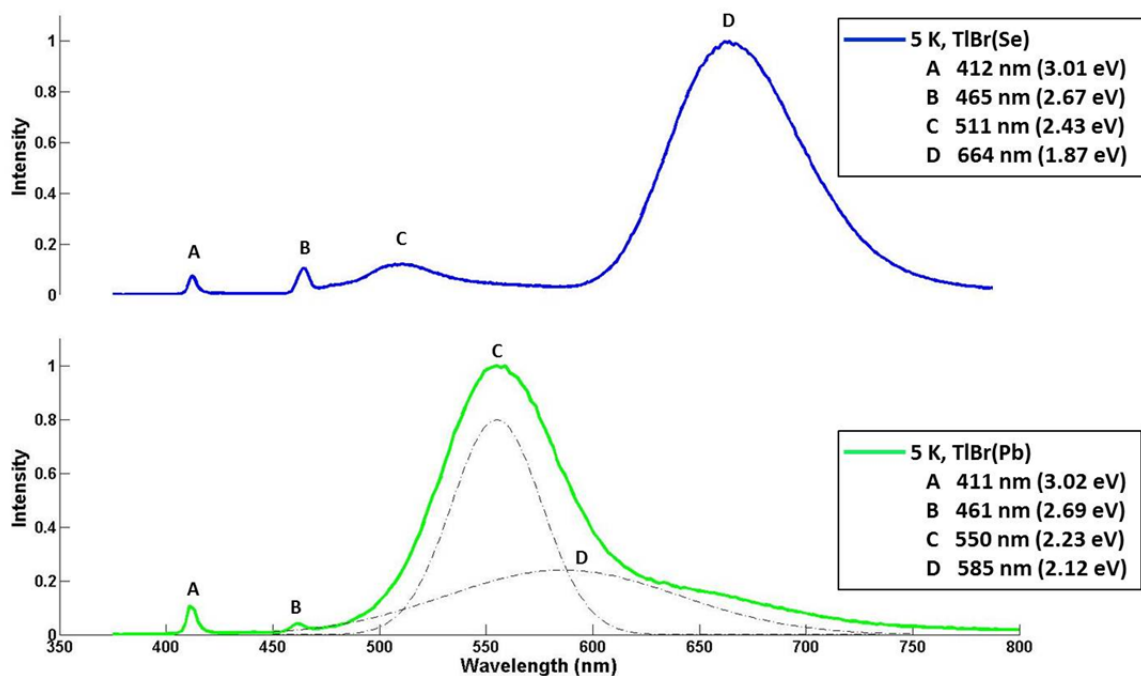


Figure 40. CL spectra at 5 K for (a) Se doped TlBr and (b) Pb doped TlBr.

E. DEEP LEVELS IN THALLIUM BROMIDE

The CL spectra for Se and Pb doped TlBr both show mid-gap defect peaks. The CL spectroscopy can be used in conjunction with other spectroscopic techniques to identify the dopant-related deep level impurity traps that cause these peaks and to begin to piece together a defect level diagram for TlBr similar to the one shown in Figure 36 for Ge. Theoretical work using Density Functional Theory (DFT) has been done to identify deep level impurity sites in the bandgap of TlBr [46]. To the author's knowledge, however, there are currently no published band diagrams based on experimental work that show the location of dopant-related deep levels in TlBr.

One technique for studying deep levels in semi-insulating semiconductors is photo-induced conductivity transient spectroscopy (PICTS). PICTS provides information on the trap activation energy, the trap capture cross section, and the trap type (electron or hole). Together, PICTS and CL can be used to identify the location of deep levels in a semiconductor [62]. Our collaborators at the University of California, Berkeley, have performed PICTS on our samples of Se and Pb doped TlBr. By combining PICTS results

with the CL spectroscopy, the first band picture of dopant-related deep levels for Se and Pb has been created [61]. The results are briefly summarized here.

In the PICTS experimental set up at Berkeley, a high-brightness LED peaked at 450 nm (2.76 eV) is used as a photoexcitation source. A bias between 15–50 V is applied to the sample, and the light is pulsed on for 350 ms and off for 150 ms. The transient photoresponse is measured as a function of temperature over the range of 80–250 K in 0.5 K increments. PICTS spectra are generated, as shown in Figure 41(a). Peaks in the spectra denote detected traps. The traps are plotted on an Arrhenius plot, as shown in Figure 41(b). The slope of the line on the Arrhenius plots gives the trap activation energy, and the y-intercept provides the trap capture cross section. For Se doped TlBr, two traps (A and B) were identified. For Pb doped TlBr, three traps (C, D, and E) were identified.

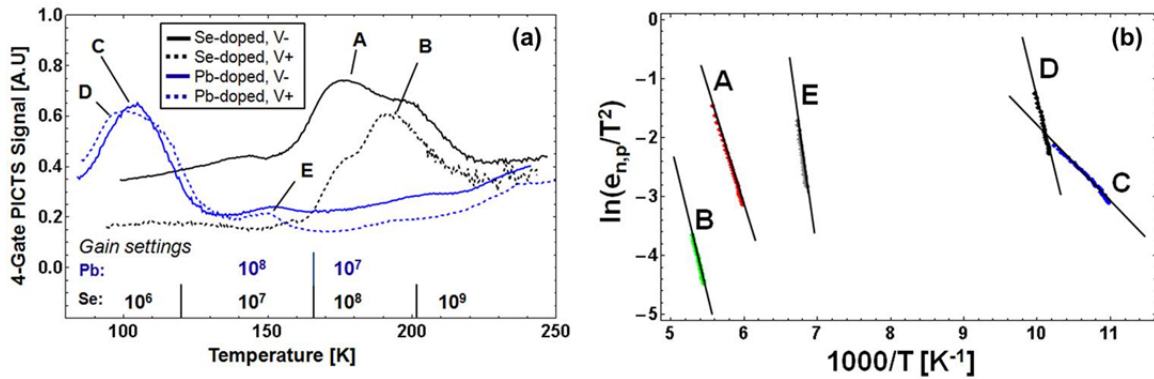


Figure 41. (a) PICTS spectrum and (b) Arrhenius plot. After [61].

For Se and Pb doped TlBr, the measured activation energy, capture cross section, and trap type are summarized in Table 4.

Table 4. Activation energies, cross section, and trap type for identified deep levels. After [61]

Peak	Sample Dopant	$E_{\text{activation}}$ [eV]	Capture Cross Section [cm ²]	Tentative Trap Type
A	Se	0.35	1.9×10^{-12}	electron
B	Se	0.45	6.6×10^{-12}	hole
C	Pb	0.11	1.1×10^{-16}	electron
D	Pb	0.45	3.9*	hole
E	Pb	0.75	2.4×10^3 *	hole

* Denotes unphysically large capture cross sections.

From the CL spectra, an energy offset, ΔE_{ind} , is measured between the defect peak and the indirect band edge at 2.68 eV. Transitions between the levels identified in the PICTS analysis are then matched to ΔE_{ind} to create the band picture. Table 5 shows the dopant, CL peak, ΔE_{ind} , and matching transitions from PICTS. For the Se doped TlBr sample, the CL peak at 2.43 eV does not match a transition identified with PICTS. The CL peak at 1.86 eV, however, matches an intradefect transition between the electron trap at 0.35 eV below the conduction band edge (denoted $E_c - 0.35$ eV) and the hole trap at 0.45 eV above the valence band edge (denoted $E_v + 0.45$ eV). For the Pb doped TlBr sample, the CL peak at 2.23 eV matches a transition from the conduction band edge to the hole trap at $E_v + 0.45$ eV. The CL peak at 2.12 eV matches an intradefect transition from the electron trap at $E_c - 0.11$ eV to the hole trap at $E_v + 0.45$ eV. The PICTS level at $E_v + 0.75$ does not match a CL peak.

Table 5. Comparison of CL and PICTS data. After [61]

Dopant	CL Peak [eV]	ΔE_{ind}	PICTS [eV]
Se	2.43	0.25	-
Se	1.86	0.82	0.35 (A) + 0.45 (B)
Pb	2.23	0.45	0.45 (D)
Pb	2.12	0.56	0.45 (D) + 0.11(C)
Pb	-	-	0.75 (E)

Together, the CL and PICTS data result in the first empirical energy diagram showing deep level impurity states related to Pb and Se dopants in TlBr. The diagram is shown in Figure 42.

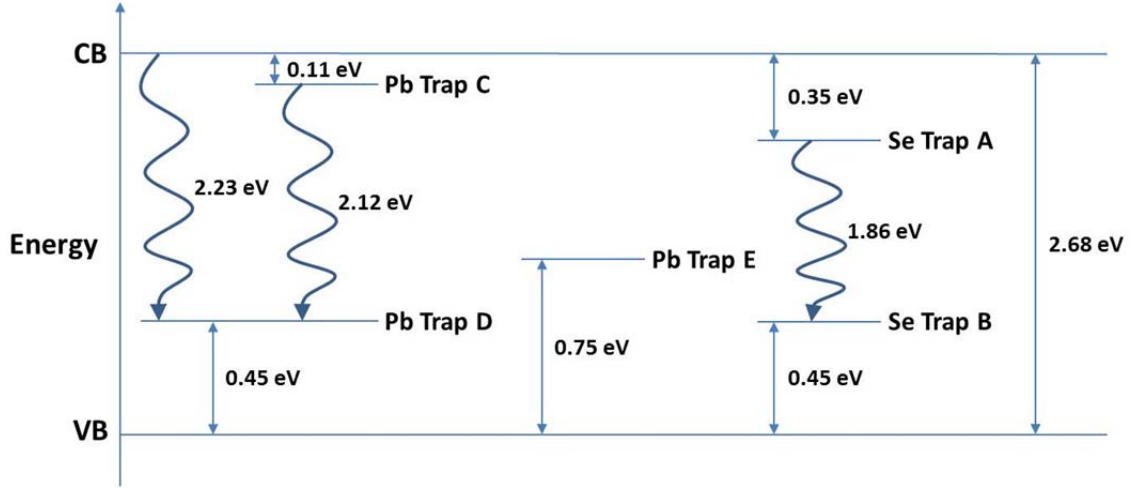


Figure 42. Energy diagram showing mid-gap defect states related to Pb and Se dopants in TlBr. Diagram not to scale. After [61]

F. TRANSPORT IMAGING

Transport imaging was performed on the Se and Pb doped TlBr samples to determine the effect of doping on the ambipolar diffusion length. Three random locations on each sample were chosen. Figure 43 shows the intensity distributions for each location on each sample at 295 K and 5 K. For each sample, at each temperature, there is little variation in the intensity distributions across the different locations. This indicates good material uniformity. Also, the distributions broaden at low temperatures, indicating increased carrier mobilities and lifetimes at lower temperatures.

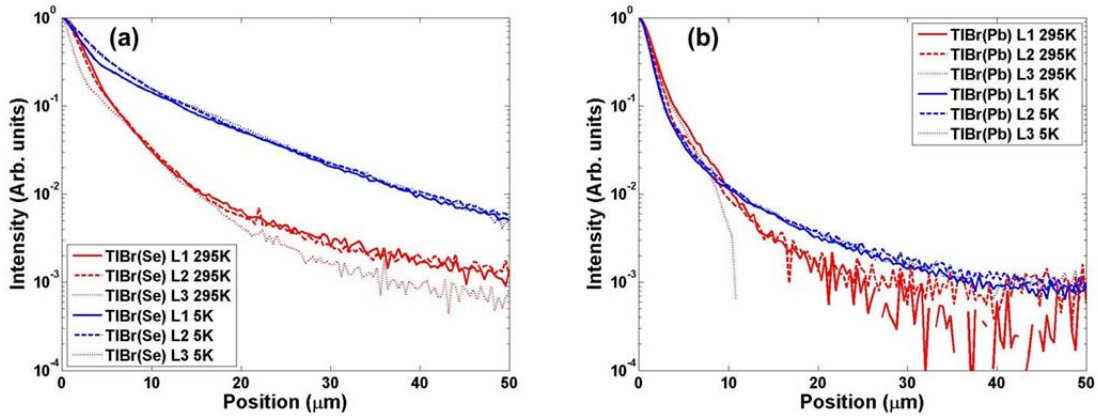


Figure 43. Intensity distributions for three random locations at 295 K and 5 K for (a) Se doped TlBr and (b) Pb doped TlBr.

A comparison of the intensity distributions for each sample at 5 K is shown in Figure 44. The intensity distributions are significantly broader for the Se doped sample. This broadening is consistent with the GDMS data shown in Figure 38, which indicates that the Se doped TlBr contains fewer impurities than the Pb doped sample. However, since each sample still has high impurity levels, Pb alone may not be entirely responsible for the decreased intensity distributions observed in Figure 44. Lead may have the dominant effect, but other impurities are also likely to affect the transport properties. Further investigation with samples with a range of dopant types and concentrations would help to determine the cause of the diffusion length decrease in the Pb doped TlBr sample.

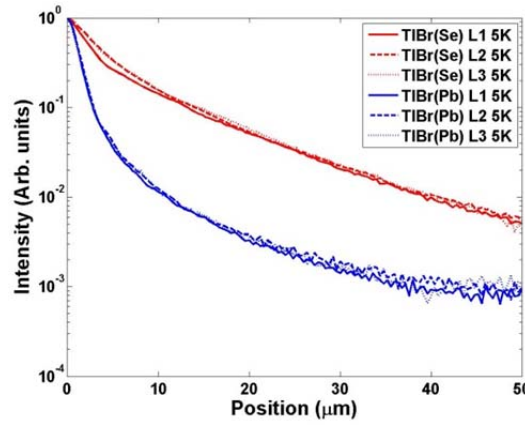


Figure 44. Intensity distributions for three random locations at 5 K for Se doped TlBr and Pb doped TlBr.

The mathematical fits differ for the Se and Pb doped samples. The fits are shown for each sample in Figure 45. For each sample, the lower panel is shown on a logarithmic scale and highlights the differences between the fits. The fit for the Se doped TlBr sample follows the data for the full data range, out to 50 μm . The fit for the Pb doped TlBr sample, however, shows systematic deviation from the data beginning at approximately 15 μm . Further studies using a range of Pb doped samples may help to understand this deviation.

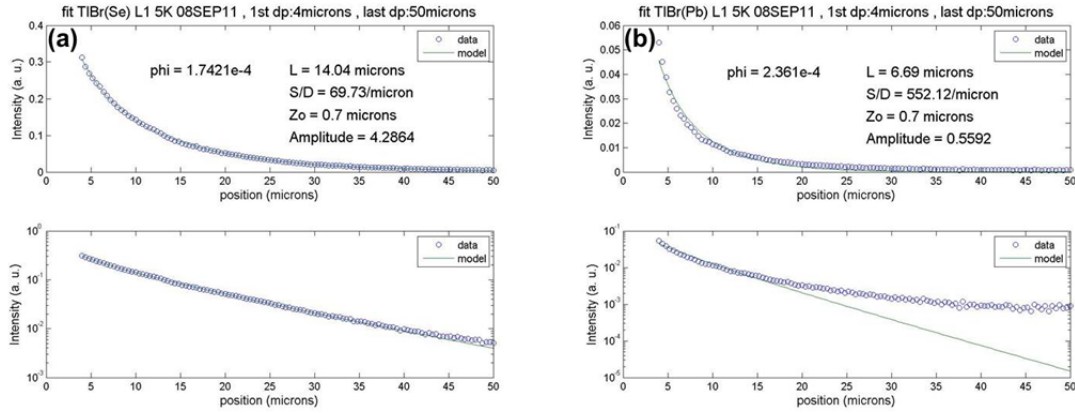


Figure 45. Least squares fitting to the data at 5 K for (a) Se doped TlBr and (b) Pb doped TlBr.

The diffusion lengths from least squares fitting to the model and the calculated $\mu\tau$ products for each sample at each location at 5 K are shown in Table 6.

Table 6. Diffusion length and $\mu\tau$ product at random locations on doped TlBr crystals at 5 K.

TlBr Crystal	Location	Diffusion Length, L_d (μm)	$L_d \pm 1\sigma$ (μm)	$\mu\tau$ Product (cm^2/V)	$\mu\tau \pm 1\sigma$ (cm^2/V)
Se doped	1	14		4.6×10^{-3}	
	2	12	13 ± 1	3.2×10^{-3}	$(3.8 \pm 0.7) \times 10^{-3}$
	3	13		3.7×10^{-3}	
Pb doped	1	6.7		1.0×10^{-3}	
	2	6.2	6.5 ± 0.3	8.9×10^{-4}	$(8.9 \pm 0.6) \times 10^{-4}$
	3	6.7		1.0×10^{-3}	

Figure 46 shows the spatial variation in the diffusion lengths along 16 μm sections of the Se and Pb doped TlBr, averaged over 2 μm sections of the line scan images at 5 K. The materials are the most uniform of any of the TlBr materials investigated to date in terms of their diffusion length and $\mu\tau$ product. Transport imaging is again able to provide a rapid assessment of both the magnitude of the transport properties and the material uniformity in these bulk samples

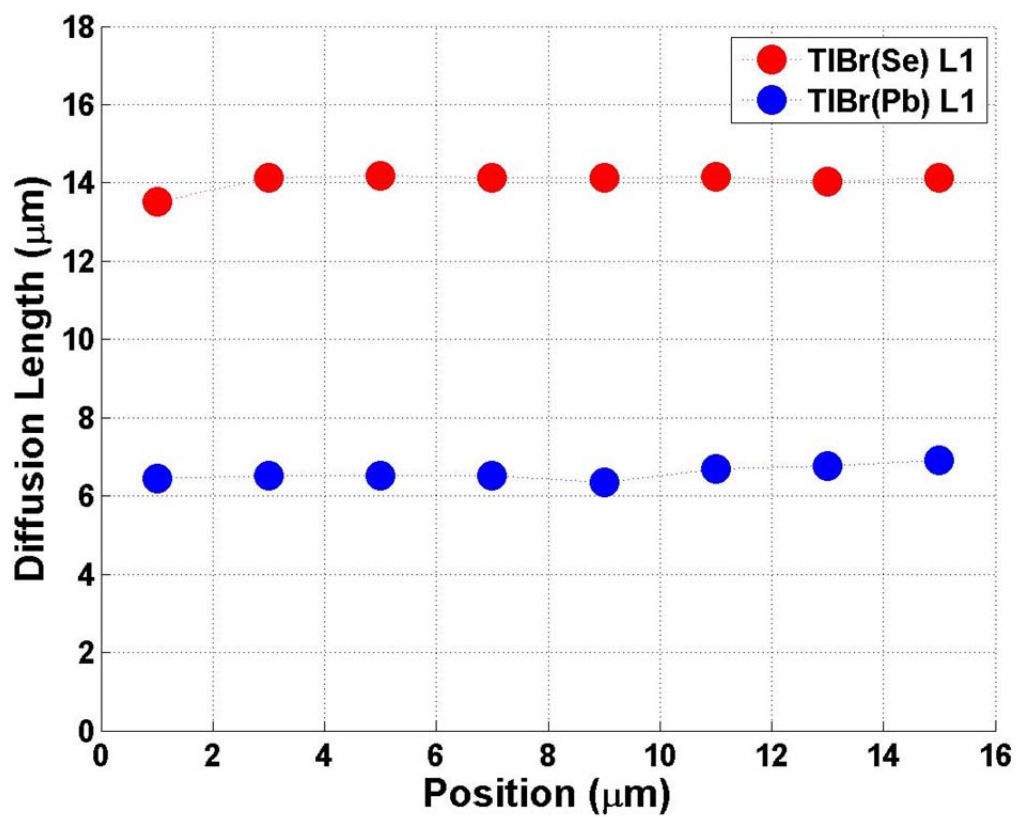


Figure 46. Spatial variation in the diffusion lengths along 16 μm sections of the Se and Pb doped TlBr, averaged over 2 μm sections of the line scan images, at 5 K.

VII. INITIAL INVESTIGATION IN BULK CADMIUM ZINC TELLURIDE

A. OVERVIEW OF CADMIUM ZINC TELLURIDE

Cadmium zinc telluride (CZT) is one of the most promising compound semiconductors under development as a room temperature replacement for HPGe for nuclear radiation detection [24], [56], [63] – [65]. Like TlBr, CZT has a high atomic number ($Z_{\text{Cd}} = 48$, $Z_{\text{Zn}} = 30$, $Z_{\text{Te}} = 52$) and high density (5.78 g/cm^3), resulting in high x-ray and gamma photon attenuation. The wide bandgap of CZT (1.57 eV) leads to high resistivity ($\sim 10^{10} \Omega\cdot\text{cm}$), which allows for room temperature operation without excessive thermal generation of carriers and dark current [66], [67]. Unlike TlBr, CZT exhibits no room temperature polarization effects, which allows for long-term operation without crystal degradation [24], [56]. In terms of spectroscopy, energy resolution $< 1\%$ FWHM has been achieved with CZT for ^{137}Cs (662 keV) [64]. Table 7 summarizes select properties of CZT.

Table 7. Properties of CZT. After [21]

Property	Value
Atomic Number	$Z_{\text{Cd}}: 48, Z_{\text{Zn}}: 30, Z_{\text{Te}}: 52$
Density	5.78 g/cm^3
Bandgap	1.57 eV
Resistivity	$3 \times 10^{10} \Omega\cdot\text{cm}$
Electron Mobility	$1000 \text{ cm}^2/\text{V}\cdot\text{s}$
Hole Mobility	$120 \text{ cm}^2/\text{V}\cdot\text{s}$
Electron $\mu\tau$ Product	$4 \times 10^{-3} \text{ cm}^2/\text{V}$
Hole $\mu\tau$ Product	$1.2 \times 10^{-6} \text{ cm}^2/\text{V}$
Melting Point	1092-1295 °C
Crystal Structure	Cubic (Zinc Blende)

Despite its many positive attributes, several obstacles have limited the widespread use of CZT [68]. Large volume, inexpensive, high quality crystals have been difficult to grow [24]. CZT suffers from incomplete charge collection, particularly for holes, which results in spectral broadening [56], [69]. To overcome this deficiency, CZT detectors are often operated as “electron-only” devices that only collect electrons [69]. Electron charge collection, however, is still hampered by the presence of Te inclusions. Te inclusions are non-stoichiometric defects that form during the melt growth of the crystal, with a typical size of 1–2 μm . Their presence and non-uniform distribution in CZT degrades energy resolution [68].

B. CATHODOLUMINESCENCE

CL mapping and spectroscopy was performed on CZT samples provided by Redlen Technologies in order to determine the CL signature. Two samples, CZT(ST1) and CZT(372), were investigated. The difference between the two samples is that CZT(ST1) has been annealed, but CZT(372) has not.

CL spectroscopy was performed at 295 K and 5 K. For CL spectroscopy, the SEM operating parameters were 20.0 keV, 3×10^{-10} A, and 2000 \times magnification. The slits were set to 0.5 mm (295 K) or 0.1 mm (5 K), and the monochromator step size was 1 nm.

The CL spectra for each sample are shown in Figure 47. For the spectra at 295 K, the peak at 1.56 eV is the band edge of CZT. For the spectra at 5 K, the peak at 1.64 is the band edge of CZT. The peak at ~ 1.61 eV is likely the second LO-phonon (21 meV) replica [70]. The peak at ~ 1.47 eV is likely defect luminescence from complex deep level defects involving Cd vacancies and impurities [71].

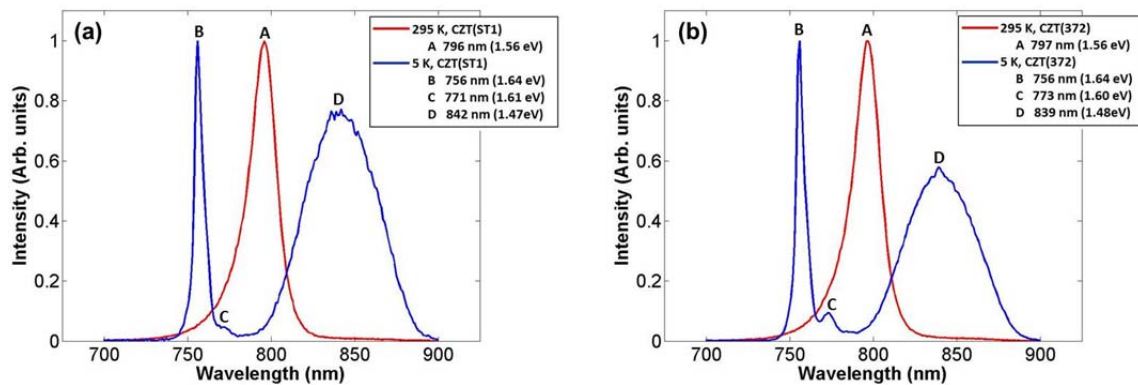


Figure 47. CL spectra at 295 K and 5 K for (a) CZT(ST1) and (b) CZT(372).

A comparison of the CL spectra for each sample at 5 K is shown in Figure 48. The most noticeable feature is a slight decrease in the defect luminescence at ~ 840 nm (1.48 eV) in the unannealed sample, CZT(372).

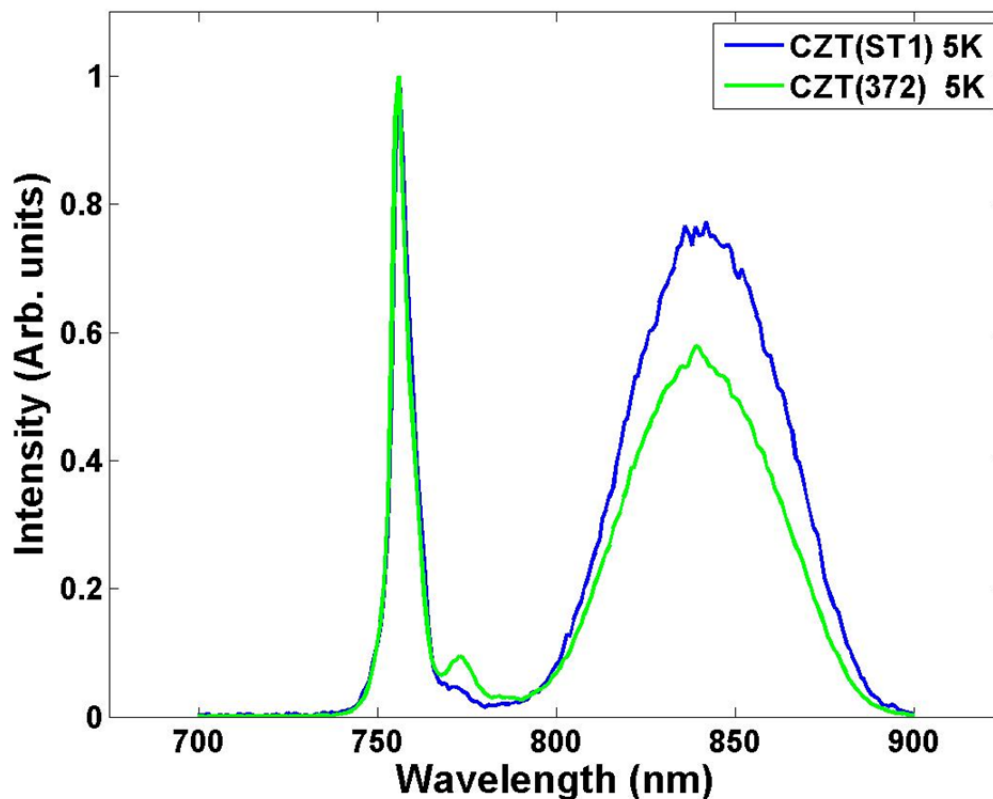


Figure 48. CL spectra at 5 K for (a) CZT(ST1) and (b) CZT(372).

CL mapping was performed on each spectrum at 5K at 755 nm (1.64 eV) to capture the band edge luminescence. The SEM operating parameters were 20.0 keV, 3×10^{-10} A, and 1000 \times magnification, and the slits of the CL system were set to 1 mm. The CL maps are shown in Figure 49. The CL map of CZT(ST1), as shown in Figure 49(a), exhibits areas of decreased intensity in approximately triangular shaped regions, with sizes of 1–5 μ m. The shape and size of these regions are consistent with the reported shape and size of Te inclusions in CZT [50]. The CL map of CZT(372), as shown in Figure 49(b), exhibits black dots up to ~ 1 μ m each along a diagonal line. These dots may represent Te inclusions that have migrated to a defect, such as a grain boundary, during cooling after the growth of a CZT ingot. Such Te inclusion along a defect are said to “decorate” the defect [48]. Further correlated studies with CL and EDX would be necessary to positively identify these areas of reduced intensity as Te.

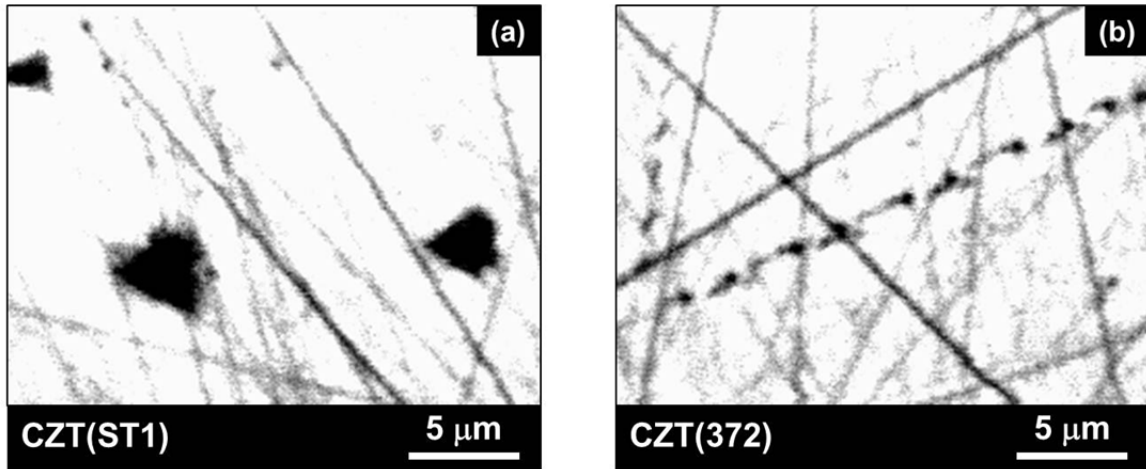


Figure 49. CL mapping at 5 K for (a) CZT(ST1) and (b) CZT(372).

C. TRANSPORT IMAGING

1. Temperature Studies

Transport imaging was performed on CZT(ST1) and CZT(362) at 295 K to investigate their room transport properties. The SEM operating parameters were 10.0 keV, 6×10^{-10} A, and 500 \times magnification. Figure 50 shows the intensity distributions for

each sample. For each sample, two random locations, labeled L1 and L2, were sampled. Each location represents a single field of view from the SEM in picture mode, and these locations on the crystal could be separated from each other by a distance of 0.5 mm or more. At each location, two separate line scan images were recorded, at two closely spaced sub-locations. First, one line scan image was recorded. Then, without moving the sample or changing the field of view, the SEM beam was moved parallel to the first line scan image, and a second line scan image was recorded. Each line scan image is labeled with the pixel sub-location in the field of view. In Figure 50(b), for example, locations L1 and L2 on sample CZT(372) represent two different random locations, separated by 0.5 mm or more. The separation between sub-locations L1 x624 and L1 x250, however, is only $624 - 250 = 374$ pixels. Based on the system resolution of $0.4 \mu\text{m}/\text{pixel}$, these two sampled sub-locations are only separated by $\sim 150 \mu\text{m}$. The line scan images for these two sampled sub-locations are overlaid in the inset in Figure 50(b). Using this scheme, we are able to investigate possible gross and fine changes in transport properties across the crystal. As shown in Figures 50(a) and (b), the intensity distributions for each sample are approximately the same for each location, indicating good material uniformity.

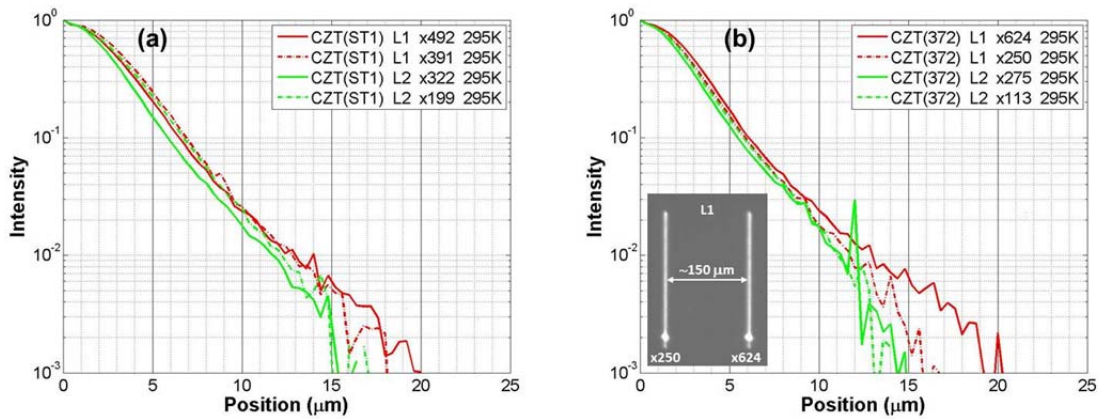


Figure 50. Transport imaging at two locations, L1 and L2, for samples (a) CZT(ST1) and (b) CZT(372). Locations L1 and L2 represent widely separated locations on the crystals, up to 0.5 mm or more. L1 x492 and L1 x391, for example, represent sub-locations that may only be separated by $150 \mu\text{m}$ or less. The inset shows an overlay of the two line scan images at sub-locations L1 x250 and L1 x624.

A comparison of the intensity distributions of the two samples at two random locations, L1 and L2, at 295 K is shown in Figure 51. For CZT(ST1), the distributions for the two sub-locations of L1 (x492 and x391) are nearly identical. For CZT(372), the distributions for the two sub-locations of L2 (x275 and x113) are nearly identical as well. At first glance, when comparing the distributions for CZT(ST1) to the distributions of CZT(372), it may appear that the distributions for CZT(ST1) are more broad. Over the region of approximately 4–12 μm , however, the slopes of the lines are nearly identical. This indicates that the diffusion lengths are approximately equal in these materials.

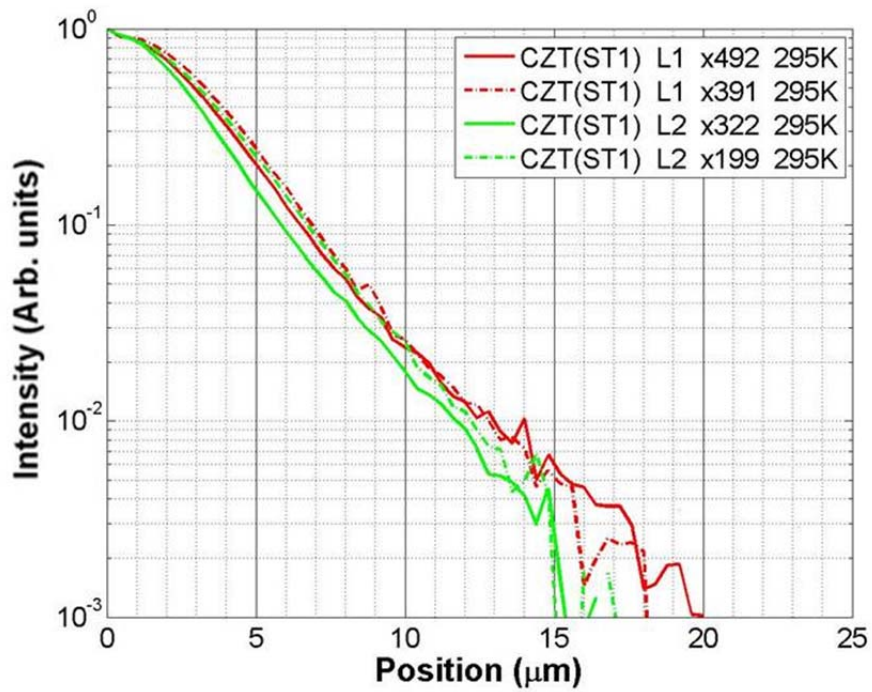


Figure 51. Comparison of intensity distribution at two different locations at 295 K for CZT(ST1) and CZT(372).

Transport imaging was repeated on samples CZT(ST1) and CZT(372) at 5 K in order to detect any low temperature differences in diffusion lengths between the two materials. Figure 52 shows the intensity distributions at 5 K at two closely spaced sub-locations on CZT(ST1) and two different locations on CZT(372). Similar to the results at 295 K, the slopes of the distributions are nearly identical beginning $\sim 4 \mu\text{m}$ from the source, after an initial difference in the shoulder regions of the curves.

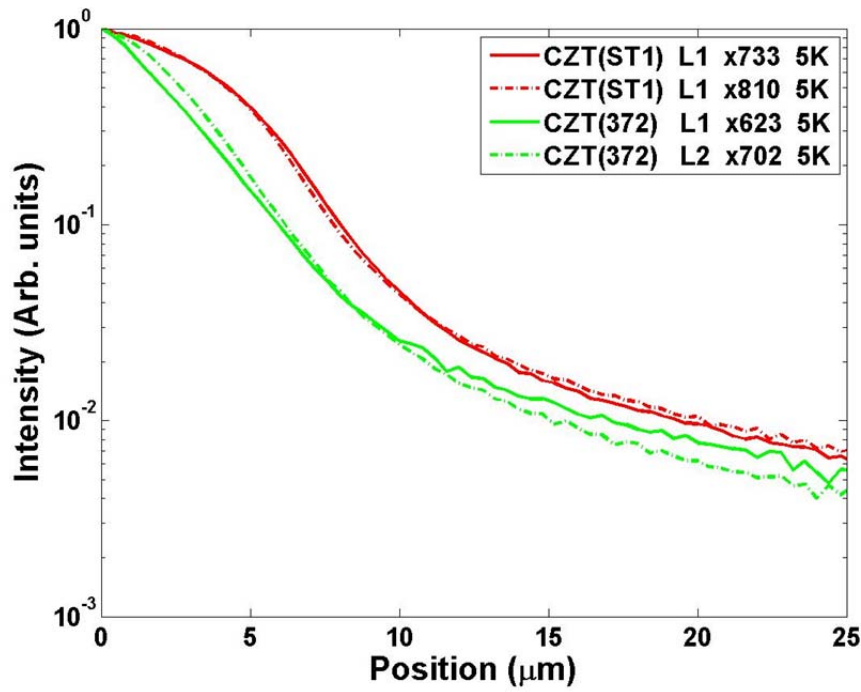


Figure 52. Comparison of intensity distribution at 5 K for CZT(ST1) and CZT(372).

For least squares fitting to the model for CZT(ST1) and CZT(372) at 295 K and 5 K, data were used beginning at 4 μm from the source. The last data point used was varied between 16 μm , 22 μm , and 50 μm . Table 8 shows the calculated diffusion lengths at each temperature, for each sample, for each location, for each stopping point. The reported “endpoint average” diffusion length is an average value over all stopping points for each location. The reported “sample average” is an average value over all stopping points over all locations for each sample. The reported $\mu\tau$ product is based on this sample average.

Table 8. Ambipolar diffusion length and $\mu\tau$ product for CZT(ST1) and CZT(372) at 295 K and 5 K.

Diffusion Length, L_d (μm)									
Data Used for Fitting									
Temp.	Sample	Location	4 – 12 μm	4 – 15 μm	4 – 22 μm	4 – 50 μm	Endpoint Average, $L_{d,End}$	Sample Average, $L_{d,Sample} \pm 1\sigma$	$\mu\tau$ Product (cm^2/V)
295 K	CZT(ST1)	L1 x492	2.67	2.69	2.69	2.69	2.69	2.68 ± 0.01	2.83×10^{-6}
		L1 x391	2.66	2.67	2.67	2.67	2.67		
	CZT(372)	L2 x275	2.78	2.77	2.76	2.75	2.77	2.72 ± 0.05	2.91×10^{-6}
		L2 x113	2.70	2.68	2.66	2.66	2.68		
5 K	CZT(ST1)	L1 x733	3.08	3.11	3.14	3.14	3.12	3.05 ± 0.08	2.16×10^{-4}
		L1 x810	2.94	2.97	2.99	2.99	2.97		
	CZT(372)	L1 x623	3.14	3.29	3.36	3.37	3.29	3.02 ± 0.30	2.11×10^{-4}
		L2 x702	2.68	2.74	2.77	2.77	2.74		

There are three conclusions to draw from the table. First, the stopping point used has little impact on the fit for the diffusion length. At 295 K for CZT(ST1) L1 x492, for example, the diffusion length is 2.67 μm based on data from 4–12 μm , and 2.69 μm based on data from 4–15 μm , 4–22 μm , and 4–50 μm . For all fitting in this dissertation, 50 μm has therefore been used as the stopping point. Second, the two samples do not exhibit significant differences in diffusion length at a specific temperature, such as 295 K. At 295 K for CST(ST1) and CZT(372), for example, the sample average diffusion lengths are $2.68 \pm 0.01 \mu\text{m}$ and $2.72 \pm 0.05 \mu\text{m}$, with only a slight difference between them. Third, the samples may exhibit detectable differences between temperatures. At 295 K for CZT(372) L2 x275, for example, the endpoint average diffusion length is 2.77 μm . At 5 K for CZT(372) L1 x623, however, the endpoint average diffusion length is 3.29 μm . Therefore, it may be possible to track changes of diffusion length with temperature.

Table 8 showed that the end point used for data fitting has little impact on the calculated diffusion length. The start point, however, has a significant impact on the fit. Figure 53 shows fits for CZT(ST1) L1 x733 at 5 K for the data range 2–12 μm and 4–12 μm . For 2–12 μm , the diffusion length is 4.71 μm , but for 4–12 μm , the diffusion length is 3.08 μm . As shown in Figure 53(a), the model cannot properly fit the shoulder region of the curve exhibited in this sample below $\sim 4 \mu\text{m}$. Further investigation is required to better understand this region right near the source.

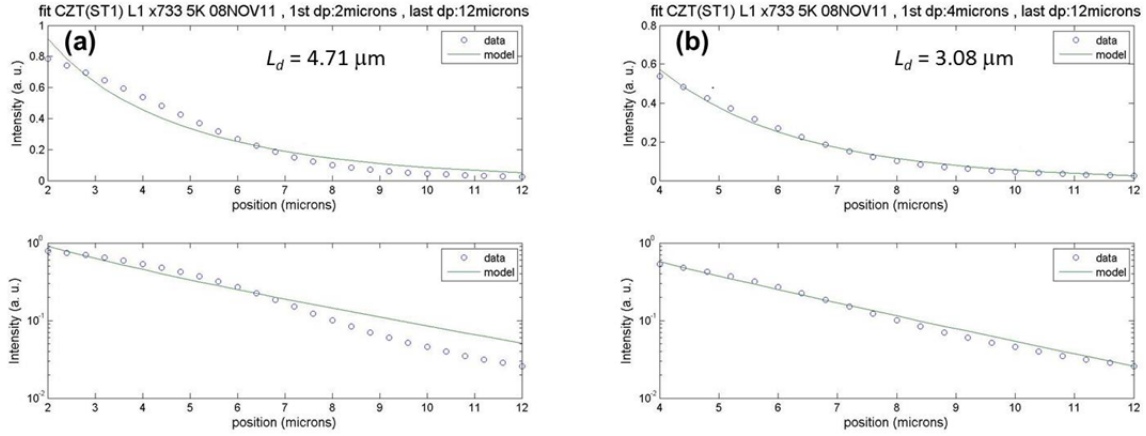


Figure 53. Mathematical fits for diffusion length at 5 K for CZT(ST1) L1 x733 for data from (a) 2–12 μm and (b) 4–12 μm .

Table 8 showed that it may be possible to detect changes in diffusion length as a function of temperature. A temperature study was conducted on CZT(372) to investigate how diffusion length and $\mu\tau$ product varied over the range of 5 K to 60 K. Figure 54 shows the normalized mean distributions for the temperature range. The SEM operating parameters were 10.0 keV, 6×10^{-10} A, and 1000 \times magnification.

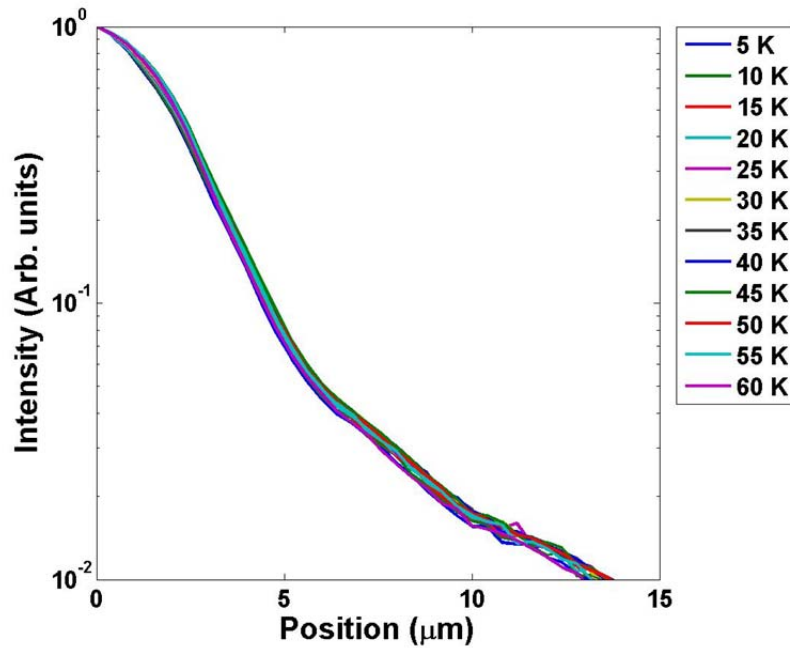


Figure 54. Normalized mean intensity distributions for CZT(372) for temperatures between 5 K and 60 K.

Figure 55 shows plots of temperature vs. diffusion length and temperature vs. $\mu\tau$ product obtained by fitting the data in Figure 54 to the model. The $\mu\tau$ product decreases monotonically with increasing temperature over the range of 5–60 K.

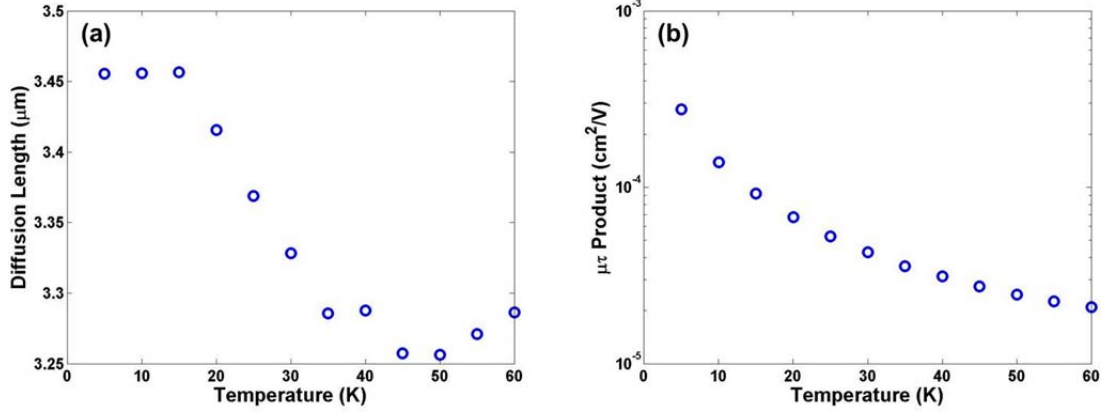


Figure 55. Temperature dependence of (a) diffusion length and (b) $\mu\tau$ product for CZT(372).

2. Effects of Inclusions

Detector-grade CZT is typically grown in Te-rich melts, which results in ingots with high concentrations of Te precipitates and Te inclusions. Te precipitates form during the cooling process, and their typical diameter is 10–50 nm. In contrast, Te inclusions are non-stoichiometric defects that form during the crystal melt growth as a result of the capture of Te-rich melt droplets at the growth interface. Their typical size is 1–2 μm, with sizes up to 100 μm reported, and they have a characteristic triangular shape. A dense dislocation field typically surrounds a Te inclusion. Te inclusions can also migrate during the cooling of the CZT ingot. When they encounter a structural defect, such as a grain boundary, their movement through the crystal stops, and the Te inclusions decorate the defect. Te inclusions and their associated dislocation field can degrade charge transport by trapping charge and distorting the internal electric field of the crystal. Non-uniform distribution of Te inclusions can result in spatial variation of charge transport and degraded energy resolution [50], [68]. Not all inclusions, however, affect charge transport. Te inclusions with diameters < 3 μm have been shown to have no effect on charge transport, up to concentrations of $3 \times 10^6 \text{ cm}^{-3}$ [68].

Amman (2002) has proposed a model to explain the non-uniformity in electron transport observed in CZT crystals [26]. His model is shown schematically in Figure 56. In this model, one alpha particle (α_1) passes through a region free of Te inclusions and creates charges that are trapped uniformly through the crystal. A second alpha particle (α_2) passes through a region with a high concentration of inclusion and experiences non-uniform charge trapping. The two events will register different pulse heights in the detector, resulting in spectral broadening and degraded detector resolution.

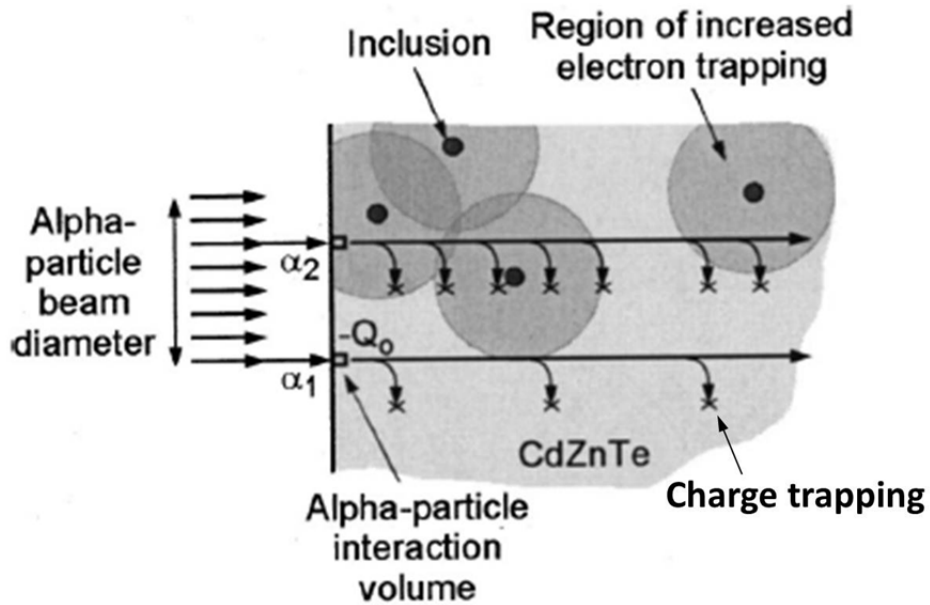


Figure 56. Proposed explanation for non-uniform charge trapping due to Te inclusions. After [26].

An initial transport imaging experiment has been performed to illustrate a potential approach to investigating the effects of Te inclusion on charge transport. Figure 57(a) shows an optical image of CZT(ST1) from the SEM in picture excitation mode at 5 K. Four dark spots are visible, each $\sim 1 \mu\text{m}$ in width, and two of them, labeled x733 and x810, exhibit clear triangular shapes. Based on their sizes and shapes, these dark triangular spots are presumably Te inclusions. Figure 57(b) shows the normalized luminescence intensity from the same region of the crystal. The luminescence from the Te inclusions is very low.

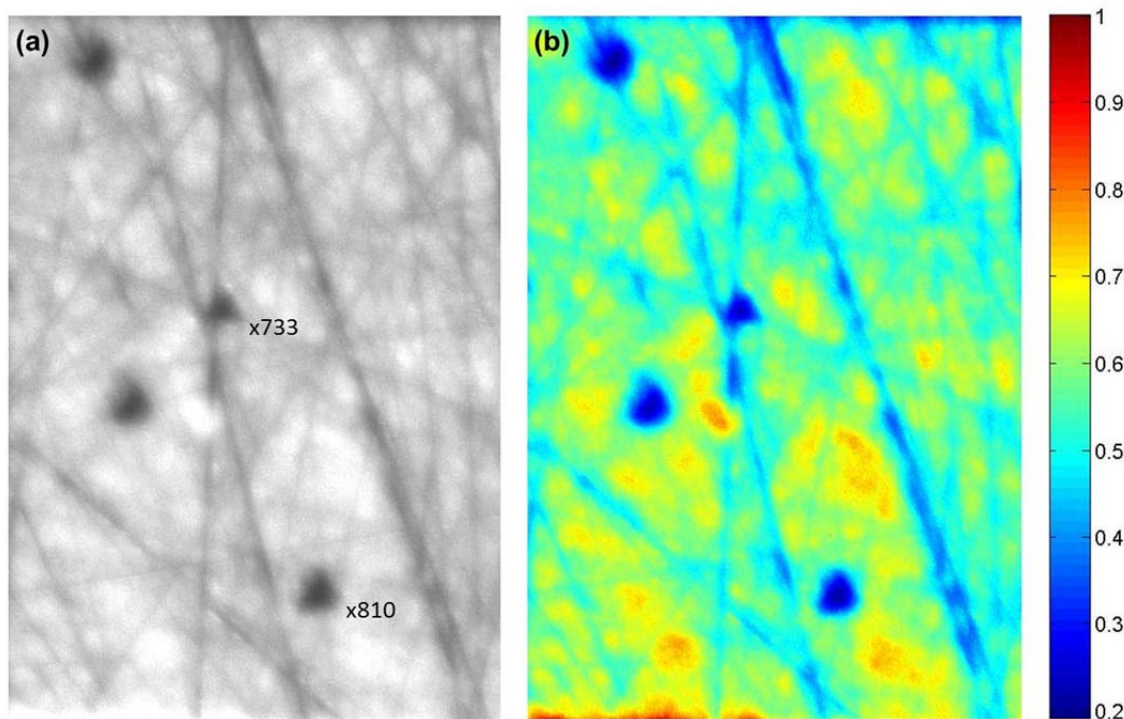


Figure 57. (a) Luminescence from CZT(ST1) from SEM operated in picture excitation mode. (b) Luminescence intensity from same region of CZT(ST1) crystal.

Figure 58(a) shows a slightly extended area of the same region of the CZT(ST1) crystal. The red line indicates where the SEM line mode excitation will cross right over the Te inclusion labeled x733. An optical image of the line scan is shown in Figure 58(b). The line scan data are analyzed over two regions. Region B-B' includes 160 μm of data. Region A-A' primarily includes the Te inclusion. The intensity distribution for each region is shown in Figure 58(c). Surprisingly, the intensity distribution is broader over the inclusion compared to the average distribution over the entire line scan. From the least squares fitting of the data from the two regions, the diffusion length is 3.07 μm over the entire line scan (B-B') but increases to 4.05 μm in the vicinity of the Te inclusion (A-A'). The process was repeated with the Te inclusion labeled x810, with similar results. The diffusion length was 2.99 μm over the entire line scan, and 4.15 μm over just the inclusion.

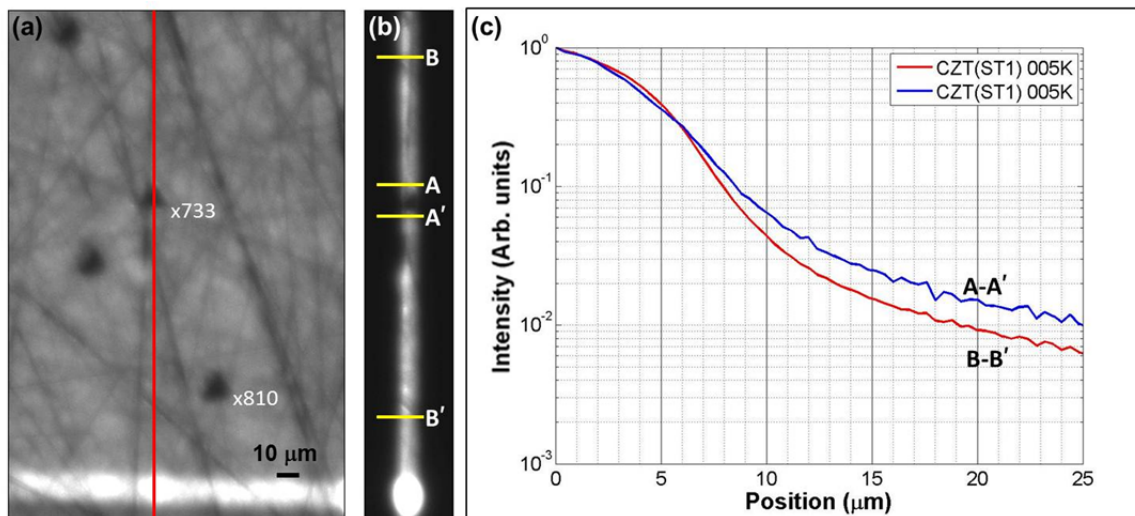


Figure 58. (a) Optical image from SEM picture excitation mode, showing location of line scan in red. (b) Optical image from SEM line excitation mode. The data are extracted over the majority of the line scan (B-B') and over just the Te inclusion (A-A'). (c) Luminescence intensity distributions over the two regions.

Further investigation is necessary to gather more statistics. These results could be within the experimental error, or it could be that the Te inclusion is a sink for local point defects and the diffusion length is in fact locally increased in its vicinity.

Using transport imaging, it may be possible to quantify the region of increased electron trapping associated with a Te inclusion. A series of line scan images could be taken, beginning at one side of the inclusion and continuing to the other side, as shown schematically in Figure 59. Each line scan could be analyzed twice, once over the entire line scan (B-B'), and a second time just over the region in line with the inclusion (A-A'). Far to the left of the inclusion, outside the region of increased electron transport, we would expect the two regions from each line scan to have approximately the same diffusion length. As we approach the region of influence, however, we would expect the diffusion behavior of the two line scan regions to diverge. On the right side of the inclusion, we would similarly expect to approach a point at which the diffusion behavior from the two regions converges again. One could further apply this technique systematically to inclusions of varying sizes to investigate the correlation between inclusion size and its influence on the region of increased electron trapping.

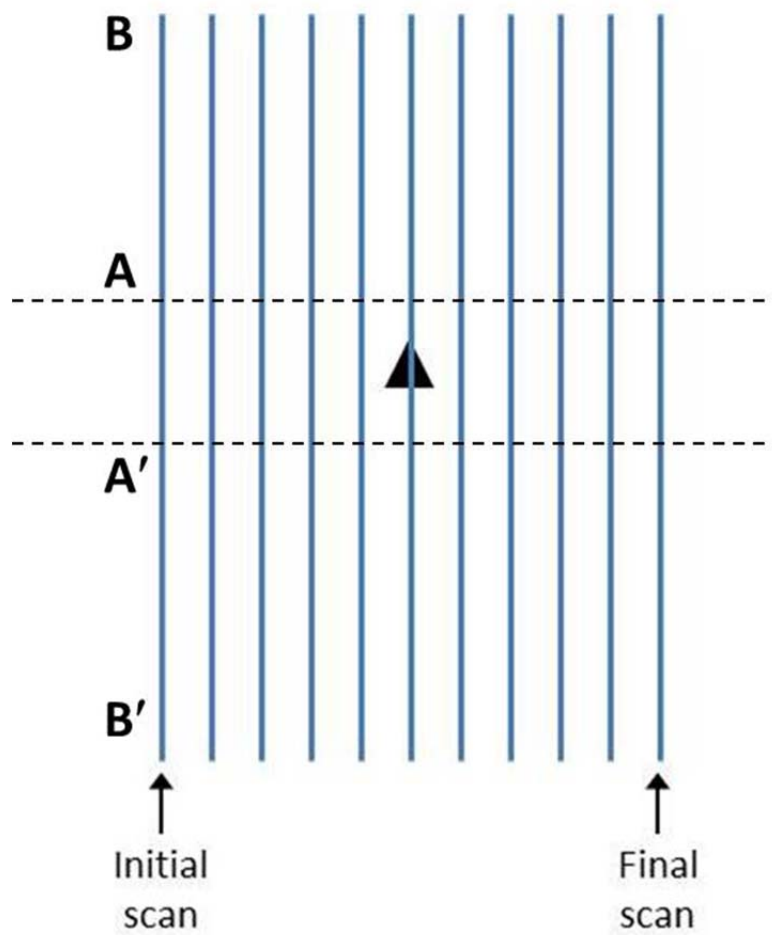


Figure 59. Schematic for investigating region of increased electron trapping associated with Te inclusions.

THIS PAGE INTENTIONALLY LEFT BLANK

VIII. FUTURE WORK

A. OVERVIEW OF FUTURE WORK

In this work, we have applied transport imaging to bulk semiconductors to investigate spatial uniformity in the $\mu\tau$ product. Fitting the data to the mathematical model remains challenging in two regions. Close to the source, at distances less than $\sim 4 \mu\text{m}$, a shoulder region often appears in the data, which the model cannot accommodate. At distances greater than $\sim 15 \mu\text{m}$, when intensity values reach $\leq 1\%$ of the maximum, systematic deviation often occurs between the data and the mathematical model. This is most likely due to statistical fluctuations associated with background levels in the CCD camera. Future work using transport imaging in bulk samples should focus on modifying the model to incorporate the physics at play in these two regions. Three areas of potential research are photon recycling, the generation volume, and a high-injection model.

B. PHOTON RECYCLING

Photon recycling, also known as self-absorption, occurs when a high-energy photon created by the recombination of an EHP is re-absorbed to create another EHP nearby. This new EHP can then recombine and re-emit a photon of lower energy. The net result is the production of lower energy photons of longer wavelength. Photon recycling has been studied extensively for a variety of photovoltaic and optoelectronic devices [72] – [79]. In double heterostructures of GaAs-GaAlAs, for example, photon recycling has been shown to increase the net radiative lifetime of carriers [79]. Of special note, Badescu (1993 and 1997) has developed a model to show how photon recycling influences the spatial distribution of excess minority carriers in n -type or p -type semiconductors under low injection conditions and results in increased efficiency in GaAs solar cells [74], [75].

The effects of photon recycling in bulk semiconductors such as TlBr have not been investigated. Here, we report on preliminary results of photon recycling in CZT and TlBr using transport imaging with optical filters.

In transport imaging, charge transport information is obtained from the luminescence intensity distribution. To accurately model the diffusion behavior of the charge carriers in semi-insulating materials, this luminescence should only come from EHP recombination, not secondary emission due to photon recycling. The potential effect of photon recycling on the intensity distribution is illustrated schematically in Figure 60. In Figure 60(a), no photon recycling is present. EHPs created in the generation volume diffuse, and then recombine, emitting photons of various wavelengths, depending on the luminescence spectrum of the individual material. The intensity distribution reflects the luminescence due to the diffusion of EHPs alone. In Figure 60(b), photon recycling occurs. EHPs created in the generation volume diffuse, and then recombine, emitting photons of different wavelengths. Some of the high energy photons, however, may create secondary photons of lower energy at points removed from the site of the EHP recombination, especially if midgap defects are present in the material. The overall effect is to broaden the intensity distribution. Now, the intensity distribution represents both diffusion and photon recycling.

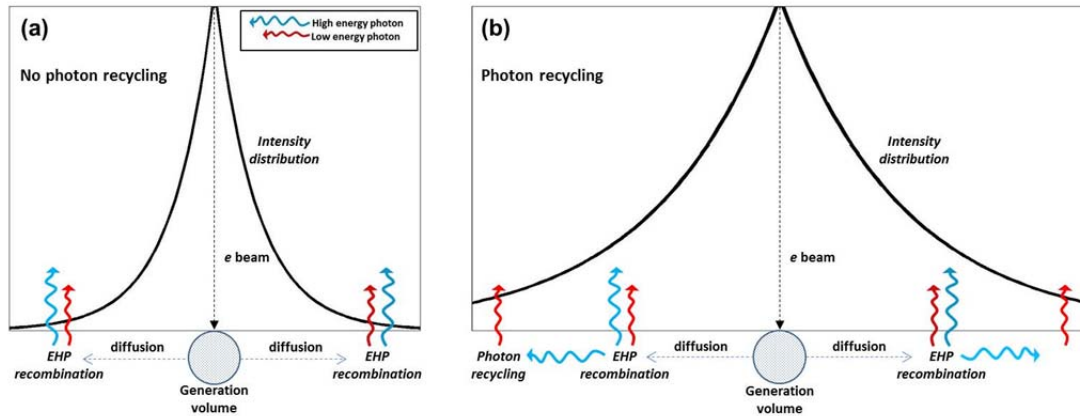


Figure 60. Effects of photon recycling in a semiconductor.

One way to investigate the role of photon recycling is to filter the light before it reaches the CCD array camera. The CL spectra for both CZT(372) and TlBr(Se) were observed to have high energy peaks followed by lower energy broad defect luminescence. Transport imaging was performed in these samples with short and long pass filters to separate the luminescence observed.

If photon recycling is occurring in these samples, we would expect the following results. With the short pass filter, we should primarily detect the shorter wavelength, higher energy photons created by the recombination of EHPs. The intensity distribution should be narrower than the unfiltered distribution since we are not detecting secondary, lower energy photons created by photon recycling at points far removed from the generation volume. With the long pass filter, we should primarily detect the longer wavelength, lower energy photons, created both by the recombination of EHPs and by photon recycling at points far removed from the generation volume. The intensity distribution should actually be broader than the unfiltered spectrum, however, since we are lowering the overall recorded intensity but still capturing light at the same distance as the unfiltered distribution.

Figures 61 shows the CL spectrum at 5 K for CZT(372) and the transmission curves for the optical filters used. The CZT(372) CL spectra at 5 K shows a direct gap peak at 756 nm (1.64 eV) and a broad defect peak at 839 nm (1.48 eV). As shown in Figures 61(a) and (b), a short pass filter at 800 nm was used and a long pass filter at 780 nm was used.

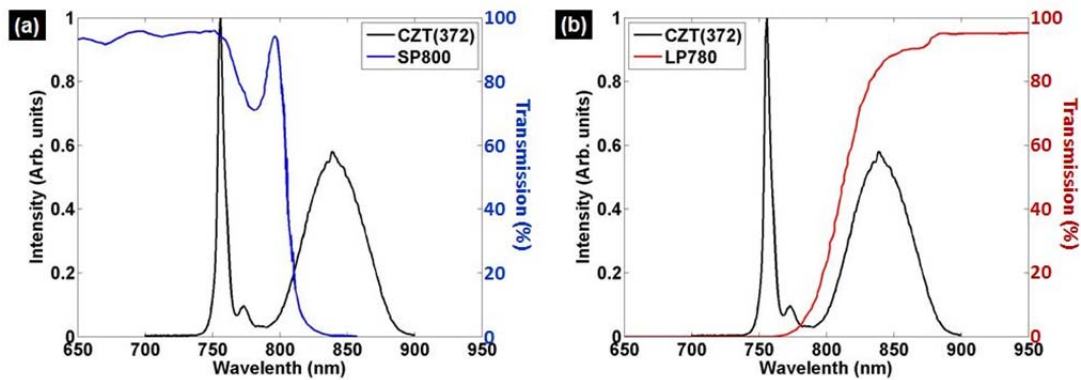


Figure 61. CL spectra at 5 K for CZT(372) and filter transmission spectra for (a) Short pass filters and (b) Long pass filters.

Figure 62 shows the intensity distribution from transport imaging of CZT(372). Figure 62(a) shows the intensity plotted in terms of counts recorded on the CCD array camera, and Figure 62(b) shows the same data plotted with normalized intensity.

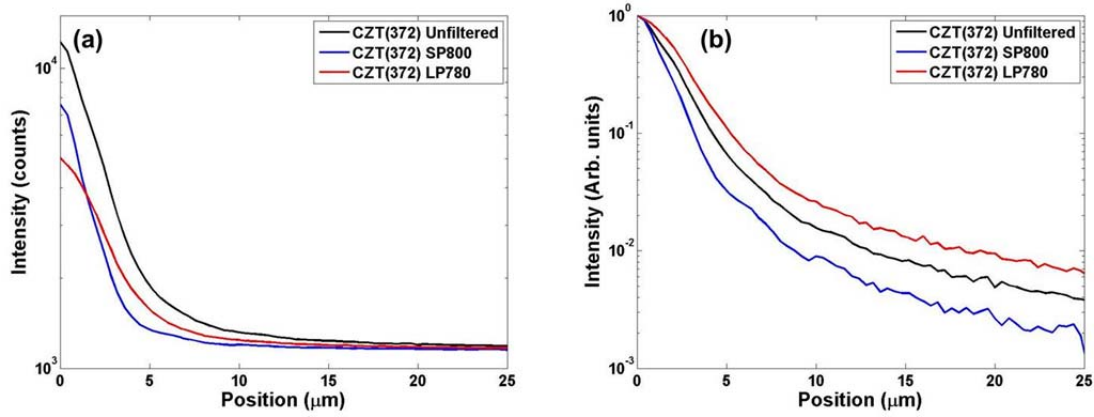


Figure 62. Intensity distributions from transport imaging of CZT(372) at 5 K for unfiltered, short-pass filtered, and long-pass filtered conditions. The same data are shown with the y-axis plotted in (a) Intensity, as measured by counts recorded on the CCD array camera, and (b) Normalized scale, with each distribution normalized to its own maximum.

The intensity distributions shown in Figure 62 for CZT(372) show the trend we would expect if photon recycling is occurring. The distribution with the short pass filter is narrower than the unfiltered distribution due to the removal of secondary, lower energy photons created by photon recycling at points far removed from the generation volume. The distribution with the long pass filter is broader than the unfiltered distribution due to removal of higher energy photons that reduce with intensity while still detecting lower energy photons created through photon recycling at points far removed from the generation volume. Although further investigation is necessary, this result suggests that future transport imaging work in CZT should be conducted with a short pass filter to remove the effects of photon recycling.

Figure 63 shows the CL spectrum at 5 K for TlBr(Se) and the transmission curves for the optical filters used. The TlBr(Se) CL spectra at 5 K shows direct and indirect gap peaks at 412 nm (3.01 eV) and 465 nm (2.67 eV) and a broad defect peak at 664 nm (1.87 eV). As shown in Figure 60(a), two short pass filters at 550 nm and 600 nm were

used. The filters were used in tandem due to the increase in their transmission at longer wavelengths. Since the transmission increases at longer wavelengths, it was not possible to completely filter these longer wavelengths. As shown in Figure 60(b), a long pass filter at 515 nm was used.

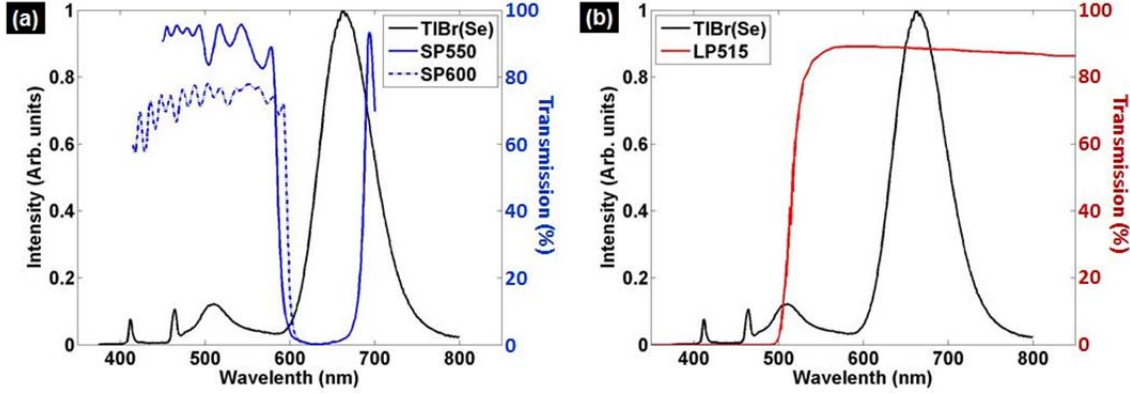


Figure 63. CL spectra at 5 K for TlBr(Se) and filter transmission spectra for (a) Short pass filters and (b) Long pass filters

Figure 64 shows the intensity distribution from transport imaging of TlBr. Out to $\sim 4 \mu\text{m}$, the distributions follow the trend we would expect if photon recycling were present. This is not the case, however, beyond $\sim 4 \mu\text{m}$, where the distribution is broader with the short pass filters. This could be due to incomplete filtering of the longer wavelength photons with the short pass filter, allowing some photon recycling to occur and broadening the distribution. It could also suggest that carrier diffusion is the dominant process and that the short pass distribution simply reflects variations in the recombination ratios. Further investigation with different filters is necessary to understand these results. These initial results do not suggest that traditional photon recycling is dominant in TlBr.

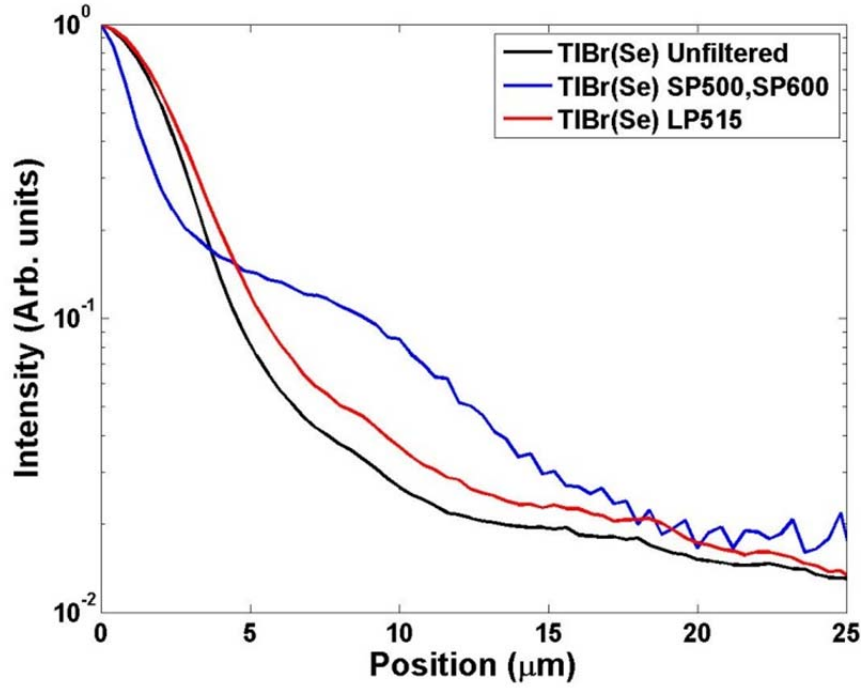


Figure 64. Intensity distributions from transport imaging of TlBr(Se) at 5 K for unfiltered, short-pass filtered, and long-pass filtered conditions.

The 2D diffusion model for charge transport in bulk semiconductors does not include a term to account for photon recycling. Many methods have been investigated for including this term [77] – [79]. One approach [78] is to include a radiative lifetime multiplicative factor, ϕ , whereby the minority carrier lifetime becomes

$$\frac{1}{\tau} = \frac{1}{\tau_{nr}} + \phi \frac{1}{\tau_r}. \quad (35)$$

Another method has been to include photon recycling as another generation term in the continuity equation [79]. If we were to follow this approach, we could modify our continuity equation in Equation (17) to become

$$\frac{\partial}{\partial t} u(\vec{r}, t) = G_{\text{electron beam}} + G_{\text{photon recycling}} - R + \frac{1}{e} (\nabla \cdot \vec{J}) \quad (36)$$

Additional research would be necessary to determine the functional form of the photon recycling generation rate.

C. GENERATION VOLUME

When an electron from an SEM enters a semiconductor, it undergoes a series of elastic and inelastic collisions that deflect it from its path and cause lateral spreading from its initial trajectory. The scattering events create a 3D generation volume of charge carriers below the surface on a μm scale [80]. Under high energy (e.g., 20 keV) electron beam excitation, the average energy required to make a single EHP is only 6.5 eV for TlBr and 4.64 eV for CZT. A single high energy electron can therefore create thousands of EHPs within the generation volume [21], [81]. At normal incidence of the electron beam, the shape of the generation volume depends on the incident beam energy and the atomic composition of the semiconductor. Monte Carlo electron simulations in low-density, low-Z materials show pear-shaped generation volumes, whereas simulations in high-density, high-Z materials reveal more hemispherical-shaped generation volumes [81].

The 2D diffusion model for charge transport in bulk semiconductors models the generation volume as a delta function at a depth z_0 below the surface. When the diffusion lengths are large compared to the generation volume, the effects of the generation volume are minimal, and the delta function approximation is valid. When the diffusion lengths are comparable in size to the generation volume, however, the delta function approximation may fail to accurately model the generation volume.

The net recorded luminescence in transport imaging is a convolution of the intensity distribution due to recombination in the generation volume and the intensity distribution due to charge transport. Luminescence from the generation volume depends on the energy of the incident electrons, whereas luminescence at points removed from the generation volume holds information about the diffusion behavior of the charge carriers. In order to de-convolve these two distributions, the luminescence distribution for the generation volume must be modeled. Two approaches considered here for future work are Monte Carlo simulations and experimentation.

A Monte Carlo simulation code called CASINO, version 2.4.8.1, has been run to investigate the generation volume in bulk TlBr. The code models the trajectories and energy loss of primary electrons until they reach energies of 50 eV. Below 50 eV, the

modeling becomes inaccurate [82]. For the simulations in TlBr, the SEM beam energy is 20 keV, the SEM spot size is 60 nm, and the number of simulated electrons is 100,000. Figure 65(a) shows the trajectory of primary electrons after scattering. Electrons in this simulation penetrate to a maximum depth of ~ 1700 nm. Figure 65(b) shows the distribution of the electrons as a function of their maximum depth. On average, the electrons reach a depth of ~ 700 nm, which was the value used for z_0 in all mathematical fitting for TlBr in this dissertation. Figure 65(c) shows a side view (XZ) of the energy density distribution in depth of the material integrated over the width of the material. Approximately 95% of the energy is deposited within ~ 750 nm of the surface. Figure 65(d) shows a planar view (XY) of the lateral extent of the energy density distribution integrated through the depth of the material. Approximately ninety-five percent of the SEM beam energy is distributed in an area with a diameter of ~ 500 μm .

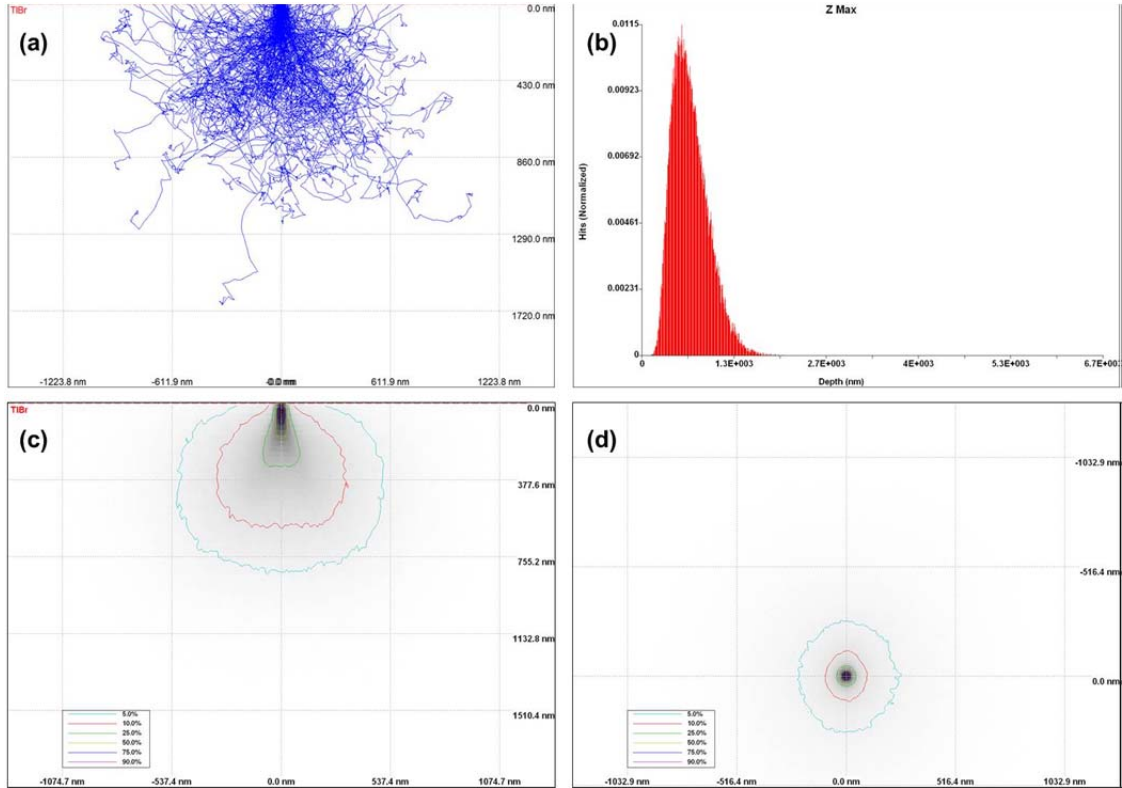


Figure 65. Monte Carlo simulations for 20 keV electrons in TlBr showing (a) Electron trajectories, (b) Electron depth distribution, (c) Integrated energy density distribution in XZ plane, and (d) Integrated energy density distribution in XY plane.

By plotting the energy density distributions shown in Figures 64(c) and (d) as functions of position, one can begin to create a model for the generation volume. Figure 66 shows oblique and side views of the integrated energy density in TlBr. This energy density is the basis for the generation volume.

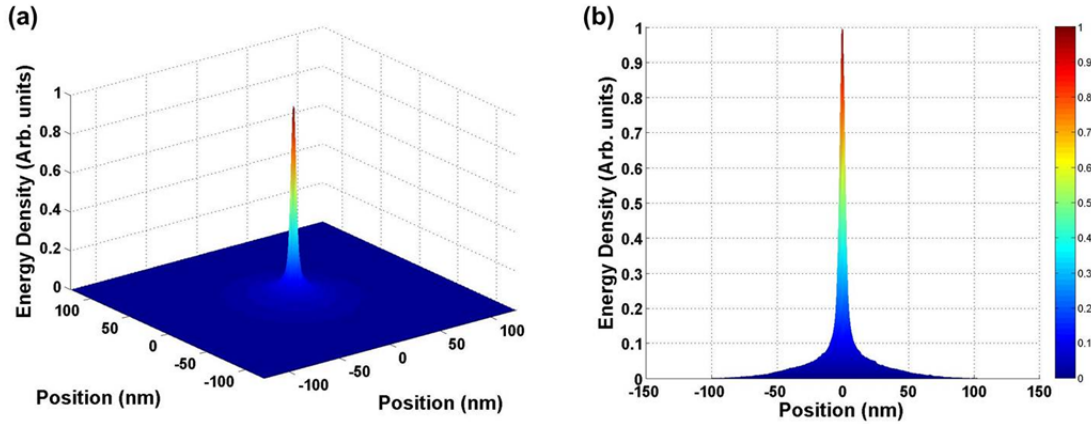


Figure 66. Monte Carlo simulations for 20 keV electrons in TlBr showing (a) Oblique and (b) Side views of the integrated energy density.

In Figure 67, the energy distribution shown in Figure 66 is fit to individual Gaussian and Lorentzian functions. Figure 67 indicates that a sum of Lorentzian or Gaussian functions may provide a good fit for the energy density.

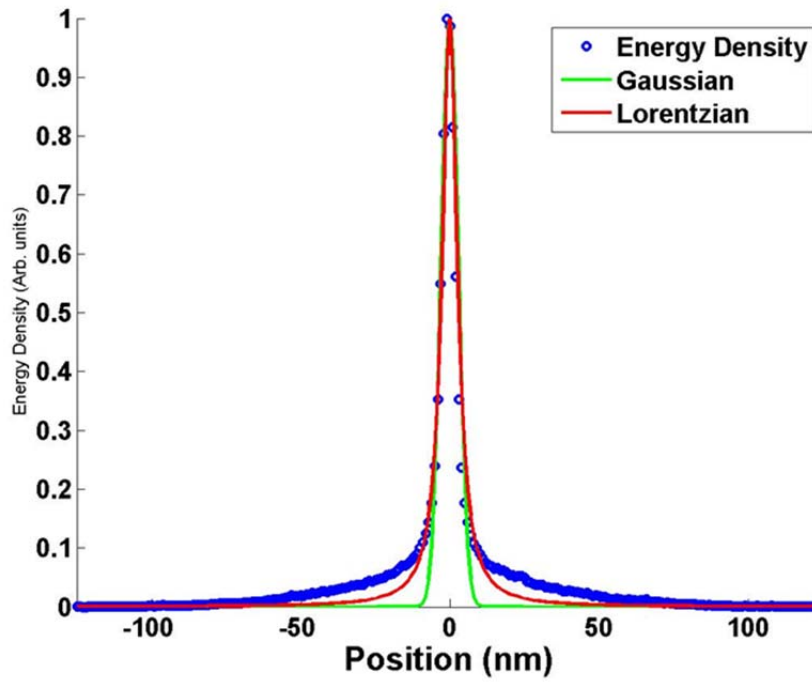


Figure 67. Gaussian and Lorentzian fits to integrated energy distribution from Monte Carlo simulations with 20 keV electrons in TlBr.

Monte Carlo simulations may provide a basis for future exploration into the generation volume. However, there are certain limitations to this approach. First, the Monte Carlo simulations cut off at 50 eV, thereby losing the full energy deposition for each electron. Second, the energy density distributions only reflect energy deposition, not the luminescence emitted from the recombination of electron-hole pairs created by this energy. The luminescence intensity distribution will be larger than the energy distribution. Much work is necessary to further model the luminescence emitted as a result of this energy deposition. Third, the energy density distributions are very narrow, with $\sim 95\%$ energy density deposition in an area with a diameter of ~ 100 nm, as shown in Figure 66(b). This distribution alone seems too narrow to account for our need to begin fitting the data at $4\text{ }\mu\text{m}$ due to the generation volume.

An alternate experimental approach would be to use known transport imaging intensity distributions from high Z materials that just reflect the generation volume, with minimal contribution from carrier transport. Transport imaging results have been

reported on thick samples of highly doped *n*-type GaAs at a probe current of 1×10^{-9} A and beam energies of 5–30 keV, with the SEM beam operated in spot mode of excitation [81]. In that work, the small diffusion length of the material ($< 1 \mu\text{m}$) and the 3D nature of the carrier diffusion allowed for direct imaging of the generation volume. Figure 68(a) shows the results of that work. Figure 68(b) shows Gaussian and Lorentzian fits to the 20 keV distribution. From Figure 68(b), the Lorentzian appears to be a reasonable fit to the generation volume. Interestingly, the generation volume distribution approaches zero at $\sim 4 \mu\text{m}$, the same distance used as a starting point for our mathematical fitting. This empirical distribution could be used for transport imaging in bulk samples to de-convolve the intensity distribution due to recombination in the generation volume and the intensity distribution due to diffusion of charge carriers in order to more accurately model the diffusion behavior of carriers.

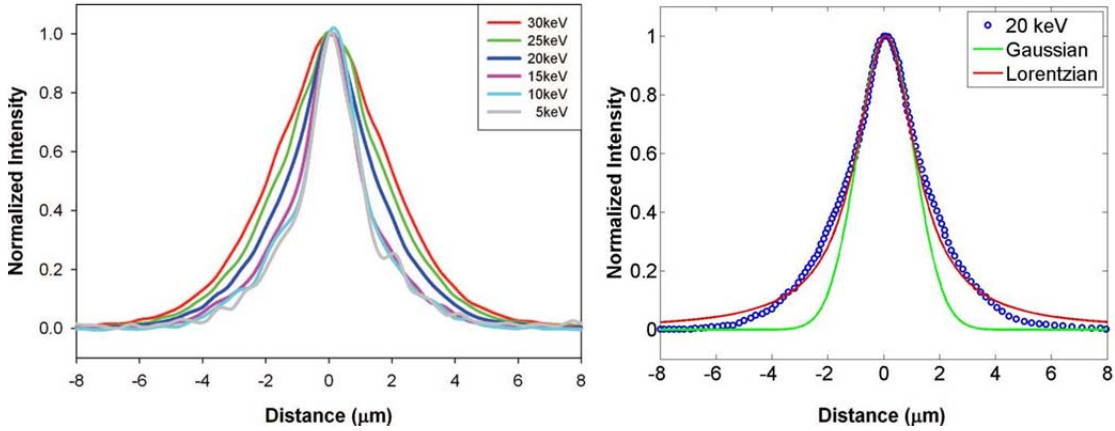


Figure 68. (a) Intensity distributions for *n*-type GaAs with beam energies from 5–30 kV, and (b) Gaussian and Lorentzian fits to the 20 keV intensity distribution. After [81].

D. HIGH-INJECTION MODEL

Finally, the 2D diffusion model is based on the assumptions of low-injection conditions in a doped semiconductor, resulting in a constant carrier lifetime. Low injection conditions mean that the excess carrier concentration generated by the electron beam is much less than the equilibrium concentration, or $n_e \ll n_0$. Doping allowed us to

say $n_0 = N_D$. For TlBr at 5 K, however, the equilibrium carrier concentration is ~ 0 due to the large bandgap and low temperature, and $n_e \gg n_0$, resulting in high-injection conditions. We must therefore re-visit our assumptions of the model and consider how high injection affects carrier lifetime and recombination. One change to the model is considered here.

The spontaneous radiative lifetime for band to band recombination was given previously as

$$\tau_R = \frac{n_e}{R} = \left[\frac{N_c N_v}{A k_B T (n_0 + p_0)} \right] \left[1 + \left(\frac{n_e}{n_0 + p_0} \right) \right]^{-1}. \quad (30)$$

Under low injection conditions where $n_0 = N_D$, Equation (30) reduced to

$$\tau_R = \frac{1}{B N_D}. \quad (34)$$

Here, the lifetime is independent of the excess carrier concentration. If instead, however, we assume high injection conditions, where $n_e \gg n_0$, and semi-insulating materials where $n_0 = p_0$, Equation (30) reduces to

$$\tau_R = \frac{1}{B n_e(x)}. \quad (35)$$

Now the lifetime depends on the excess carrier concentration. Additionally, we have indicated that the excess carrier concentration has a spatial dependence (1-D case shown). The spatial dependence results from a rapid decrease in excess carrier concentration as the carrier concentration gradient drives diffusion away from the generation volume [37].

If we define the recombination rate as

$$R = \frac{n_e(x)}{\tau_R} \quad (36)$$

then substitution of Equation (35) into Equation (36) results in a new expression for the recombination rate, given by

$$R = B [n_e(x)]^2 \quad (37)$$

The recombination rate now has a quadratic dependence on the excess carrier concentration [38].

The modified recombination rate is representative of one change to the model that should be considered for accurate modeling of semi-insulating materials in the high injection limit. This may be especially important in the case of a high-resistivity direct bandgap semiconductor, such as CZT. For TlBr, an indirect gap material where defect-mediated recombination is dominant, it appears likely that a constant lifetime model is appropriate, as indicated by the excellent fits obtained with the existing model for the Se-doped material. Further experimental studies as a function of doping would provide additional insight.

THIS PAGE INTENTIONALLY LEFT BLANK

IX. CONCLUSION

In this work, the transport properties of charge carriers in bulk semi-insulating semiconductors for nuclear radiation detectors have been investigated. Sample analysis has included undoped detector grade TlBr (45-S10) and doped TlBr (Na/Al/Ag, Cu/Fe/Zn, Se, and Pb), as well as CZT (ST1 and 372) under different post-growth conditions. Analytical techniques have included GDMS, EDX, TOF-SIMS, CL, PL, PICTS, and transport imaging using a 2D diffusion model for bulk materials. Using these methods we have demonstrated the following:

- Low temperature CL spectrum in TlBr.
- Application of a 2D model of carrier diffusion in bulk TlBr and CZT using transport imaging to advance a micro-characterization technique for rapid assessment of the magnitude and spatial variation in the $\mu\tau$ product at 2 μm resolution.
- Spatial variation in the ambipolar diffusion length in TlBr on a scale of $\sim 10 \mu\text{m}$.
- Contribution to first empirical energy level diagram for defect levels of Se and Pb in TlBr.
- Application of transport imaging in TlBr to demonstrate variations in charge transport properties in TlBr with doping/impurity levels.
- Application of transport imaging in TlBr and CZT to report variations in $\mu\tau$ product with temperature over the ranges 8 K–102 K and 5 K–60 K, respectively.
- First application of transport imaging for preliminary investigation of the effects of Te inclusions on charge transport in CZT.
- First application of transport imaging for preliminary investigation of the presence of photon recycling in TlBr and CZT.

The magnitude and spatial variation of the $\mu\tau$ product are critical to the high resolution performance of room temperature semiconductor gamma-ray detectors. The research presented in this dissertation can contribute to the development and evaluation of these materials and devices by providing a rapid, contact-free, all-optical technique for micro-scale characterization of fundamental charge transport properties.

APPENDIX A. CL MAP

The Matlab file **CL_map.m** opens a image file (.tif) and creates a CL map with a scale bar, as shown in Figure A1.

CL_map.m

```
clear
clc

% Load image file
image = '0723_BSE';
IO = imread([image '.tif']);
IO = double(IO); % [X Width 2184, Y Height 1472] in MicroCCD
sizeIO = size(IO);

% Normalize IO matrix
m=max(max(IO));
IO=IO/m;

% Plot Map
figure(1);
surf(IO);
view([0,-90]);
shading interp
colormap(hot)
colorbar
xlim([0,sizeIO(2)]); ylim([0,sizeIO(1)])
set(gca,'XTick',[],'XTickLabel',[])
set(gca,'YTick',[],'YTickLabel',[])
saveas(gcf,['CL_map_' image '.jpg'])
```

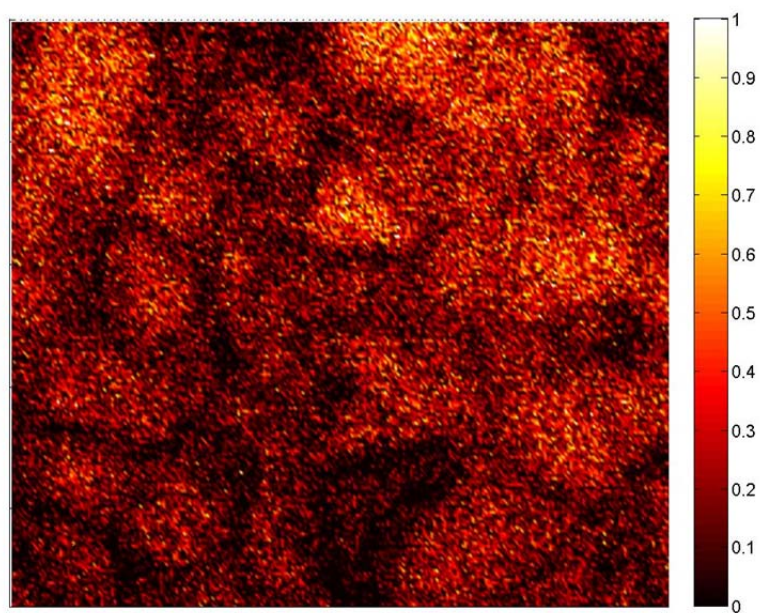


Figure A1. CL map.

APPENDIX B. CL SPECTRA

The Matlab file **CL_spectra.m** opens one or more .dat files and creates one or more CL spectrum, as shown in Figures B2 and B3. The code shown here also includes Gaussian fits to several peaks.

CL_spectra.m

```
-----
clc
clear

%% Load data file (.dat) and sample information

fileload = {...
    1, 'TlBr1', 'TlBr 45-S10', '2000x', '6E-10A', '295K', '23FEB11';
    2, 'TlBr9', 'TlBr 45-S10', '2000x', '3E-10A', '11 K', '23FEB11'};

k = size(fileload,1);

for j=1:k
    index{j} = fileload{j,1};
    datafile{j} = [fileload{j,2} '.dat'];
    sample{j} = fileload{j,3};
    mag{j} = fileload{j,4};
    current{j} = fileload{j,5};
    temp{j} = fileload{j,6};
    date{j} = fileload{j,7};
end;

%% Generate wavelength (X) and normalized intensity (Y) vectors

for j = 1:k
    fid = fopen(datafile{j});
    Header = textscan(fid,'%s',10,'delimiter','\n');
    Spectrum = textscan(fid, '%f %f');
    fclose(fid);

    c = 0; % 0 = wavelength x axis, 1 = energy x axis
    if c == 0
        X{j} = Spectrum{1,1};
        xaxis = 'Wavelength (nm)';
    elseif c == 1
        X{j} = 1.24*1000./Spectrum{1,1};
        xaxis = 'Energy (keV)';
    end
    Y{j} = Spectrum{1,2};
    Ymax{j} = max(Y{j});
    Ybkg{j} = min(Y{j});
    Y{j} = (Y{j}-Ybkg{j})/(Ymax{j}-Ybkg{j}); % Y values normalized to
```

1

```

end;

%% Plot Spectrum

x1=linspace(350,500,1001);
x10=416;
a1 = 5.5;
A1=0.84;
f1=@(x1) A1*exp(-(abs(x1-x10)/a1).^2);
G1=f1(x1);

x2=linspace(350,500,1001);
x20=428;
a2 = 10;
A2=1;
f2=@(x2) A2*exp(-(abs(x2-x20)/a2).^2);
G2=f2(x2);

x3=linspace(400,440,1001);
x30=417;
a3 = 10;
A3=0.06;
f3=@(x3) A3*exp(-(abs(x3-x30)/a3).^2);
G3=f3(x3);

% TlBr(45-S10), CL 295K
figure(1)
hold on
plot(X{1},Y{1},'b','LineWidth',2);
plot(x1,G1,'--r','MarkerSize',2,'LineWidth',1);
plot(x2,G2,'--g','MarkerSize',2,'LineWidth',1);
hold off
xlabel(xaxis,'FontSize',20,'FontWeight','b')
% xmin = 1.5; xmax = 3.6; xlim([xmin xmax])
xmin = 350; xmax = 800; xlim([xmin xmax])
ylabel('Intensity (Arb. units)','FontSize',20,'FontWeight','b')
% ymin = -0.1; ymax = 1.1; ylim([ymin ymax])
set(gca,'FontSize',16,'FontWeight','b'); % set(gcf,'Color',[1,1,1]);
legend('Data','Gaussian Fit 1','Gaussian Fit 2')
set(gca,'XMinorGrid','off','YGrid','off')
saveas(gcf,'295K.jpg')

% TlBr(45-S10), CL 11K
figure(2)
hold on
plot(X{2},Y{2},'b','MarkerSize',5,'LineWidth',2);
plot(x3,G3,'--r','MarkerSize',2,'LineWidth',2);
hold off
xlabel(xaxis,'FontSize',20,'FontWeight','b')
% xmin = 1.5; xmax = 3.6; xlim([xmin xmax])
xmin = 300; xmax = 800; xlim([xmin xmax])
ylabel('Intensity (Arb. units)','FontSize',20,'FontWeight','b')
ymin = -0.01; ymax = 1.1; ylim([ymin ymax])
set(gca,'FontSize',16,'FontWeight','b'); % set(gcf,'Color',[1,1,1]);

```

```
legend('Data','Gaussian Fit')
set(gca,'XMinorGrid','off','YGrid','off')
saveas(gcf,'11K.jpg')
```

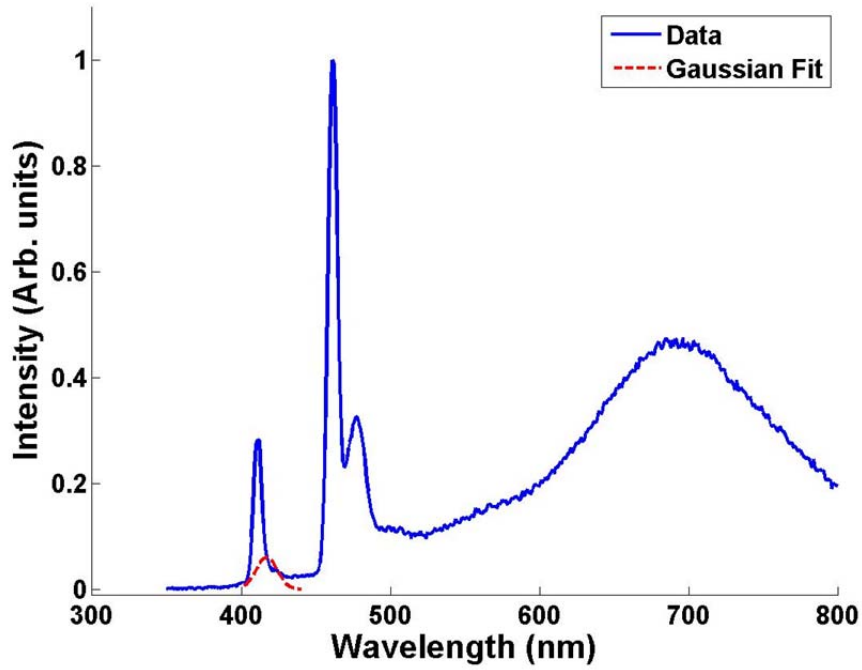


Figure B1. CL spectrum at 11 K.

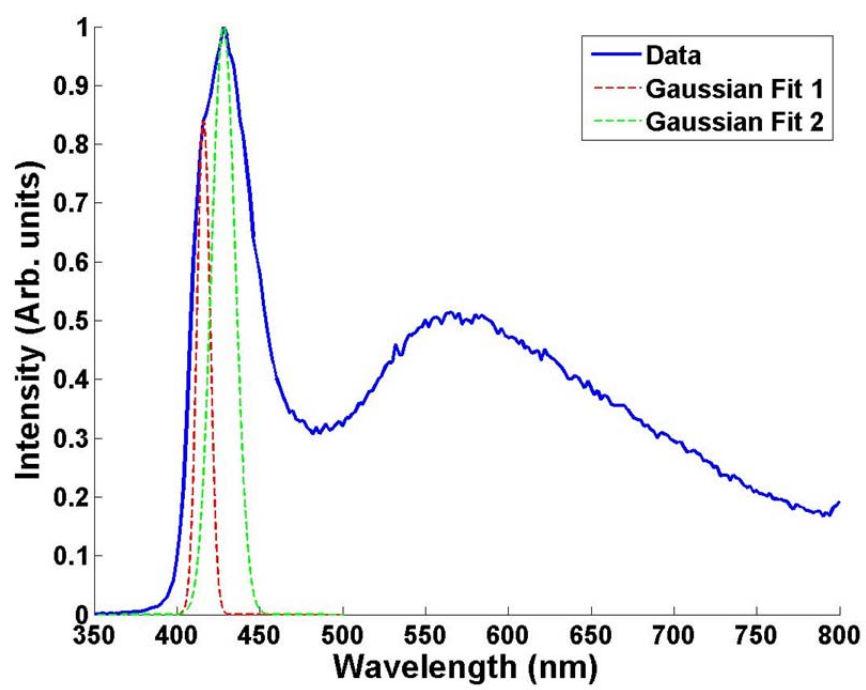


Figure B2. CL spectrum at 295 K.

APPENDIX C. INTENSITY DISTRIBUTION AND FIT

This appendix explains how to create the intensity distribution plots and fit the model to the data for multiple files.

Begin by loading and analyzing the image files. Use **Loaddata_multifile.m**. Enter the line image file names in the “File Information” section of **Loaddata_multifile.m**.

The call structure is as follows:

```
Loaddata_multifile.m  
    Tiff2data4fit_multifile.m  
        CenterCut_v2.m  
        Norm4fit.m  
        makeX.m  
        sdvec.m  
        reduce_outliers.m (optional)
```

The result is a matlab file (.mat) with the filename “data_...”

To plot the intensity distribution, use **plot_distribution_RHS.m**. This script loads and plots the data files, as shown in Figure C1.

To fit the data, use **fit_LMA_LVA_v1_multifile.m**.

The call structure is as follows:

```
fit_LMA_LVA_v1_multifile.m  
    LMA_LVA_v1.m  
        Ueval_v8.m  
        UpartL_v7.m  
        UpartV_v8.m  
        polyEstimate.m  
            Ueval_v8.m  
            errorfit.m  
            fitplot.m  
        ConvergeCheck.m  
fitPlot.m
```

Loaddata_multifile.m

```
clc
clear
clf reset

%% File Information

fileload = {...
    1, 'ST1_line1_180s_500x_6E-10A_10kV_8.12mm_295K_x492.png',
    'CZT(ST1)', 'L1', 'x492', '295K', '22NOV11';
    2, 'ST1_line1_180s_500x_6E-10A_10kV_8.12mm_295K_x391.png',
    'CZT(ST1)', 'L1', 'x391', '295K', '22NOV11';
    3, 'ST1_line1_180s_500x_6E-10A_10kV_8.12mm_295K_x732.png',
    'CZT(ST1)', 'L1', 'x732', '295K', '22NOV11'; % OMIT
    4, 'ST1_line2_180s_500x_6E-10A_10kV_8.15mm_295K_x322.png',
    'CZT(ST1)', 'L2', 'x322', '295K', '22NOV11';
    5, 'ST1_line2_180s_500x_6E-10A_10kV_8.15mm_295K_x199.png',
    'CZT(ST1)', 'L2', 'x199', '295K', '22NOV11'};

k = size(fileload,1);

for j=1:k
    index{j}=fileload{j,1};
    imagefile{j}=fileload{j,2};
    sample{j}=fileload{j,3};
    location{j}=fileload{j,4};
    line{j}=fileload{j,5};
    temp{j}=fileload{j,6};
    date{j}=fileload{j,7};
    datafile{j}=(['data ' sample{j} ' ' location{j} ' ' line{j} ' '
temp{j} ' ' date{j}]);
end

%% FUNCTION CALL FOR CUTTING OF THE IMAGE FILE AND SAVING DATA VECTOR

for j = 1 % manually iterate through filenames for all files
    [DataVec X IO R varvec] = Tiff2data4fit_multifile(imagefile{j},
sample{j});
    save(datafile{j}, 'DataVec', 'X', 'IO', 'R', 'varvec')
end;
```

Tiff2data4fit_multifile.m

```
function [ DataVec X IO R varvec] = Tiff2data4fit_multifile( image,
sample)

IO = imread(image);
IO = double(IO); % [X Width 2184, Y Height 1472] in MicroCCD
IO = IO';

%% Surface plot of data
figure1 = figure(1);
clf('reset');
axes1 = axes('Parent',figure1,'CLim',[0 1]);
view(axes1,[0 0]);
grid(axes1,'minor');
hold(axes1,'all');
surf1(IO)
shading interp
colormap copper
title(sample)
xlabel('row','VerticalAlignment','cap','HorizontalAlignment','center');
ylabel('column','Visible','off','HorizontalAlignment','center');

%% First cut of Data
clc

% Rstart1 = 0;
% Rend1 = 500;

Rstart1 = input('\nInput start range for desired Row data (1st cut):
');
Rend1 = input('Input end range for desired Row data: ');
for I = 1:Rend1-Rstart1+1
    T1(:,I) = IO(:,I+Rstart1);
end
IO = T1;

%% Surface plot of data
clf('reset');
figure1 = figure(1);
axes1 = axes('Parent',figure1,'CLim',[0 1]);
view(axes1,[0 0]);
grid(axes1,'minor');
hold(axes1,'all');
surf1(IO)
shading interp
colormap copper
title(sample)
xlabel('row','VerticalAlignment','cap','HorizontalAlignment','center');
ylabel('column','Visible','off','HorizontalAlignment','center');

%% Second cut of data in same direction
Rstart2 = input('\nInput start range for desired Row data (2nd cut):
');
```

```

Rend2 = input('Input end range for desired Row data (2nd cut): ');

R=[Rstart1 Rend1 Rstart2 Rend2];

for I = 1:Rend2-Rstart2+1
    T2(:,I) = IO(:,I+Rstart2);
end
IO = T2;

%% Surface plot of data
clf('reset');
figure1 = figure(1);
axes1 = axes('Parent',figure1,'CLim',[0 1]);
view(axes1,[89 15]);
grid(axes1,'minor');
hold(axes1,'all');
surf1(IO)
shading interp
colormap copper
title(sample)
xlabel('row','VerticalAlignment','cap','HorizontalAlignment','center');
ylabel('column','Visible','off','HorizontalAlignment','center');

%% Save Ridge figure before CenterCut and X vec generation
%
% clf
% figure1 = figure(1);
% axes1 = axes('Parent',figure1,'CLim',[0 1]);
% view(axes1,[0 0]);
% grid(axes1,'minor');
% hold(axes1,'all');
% surf1(IO)
% shading interp
% colormap copper
% title(strcat(sample, ' (Before CenterCut)'))
%
% xlabel('row','VerticalAlignment','cap','HorizontalAlignment','center');
% ylabel('column','Visible','off','HorizontalAlignment','center');
%
% %% Surface plot of data
% % clf reset;
% figure2 = figure(2);
% axes1 = axes('Parent',figure2,'CLim',[0 1]);
% view(axes1,[89 15]);
% grid(axes1,'minor');
% hold(axes1,'all');
% surf1(IO)
% shading interp
% colormap copper
% title(sample)
%
% xlabel('row','VerticalAlignment','cap','HorizontalAlignment','center');
% ylabel('column','Visible','off','HorizontalAlignment','center');

```



```

%% Reducing outlayers
% - if g is set to 0 then this section is skipped
%
% - if g is set to 1 then any value in that is more than 1 std away
from
%     values in the row will be set to the mean of that row
g = 0;
if g == 1
    IO = reduce_outliers(IO);
end

%% Centering and X vec generator

Xmax = input('\nEnter the number of pixels to the right of the peak to
keep: ');
% Xmax = 1000;

[IO] = CenterCut_v2(IO,Xmax);

% close(figure2);
figure3 = figure(3);
% clf('reset');
axes1 = axes('Parent',figure3,'CLim',[0 1]);
view(axes1,[90 0]);
grid(axes1,'minor');
hold(axes1,'all');
surf1(IO)
shading interp
colormap copper
title(sample)
% title(strcat(sample, ' (After CenterCut)'))
% title(strcat('Post-CenterCut Data for ', sample))
xlabel('row','VerticalAlignment','cap','HorizontalAlignment','center');
ylabel('column','Visible','off','HorizontalAlignment','center');

%% Setting max value to 1
IO = Norm4fit(IO);

%% Takes the mean of the rows of the matrix to create a single vector
DataVec = mean(IO);

%% Cuts the DataVec
% so that the values of DataVec are above the noise and background
levels
[X] = makeX(DataVec);
varvec = sdvec(X,IO);

%% Benediction
display(' ')
display('Goodbye!')
display(' ')

```

CenterCut_v2.m

```
function [ BB ] = CenterCut_v2( AA , Xmax)

% This will cut the matrix AA so that the columns will be of length
Xmax
% Position 1 of the AA matrix is the max value of that column

[M,N]= size(AA);

DV = mean(AA');
n1 = max(DV);
n2 = find((DV) == n1,1,'first');

for I = 1:N
    n3 = find(AA(:,I) == max(AA(n2-20:n2+20,I)),1,'last');
    BB(:,I) = AA(n3:n3+Xmax-1,I);
end

end
```

Norm4fit.m

```
function [ BB ] = Norm4fit( AA )
% For each row in AA, a background noise level is calculated by taking
a
% mean of the furthest 20 value counts away from the source and then
% subtracting this background noise level from each value in that row

% The rows are then normalized to a max value of '1'

[M,N] = size(AA);

for I = M-19:M
    n1(I-M+20) = mean(AA(I,1:N));
end
AA = AA-mean(n1);

for I=1:N
    n2=AA(1,I);
    BB(:,I)= AA(:,I)./(n2);
end

end
```

makeX.m

```
function [ X ] = makeX( DataVec )

% creates the X vector of same length as DataVec with .4 as stepsizes

% N - length of DataVec

[M,N] = size(DataVec);

[M,N] = size(DataVec);
X=0:N-1;
X = X*(.4e-6);

end
```

sdvec.m

```
function [ varvec ] = sdvec( X ,IO )

[m1,n1] = size(X);
varvec = zeros(m1,n1);
for i=1:n1
    varvec(i)=std(IO(i,:));
end

end
```

reduce_outliers.m (optional)

```
function [ IO ] = reduce_outliers( IO )
%Any value in that is more than 2 std away from
%values in the row will be set to the mean of that row

for I=1:size(IO,1)
    a = 2*std(IO(I,:));
    b = mean(IO(I,:));
    for J=1:size(IO,2)
        if IO(I,J)>=b+a
            IO(I,J)=b;

            elseif IO(I,J)<=b-a
                IO(I,J)=b;
            end
        end
    end
end

end
```

plot_distribution_RHS.m

```
clc
clear
clf reset

%% File Information

fileload = {...
    1, 'ST1_line1_180s_500x_6E-10A_10kV_8.12mm_295K_x492.png',
    'CZT(ST1)', 'L1', 'x492', '295K', '22NOV11';
    2, 'ST1_line1_180s_500x_6E-10A_10kV_8.12mm_295K_x391.png',
    'CZT(ST1)', 'L1', 'x391', '295K', '22NOV11';
    3, 'ST1_line1_180s_500x_6E-10A_10kV_8.12mm_295K_x732.png',
    'CZT(ST1)', 'L1', 'x732', '295K', '22NOV11';
    4, 'ST1_line2_180s_500x_6E-10A_10kV_8.15mm_295K_x322.png',
    'CZT(ST1)', 'L2', 'x322', '295K', '22NOV11';
    5, 'ST1_line2_180s_500x_6E-10A_10kV_8.15mm_295K_x199.png',
    'CZT(ST1)', 'L2', 'x199', '295K', '22NOV11'};

k = size(fileload,1);

for j=1:k
    index{j}=fileload{j,1};
    imagefile{j}=fileload{j,2};
    sample{j}=fileload{j,3};
    location{j}=fileload{j,4};
    line{j}=fileload{j,5};
    temp{j}=fileload{j,6};
    date{j}=fileload{j,7};
    datafile{j}=[ 'data' sample{j} ' ' location{j} ' ' line{j} ' '
temp{j} ' ' date{j}];
end

DATA = [index' sample' location' line' temp' date']

%% PLOT DISTRIBUTIONS

for j = 1:k
    S{j} = load(datafile{j});
    X{j} = S{j}.X*1e6;
    Y{j} = S{j}.DataVec;
end;

%%

% 295K
figure(1)
semilogy(...
    X{1},Y{1}, 'r', ...
    X{2},Y{2}, 'g', ...
    X{3},Y{3}, 'b', ...
    X{4},Y{4}, 'm', ...
```

```

X{5},Y{5},'k',...
'MarkerSize',5,'LineWidth',2);
xlabel('Position (\mum)','FontSize',20,'FontWeight','b')
xmin = 0; xmax = 25; xlim([xmin xmax])
ylabel('Intensity (Arb. units)','FontSize',20,'FontWeight','b')
ymin = 1e-3; ymax = 1; ylim([ymin ymax])
set(gca,'FontSize',16,'fontWeight','b'); % set(gcf,'Color',[1,1,1]);
set(gca,'XMinorGrid','off','YMinorGrid','off')
A = [sample{1} ' ' location{1} ' ' line{1} ' ' temp{1}];
B = [sample{2} ' ' location{2} ' ' line{2} ' ' temp{2}];
C = [sample{3} ' ' location{3} ' ' line{3} ' ' temp{3}];
D = [sample{4} ' ' location{4} ' ' line{4} ' ' temp{4}];
E = [sample{5} ' ' location{5} ' ' line{5} ' ' temp{5}];
legend(A,B,C,D,E,'Location','NorthEast');
figurenamesave = [sample{1} '_' sample{4} '_' temp{1}];
saveas(gcf,[figurenamesave '.jpg']);

```

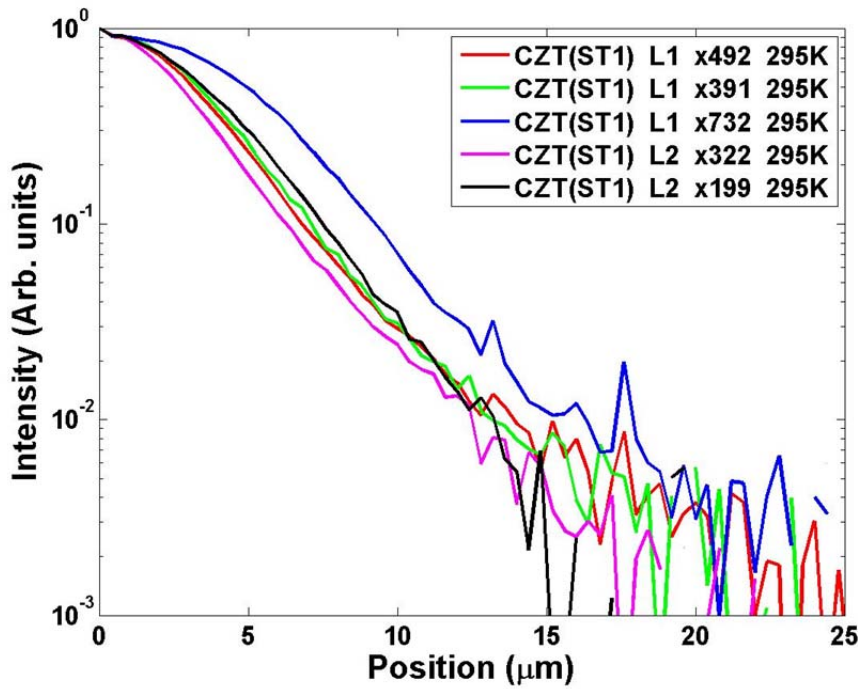


Figure C1. Intensity distribution.

fit_LMA_LVA_v1_multifile.m

```
format short e
format compact

clc
clear

%% File Information

fileload = {...
    1, 'ST1_line1_180s_500x_6E-10A_10kV_8.12mm_295K_x492.png',
    'CZT(ST1)', 'L1', 'x492', '295K', '22NOV11';
    2, 'ST1_line1_180s_500x_6E-10A_10kV_8.12mm_295K_x391.png',
    'CZT(ST1)', 'L1', 'x391', '295K', '22NOV11';
    3, 'ST1_line1_180s_500x_6E-10A_10kV_8.12mm_295K_x732.png',
    'CZT(ST1)', 'L1', 'x732', '295K', '22NOV11';
    4, 'ST1_line2_180s_500x_6E-10A_10kV_8.15mm_295K_x322.png',
    'CZT(ST1)', 'L2', 'x322', '295K', '22NOV11';
    5, 'ST1_line2_180s_500x_6E-10A_10kV_8.15mm_295K_x199.png',
    'CZT(ST1)', 'L2', 'x199', '295K', '22NOV11'};

k = size(fileload,1);

for j=1:k
    index{j}=fileload{j,1};
    imagefile{j}=fileload{j,2};
    sample{j}=fileload{j,3};
    location{j}=fileload{j,4};
    line{j}=fileload{j,5};
    temp{j}=fileload{j,6};
    date{j}=fileload{j,7};
    datafile{j}=(['data ' sample{j} ' ' location{j} ' ' line{j} ' '
temp{j} ' ' date{j}]);
end

for j=1:k
    file_name_2_load{j} = datafile{j};
    filename_4_save{j} = (['fit ' sample{j} ' ' location{j} ' ' line{j}
' ' temp{j} ' ' date{j}]);
    file1{j} = load(file_name_2_load{j});
end

%% INITIAL PARAMETERS
% initial inputs for parameters are to be entered for pvec_start vector

L = 10;    % enter L in microns
V = 8;     % enter V in 1/micron
Zo = 0.5;  % enter Zo in microns
A = 40;

%%%%%%%%%%%%%%%%%%%%%%%%%%%%%%%%%%%%%%%%%%%%%%%%%%%%%%%%%%%%%%%%%%%%%%%%%
```

```

first_data_point_2_use = 11;          % [11,15]=4-10 um; [11,20]=4-12
um; [11,30]=4-16 um; [11,40]=4-20 um; [11,115]=4-50 um;
number_of_data_points_2_use = 115;    % [6,15]=2-8 um;   [6,25]=2-12;
[6,35]=2-16;      [6,45]=2-20 um;   [6,50]=2-22 um;

pvec = [L V Zo A];
initial_pvec = pvec;
%%#####

%%

j=1;

for j=1:k
    Xvec{j} = file1{j}.X*1e6;
    Dvec{j} = file1{j}.DataVec;

    cc=1e-5;

    xvec = Xvec{j}(first_data_point_2_use:first_data_point_2_use+
number_of_data_points_2_use );
    dvec = Dvec{j}(first_data_point_2_use:first_data_point_2_use+
number_of_data_points_2_use );

    display(' ');
    display('Start - new loop');
    display('----- ');
    jj=1;

    [ L V A phi]=LMA_LVA_v1(pvec(1),pvec(2),pvec(3),pvec(4), xvec,
dvec,cc );
    pvec(1)=L;
    pvec(2)=V;
    pvec(3)=Zo;
    pvec(4)=A;

    [uest] = fitPlot(pvec(1), pvec(2), pvec(3), pvec(4), xvec, dvec,
filename_4_save{j});

    save(filename_4_save{j}, 'pvec', 'first_data_point_2_use', 'number_of_data
_points_2_use', 'initial_pvec', 'xvec', 'dvec', 'uest')

    display('Goodbye')

end

%% Comments/notes

% pvec - parameter vector [ L V Zo A]
% M - matrix of most recent 10 parameters [phi ; L ; V ; Zo ; A]
% phi - squared error vector (evec.*evec)
% evec - error vector
% L - diffusion length in meters

```



```

% V - S/D in 1/sec
% Zo - penetration depth of electron beam for model
% A - Amplitude of model

% FIT - is the final matrix that contains the data for each of the fits
% Lfit - temporary vector to save corresponding final values for L
% Vfit - same - for V
% Afit - same for A
% phifit - same for phi

% Dvec - vector of with all data points recorded
% dvec - vector in use for fitting of current data set

% Xvec - position vector of all the x-values
% xvec - position vector in use for fitting current data set

% Uest - Full length vector of fitted values with current parameters
% uest - vector of fitted values cut to desired length

% UpL - vector of partial derivatives with respect to L
% UpV - wrt V
% UpZ - wrt Z
% UpA - wrt A

% Ln - normalized vector of partial derivatives with respect to L
% Vn - wrt V
% Zn - wrt Z
% An - wrt A
% En - normalized error vector

% grad - gradient vector with the four parameters
% Ngrad - normalized gradient vector

% first_data_point_2_use - # of data points moving away from the source
to skip
% number_of_data_points_2_use - # of data points to be used in the
fitting of the model

% M - Matrix that contains the last 10 values through the iteration
%   process for [phi pvec(1) pvec(2) pvec(3) pvec(4) phistep ]
% cc - is the percentage of change in each parameter of pvec allowed to
%   determine convergence

% gM - AMatrix of 4 columns consisting of the normalized partials
derivatives
%   for UpL, UpV, UpZ, UpA

% LMA - Levenberg-Marquardt-Algorithm step direction

% stepvec - vector used to gauge the best next step between the max
and
%   min of the step vector

```

```

% stepVecVariance - the amount that will be used in varying phistep (as
a
%               percentage) when creating the next 'stepvec'
% stepvec_start - used to keep track of the initial stepvec so that if
%               max(stepvec) is greater than '1' stepvec will be
reset
%               to 'stepvec_start'

% fitcount - the number of times that the fitting will be performed -
the
%               fit with the lowest phi value in all this will be used.
% fitmat - matrix used to store the fitted values for each iteration of
%               fitcount

```

LMA_LVA_v1.m

```
function [ L V A phi b] = LMA_LVA_v1(L,V ,Zo,A ,xvec, dvec, cc)
pvec=[L V Zo A];

format long e
% pvec - parameter vector [ L V Zo A]
% M - matrix of most recent 10 parameters [phi ; L ; V ; Zo ; A]
% phi - squarred error vector (evec.*evec)
% evec - error vector

% Dvec - vector of with all data points recorded
% dvec - vector in use for fitting of current data set

% Xvec - position vector of all the x-values
% xvec - position vector in use for fitting current data set

% Uest - Full length vector of fitted values with current parameters
% uest - vector of fitted values cut to desird length

% UpL - vector of partial derrivatives with respect to L
% UpV - wrt V
% UpZ - wrt Z
% UpA - wrt A

% Ln - normalized vector of partial derrivatives with respect to L
% Vn - wrt V
% Zn - wrt Z
% An - wrt A
% En - normalized error vector

% grad - gradient vector with the four paramter
% Ngrad - normalized gradient vector

% dp2skip - # of data points moving away from the source to skip
% dp2use - # of data points to be used in the fitting of the model

% M - Matrix that contains the last 10 values throught the iteration
% process for [phi pvec(1) pvec(2) pvec(3) pvec(4) phistep ]
% cc - is the percentage of change in each paramter of pvec allowed to
% determine convergence

% gM - AMatrix of 4 columes consiting of the normalized partials
derivatives
% for UpL,UpV,UpZ,UpA

% LMA - Levenberg-Marquardt-Algorithm step direction

% stepvec - vector used to gage a the best next step between the max
and
% min of the step vector
% stepVecVariance - the amount that will be used in varying phistep (as
a
```

```

%               percentage) when creating the next 'stepvec'
% stepvec_start - used to keep track of the initial stepvec so that if
%               max(stepvec) is greater than '1' stepvec will be
reset
%               to 'stepvec_start'

jj=0;
converge=0;
M = zeros(10,6);
tic

phistep = .9;
stop=7;
cc=1e-6;
see =5 ;
lambda = 1e0;
nu = 3;
phi=0;

while converge ==0;

    jj=jj+1;
    uest = Ueval_v8(pvec(1),pvec(2),pvec(3),pvec(4),xvec);
    UpL = UpartL_v7(pvec(1),pvec(2),pvec(3),pvec(4), xvec);
    UpV = UpartV_v8(pvec(1),pvec(2),pvec(3),pvec(4), xvec);
    UpA = uest/pvec(4);

    evec = (uest-dvec);
    Aphi   = evec*evec';
    % a1 = [UpL ; UpV ; UpA ]';
    a1 = [UpL/norm(UpL) ; UpV/norm(UpV); UpA/norm(UpA)]';
    b = -(a1'*a1+lambda*diag(diag(a1'*a1)))\'(a1'*evec');
    LMA = b'/norm(b);

    Bpvec = [pvec(1)+LMA(1)*phistep*pvec(1)
    pvec(2)+LMA(2)*phistep*pvec(2) pvec(3) pvec(4)+LMA(3)*phistep*pvec(4)];
    Buest = Ueval_v8(Bpvec(1),Bpvec(2),Bpvec(3),Bpvec(4),xvec);
    Bevec = Buest-dvec;
    Bphi = Bevec*Bevec';
    phistepL=phistep;
    k=0;
    if Bphi<Aphi
        if lambda <1e-10
            Aphi=Bphi;
        end
        while Bphi<Aphi
            k=k+1;
            Aphi = Bphi;
            Blambda=lambda/(nu^k);
            b = -(a1'*a1+Blambda*diag(diag(a1'*a1)))\'(a1'*evec');
            LMA = b'/norm(b);
            phistep = polyEstimate( pvec, LMA,xvec,dvec,phistepL,stop
);

```

```

        Bpvec = [pvec(1)+LMA(1)*phistep*pvec(1)
pvec(2)+LMA(2)*phistep*pvec(2) pvec(3) pvec(4)+LMA(3)*phistep*pvec(4)];
        Buest = Ueval_v8(Bpvec(1),Bpvec(2),Bpvec(3),Bpvec(4),xvec);
        Bevec = Buest-dvec;
        Bphi = Bevec*Bevec';
        if Blambda <1e-10
            Aphi=Bphi;
        end
    end
    k=k-1;
else
    Clambda=lambda/(nu);
    b = -(a1'*a1+Clambda*diag(diag(a1'*a1)))\'(a1'*evec');
    LMA = b'/norm(b);
    phistep = polyEstimate( pvec, LMA,xvec,dvec,phistepL ,stop );
    Cpvec = [pvec(1)+LMA(1)*phistep*pvec(1)
pvec(2)+LMA(2)*phistep*pvec(2) pvec(3) pvec(4)+LMA(3)*phistep*pvec(4)];
    Cuest = Ueval_v8(Cpvec(1),Cpvec(2),Cpvec(3),Cpvec(4),xvec);
    Cevec = Cuest-dvec;
    Cphi = Cevec*Cevec';

    if Cphi<Aphi
        k=k+1;
        Bphi=Cphi;
        if lambda <1e-10
            Aphi=Bphi;
        end
        while Bphi<Aphi
            k=k+1;
            Aphi = Bphi;
            Blambda=lambda/(nu^k);
            b = -(a1'*a1+Blambda*diag(diag(a1'*a1)))\'(a1'*evec');
            LMA = b'/norm(b);
            phistep = polyEstimate( pvec, LMA,xvec,dvec,phistepL
,stop );
            Bpvec = [pvec(1)+LMA(1)*phistep*pvec(1)
pvec(2)+LMA(2)*phistep*pvec(2) pvec(3) pvec(4)+LMA(3)*phistep*pvec(4)];
            Buest =
Ueval_v8(Bpvec(1),Bpvec(2),Bpvec(3),Bpvec(4),xvec);
            Bevec = Buest-dvec;
            Bphi = Bevec*Bevec';
            if Blambda <1e-10
                Aphi=Bphi;
            end
        end
        k=k-1;
    else
        if lambda >1e10
            Aphi=Bphi;
        else
            k=k-1;
        end
        while Aphi<Bphi
            k=k-1;
            Bphi=min(Aphi,Bphi);

```

```

        Alambda=lambda/(nu^k);
        b = -(a1'*a1+Alambda*diag(diag(a1'*a1)))\'(a1'*evec');
        LMA = b'/norm(b);
        phistep = polyEstimate( pvec, LMA,xvec,dvec,phistepL
,stop );

        Apvec = [pvec(1)+LMA(1)*phistep*pvec(1)
pvec(2)+LMA(2)*phistep*pvec(2) pvec(3) pvec(4)+LMA(3)*phistep*pvec(4)];
        Auest =
Ueval_v8(Apvec(1),Apvec(2),Apvec(3),Apvec(4),xvec);
        Aever = Auest-dvec;
        Aphi = Aever*Aever';
        if Alambda >1e10
            Aphi=Bphi;
        end

    end

    Bpvec=Apvec;
    k=k+1;
end
end
lambda=lambda/(nu^k);
% a1 = [UpL/norm(UpL) ; UpV/norm(UpV); UpA/norm(UpA)]';
b = -(a1'*a1+lambda*diag(diag(a1'*a1)))\'(a1'*evec');
LMA = b'/norm(b);
phistep = polyEstimate( pvec, LMA,xvec,dvec,phistepL ,stop );

pvec = [pvec(1)+LMA(1)*phistep*pvec(1)
pvec(2)+LMA(2)*phistep*pvec(2) pvec(3) pvec(4)+LMA(3)*phistep*pvec(4)];
uest = Ueval_v8(Bpvec(1),Bpvec(2),Bpvec(3),Bpvec(4),xvec);
evec = uest-dvec;
phi = evec*evec';

M(1:9,1:6)=M(2:10,1:6);
M(10,:)=[phi pvec(1) pvec(2) pvec(3) pvec(4) phistep ];

converge = ConvergeCheck(M,cc);
%     if converge == 1
%         if stop <6
%             converge=0;
%             stop=stop+1;
%             cc=cc/5;
%             display(' ##### YAHOOOO
#####')
%             M = zeros(10,6);
%             M(10,:)=[phi pvec(1) pvec(2) pvec(3) pvec(4) phistep ];
%
%             Lname = 'L = ';
%             Vname = ', V = ';
%             Zname = ', Zo = ';
%             Aname = ', A = ';
%
%             p1 = 'step =';
%             p2 = ', phi =';

```

```

%           L1 = ',   LMA  = ';
%           lam = ',   time =';
%           lam1 = ',   jj count  =';
%           lam2 = ',   lambda =';
%           time1= toc;
%           fprintf('%s %1.4e %s %1.5e %s %1.4e %s %1.4e %s   %4.3f
%10s %4.3e  \n'...
%               ,Lname,pvec(1),Vname,pvec(2),Zname,pvec(3),
Aname,pvec(4), lam,time1,lam2,lambda')
%
%           fprintf('%s %1.10f %s %1.9e %s %3.3e %s %4.4e %4.4e %4.4e
\n \n \n'...
%               ,p1, phistep,p2, phi,lam1,jj, L1 , LMA(1) , LMA(2)
,LMA(3));
%           fitPlot( pvec(1), pvec(2) ,pvec(3),pvec(4)
,xvec,dvec,'test' );
%           pause(.01)
%
%
%           end
%       end

    if mod(jj,see)==1;
        Lname = 'L = ';
        Vname = ',   V = ';
        Zname = ',   Zo = ';
        Aname = ',   A = ';

        p1 = 'step =';
        p2 = ',   phi =';
        L1 = ',   LMA  = ';
        lam = ',   time =';
        lam1 = ',   jj count  =';
        lam2 = ',   lambda =';
        time1= toc;
        fprintf('%s %1.4e %s %1.5e %s %1.4e %s %1.4e %s   %4.3f %10s
%4.3e  \n'...
            ,Lname,pvec(1),Vname,pvec(2),Zname,pvec(3), Aname,pvec(4),
lam,time1,lam2,lambda')

        fprintf('%s %1.10f%s %1.9e %s %3.3e %s %4.4e %4.4e %4.4e  \n
\n \n'...
            ,p1, phistep,p2, phi,lam1,jj, L1 , LMA(1) , LMA(2)
,LMA(3));
        fitPlot( pvec(1), pvec(2) ,pvec(3),pvec(4) ,xvec,dvec,'test' );
        pause(.01)

    end

end

L = pvec(1);
V = pvec(2);
Zo = pvec(3);

```

```

A = pvec(4);

Lname = 'L = ';
Vname = ', V = ';
Zname = ', Zo = ';
Aname = ', A = ';

p1 = 'step =';
p2 = ', phi =';
L1 = ', LMA = ';
lam = ', time =';
lam1 = ', jj count =';
lam2 = ', lambda =';
time1= toc;
fprintf('%s %1.4e %s %1.5e %s %1.4e %s %1.4e %s %4.3f %10s %4.3e
\n'...
,Lname,pvec(1),Vname,pvec(2),Zname,pvec(3), Aname,pvec(4),
lam,time1,lam2,lambda')

fprintf('%s %1.10f %s %1.9e %s %3.3e %s %4.4e %4.4e %4.4e \n \n \n'...
,p1, phistep,p2, phi,lam1,jj, L1 , LMA(1) , LMA(2) ,LMA(3));

fitPlot( pvec(1), pvec(2) ,pvec(3),pvec(4) ,xvec,dvec,'test' );
pause(.01)

end

```

Ueval_v8.m

```
function [ Uest ] = Ueval_v8( L,V,Zo,A,xvec )
% evaluates U by the provided inputs
% this requires the evaluation of two integrals. 'f1' and 'f2'
% ef (easy function) is used to simplify f1 and f2

k = length(xvec);
U1 = zeros(1,k);
U2 = zeros(1,k);
U3 = zeros(1,k);

%%

parfor n=1:k
    a=1e-13;
    b=1e-13;

    x = xvec(n);
    %%
    LL= x/L;

    ef = @(t) sqrt( t.^2 - (x/L).^2 );
    f1 = @(t) bessellk(1,t).*ef(t);

    U1(n)=
quadgk(f1,LL,Inf, 'RelTol',a, 'AbsTol',b, 'MaxIntervalCount',9999999);

    %%

    % f3 = @(r) bessellk(0,sqrt(r+(x/L)^2)).*(exp(V*(Zo-L.*sqrt(r)))-
1)./(2.*sqrt(r));
    % LL=(Zo/L)^2;

    % f3 = @(r) bessellk(0,sqrt(r+x^2)/L).*( exp(V*(Zo-sqrt(r)))-1
)./(2*L.*sqrt(r));
    % LL=Zo^2;

    f3 = @(r) bessellk(0,sqrt(r.^2+x^2)/L).*( exp(V*(Zo-r))-1 )./L;
    LL=Zo;

    U3(n)=
quadgk(f3,LL,Inf, 'RelTol',a, 'AbsTol',b, 'MaxIntervalCount',9999999);

end

Uest=(U1+U3)*A;

end
```

UpartL_v7.m

```

function [ UpL ] = UpartL_v7( L,V,Zo,A,xvec )
% This function calculates the partial derrivative of
%   u(L,V,Z,A) with respect to L

% takes as inputs the value for each variable L,V,Z,A
%   and a vector of concerened x values

% sends as output a vector with the partial of u wrt L
%   evaluated at each of the x vaules in the xvec
%display('UparL')
%tic
k = length(xvec);
I1 = zeros(1,k);
I2 = zeros(1,k);
I3 = zeros(1,k);

a=1e-13;
b=1e-13;

parfor n=1:k
    x = xvec(n);
    LL= x/L;

    ef = @(t) sqrt( t.^2 - (x/L)^2 );
    f1 = @(t) bessellk(2,t).*ef(t).*(x^2/L^3)./t;

    I1(n)=
quadgk(f1,LL,Inf, 'RelTol',a, 'AbsTol',b, 'MaxIntervalCount',9999999);

%%

%       f2 = @(r) bessellk(0,sqrt(r+(x/L)^2)).*( (-
V*(r+(x/L)^2).exp(V*(Zo-L.*sqrt(r)))./(r) ) + ...
%       (1- exp(V*(Zo-L.*sqrt(r))) ).*x^2./(L^3*r.^(3/2)) )/2;
%       LL= (Zo/L)^2;

%       f2 = @(r) (1-exp(V.*(Zo-sqrt(r))))./(2*L^2.*sqrt(r)).*(
bessellk(1,sqrt(r+x^2)./L).*(sqrt(r+x^2)./L)-bessellk(0,sqrt(r+x^2)./L)
);
%       LL= Zo^2;

%       f2 = @(r) 1/(L^2)*(1-exp(V.*(Zo-
r))).*(bessellk(1,sqrt(r.^2+x^2)./(L)).*sqrt(r.^2+x^2)./(L)-
bessellk(0,sqrt(r.^2+x^2)./(L)));
    LL= Zo;

```

```
    I2(n)=  
quadgk(f2,LL,Inf,'RelTol',a,'AbsTol',b,'MaxIntervalCount',9999999);
```

```
end
```

```
UpL=(I1+I2)*A;
```

```
end
```

UpartV_v8.m

```
function [ UpV ] = UpartV_v8( L,V,Zo,A,xvec )
% This function calculates the partial derrivative of
%   u(L,V,Z,A) with respect to V

% takes as inputs the value for each variable L,V,Z,A
%   and a vector of concerened x values

% sends as output a vector with the partial of u wrt V
%   evaluated at each of the x vaules in the xvec
%display('UpartV')
%tic
k = length(xvec);
UpV = zeros(1,k);

%%

a=100*eps;
b=1e-23;

parfor n=1:k

    int1=0;
    x = xvec(n);

    tt = 3;

    if tt == 1
        LL = (Zo/L)^2;
        f1 = @(r) bessellk(0,sqrt(r+(x/L)^2)).*(Zo-
L.*sqrt(r)).*exp(V.*(Zo-L.*sqrt(r)))./(2.*sqrt(r));

    elseif tt== 2
        LL = Zo^2;
        f1 = @(r) bessellk(0,sqrt(r+x^2)/L).*exp(V*(Zo-sqrt(r))).*(Zo-
sqrt(r))./(2*L.*sqrt(r));

    else
        LL = Zo;
        f1 = @(r) bessellk(0,sqrt(r.^2+x^2)/L).*exp(V*(Zo-r)).*(Zo-
r)./(L);
    end

    %   acc1=10;
    %   ww=10;
    %   stop = min(LL*acc1,ww);
    %   c = 500;
    %
    %
    %   i=1;
    %   while LL<=stop;
    %       inc = log(1+(i)/c)^4;
```

```

%           int1 = int1 +
quadgk(f1,LL,LL+inc,'RelTol',a,'AbsTol',b,'MaxIntervalCount',9999999);
%
%
%           i=i+1;
%           LL=LL+inc;
%       end

UpV(n)= int1 +
quadgk(f1,LL,Inf,'RelTol',a,'AbsTol',b,'MaxIntervalCount',9999999);

%%

end
UpV=UpV*A;

end
-----

```

polyEstimate.m

```
function [ phistep ] = polyEstimate( pvec, LMA,xvec,dvec ,a,b1)

% uses the elements of 'stepvec' to determine the best stepsize in the
% direction of 'LMA' for pvec.

% returns the estimated stepsize

% stepvec = [1e-5 1e-5+.05 1e-5+.1 ];
%
% ercheck=zeros(1,length(stepvec));
%
% for j=1:length(stepvec)
%     Pcheck=[pvec(1)+LMA(1)*stepvec(j)*pvec(1)
pvec(2)+LMA(2)*stepvec(j)*pvec(2) pvec(3)
pvec(4)+LMA(3)*stepvec(j)*pvec(4)];
%     Ucheck=Ueval_v8(Pcheck(1),Pcheck(2),Pcheck(3),Pcheck(4),xvec);
%
%     ercheck(j)=(dvec-Ucheck)*(dvec-Ucheck)';
% end
% phistep=errorfit3(stepvec,ercheck);
% end

a=min(a*100,.08);
%b=-7;
b=-b1;
stepvec = [10^b 3*10^b a/6 a/4 a/3 a];

%stepvec = [10^b (10^b)*1.845 max((a/219),(10^b)*2.5743)
max((a/111),(10^b)*2.8) max((a/10),(10^b)*3.9) max((a),(10^b)*5)];
%stepvec = [10^b 10^b+a 10^b+(a*2) 10^b+(a*3) ];

ercheck=zeros(1,length(stepvec));

for j=1:length(stepvec)
    Pcheck=[pvec(1)+LMA(1)*stepvec(j)*pvec(1)
pvec(2)+LMA(2)*stepvec(j)*pvec(2) pvec(3)
pvec(4)+LMA(3)*stepvec(j)*pvec(4)];
    Ucheck=Ueval_v8(Pcheck(1),Pcheck(2),Pcheck(3),Pcheck(4),xvec);

    ercheck(j)=(dvec-Ucheck)*(dvec-Ucheck)';
end
phistep=errorfit(stepvec,ercheck,b);
end
```

errorfit.m

```
function [t] = errorfit( a,f,b )
n1 = length(f);

S = zeros(n1,n1);
S(:,1)=f;
for i = 2:n1
    for j = 2:i
        S(i,j)=(S(i,j-1)-S(i-1,j-1))/(a(i)-a(i-j+1));
    end
end

f1 =@(x) S(1,1) +(x-a(1)).*S(2,2)+(x-a(1)).*(x-a(2)).*S(3,3)+...
        (x-a(1)).*(x-a(2)).*(x-a(3)).*S(4,4)+(x-a(1)).*(x-
a(2)).*(x-a(3)).*(x-a(4)).*S(5,5);

        x=min(a)/10^b:max(a)/10^b;
        x=x*10^b;
%         plot(x,f1(x))
t=x(find(f1(x)==min(f1(x)),1,'first'));

end
```

ConvergeCheck.m

```
function [ converge ] = ConvergeCheck( M,cc )

% This function uses matrix M and convergence criteria 'c' to determine
if
% the new pvec paramters are with in tolerance for convergence

% 'd' is used to set the previous itterations for checking note that a
% value of 7 will check the rows 7-9 against the 10th row or in other
% words the previous three iterations

d=7;
converge =0;

if abs(max(M(d:9,2))-M(10,2))<=M(10,2)*cc
    if abs(max(M(d:9,3))-M(10,3))<=M(10,3)*cc
        if abs(max(M(d:9,4))-M(10,4))<=M(10,4)*cc
            if abs(min(M(d:9,2))-M(10,2))<=M(10,2)*cc
                if abs(min(M(d:9,3))-M(10,3))<=M(10,3)*cc
                    if abs(min(M(d:9,4))-M(10,4))<=M(10,4)*cc

                        converge = 1;

                    end
                end
            end
        end
    end
end

end

end
```

fitPlot.m

```
function [ uest ] = fitPlot( L, V ,Zo ,A ,xvec,dvec, filenamesave )
%UNTITLED2 Summary of this function goes here
% Detailed explanation goes here

acc=0;

uest=Ueval_v8(L,V,Zo,A,xvec);
evec = (uest-dvec);
phi  = evec*evec';

figure(20)
subplot(2,1,1)
plot(xvec,dvec,'o',xvec,uest,'MarkerSize',5)

legend('data','model')
title(strcat(filenamesave,' , 1st dp:',num2str(xvec(1)),'microns , last
dp:',num2str(xvec(length(xvec))), 'microns'), 'FontSize',15);
xlabel('position (microns)', 'FontSize',13)
ylabel('Intensity (a. u.)', 'FontSize',13)
d = max(uest);
c= min(uest);
text(xvec(floor(length(xvec)/2)), (c+(d-c)*9/10), [' L = '
,num2str(round(L*1e2)*1e-2), ' microns'], 'FontSize',15);
text(xvec(floor(length(xvec)/2)), (c+(d-c)*7/10), [' S/D = '
,num2str(round((V*100))/100), '/micron'], 'FontSize',15);
text(xvec(floor(length(xvec)/2)), (c+(d-c)*5/10), [' Zo = '
,num2str(round(Zo*1e2)*1e-2), ' microns'], 'FontSize',15);
text(xvec(floor(length(xvec)/2)), (c+(d-c)*3/10), [' Amplitude = '
,num2str(round(A*1e4)*1e-4)], 'FontSize',15);
text(xvec(floor(length(xvec)/6)), (c+(d-c)*9/10), [' phi = '
,num2str(round(phi*1e7)/1e3), '1e-4'], 'FontSize',15)

subplot(2,1,2)
semilogy(xvec,dvec,'o',xvec,uest,'MarkerSize',5)
legend('data','model')
xlabel('position (microns)', 'FontSize',13)
ylabel('Intensity (a. u.)', 'FontSize',13)
saveas(gcf,strcat(filenamesave,'.jpg'))
end
```

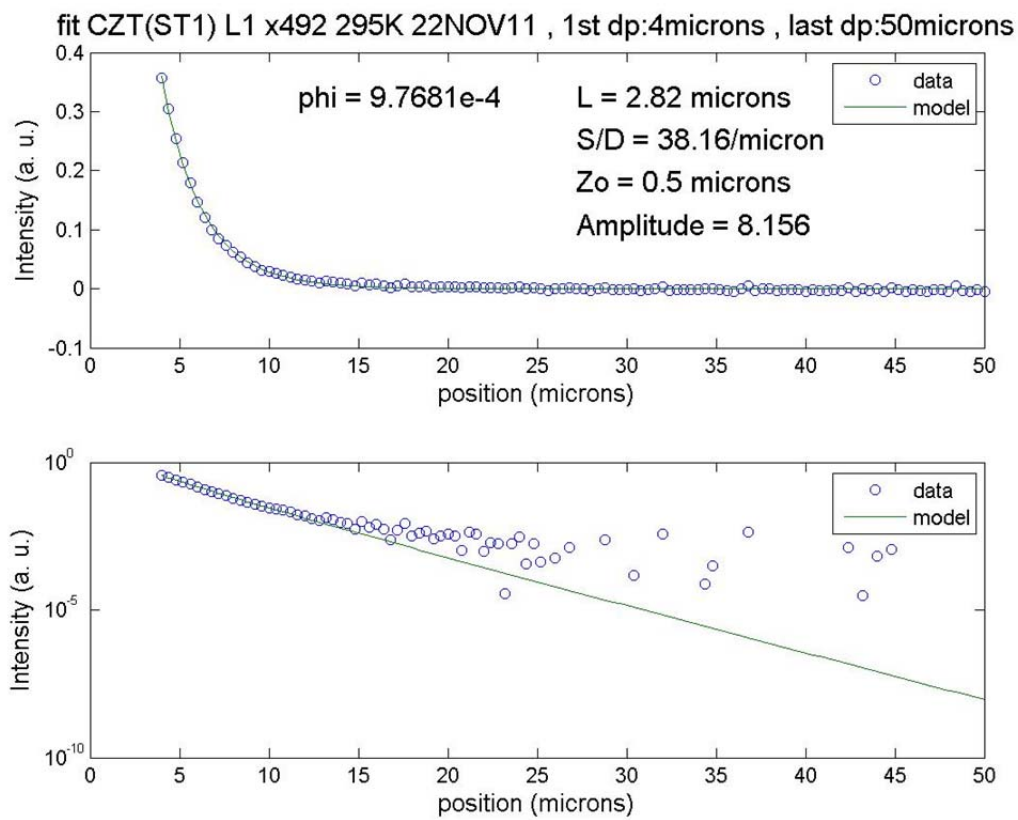


Figure C2. Mathematical fit.

APPENDIX D. SPATIAL DISTRIBUTION

This appendix explains how to create an intensity distribution plot, divide the distribution into desired lengths (i.e., 5 pixel or 2 μm segments) and fit the model to the data for each segment.

Begin by loading and analyzing each image file. Use **Loaddata_multicut.m**. Enter the line image file names in the “File Information” section of **Loaddata_multicut.m**. The number of pixels used is controlled by changing the value of the variable p in the file **finecut.m**.

The call structure is as follows:

```
Loaddata_multicut.m
    Tiff2data4fit_multicut.m
        CenterCut_v2.m
        Norm4fit.m
        finecut.m
        makeX.m
```

The result is a matlab file (.mat) with the filename “dataMC...”

To fit the data, use **fit_LMA_LVA_v1_multicut.m**. This file loads the “dataMC...” file, fits each distribution, and creates a file containing all the fitted diffusion lengths. This file is called “**fit...L data.m**”.

The call structure is as follows.

```
fit_LMA_LVA_v1_multicut.m
    LMA_LVA_v1.m
        Ueval_v8.m
        UpartL_v7.m
        UpartV_v8.m
        polyEstimate.m
            Ueval_v8.m
            errorfit.m
            fitplot.m
        ConvergeCheck.m
    fitPlot.m
```

To plot the diffusion length for each segment, use the file **plot_Ld.m**. Enter the file **fit...L data.m** in the “File Information” section. The file **plot_Ld.m** calls **mu_tau.m**. The resulting plots are shown in Figures D1 and D2.

Loaddata_multicut.m

```
-----
clc
clear
clf reset

%% File Information

fileload = {...
    1, 'ST1_line1_180s_500x_6E-10A_10kV_8.12mm_295K_x492.png',
    'CZT(ST1)', 'L1', 'x492', '295K', '22NOV11';
    2, 'ST1_line1_180s_500x_6E-10A_10kV_8.12mm_295K_x391.png',
    'CZT(ST1)', 'L1', 'x391', '295K', '22NOV11';
    3, 'ST1_line1_180s_500x_6E-10A_10kV_8.12mm_295K_x732.png',
    'CZT(ST1)', 'L1', 'x732', '295K', '22NOV11';
    4, 'ST1_line2_180s_500x_6E-10A_10kV_8.15mm_295K_x322.png',
    'CZT(ST1)', 'L2', 'x322', '295K', '22NOV11';
    5, 'ST1_line2_180s_500x_6E-10A_10kV_8.15mm_295K_x199.png',
    'CZT(ST1)', 'L2', 'x199', '295K', '22NOV11'};

k = size(fileload,1);

for j=1:k
    index{j}=fileload{j,1};
    imagefile{j}=fileload{j,2};
    sample{j}=fileload{j,3};
    location{j}=fileload{j,4};
    line{j}=fileload{j,5};
    temp{j}=fileload{j,6};
    date{j}=fileload{j,7};
    datafile{j}=(['dataMC ' sample{j} ' ' location{j} ' ' line{j} ' '
temp{j} ' ' date{j}]);
end

%% Select file and analyze data

j=1;
[ DataVecMC X IO R ] = Tiff2data4fit_multicut(imagefile{j}, sample{j});
save(datafile{j},'DataVecMC','X','IO','R')
-----
```

Tiff2data4fit_multicut.m

```
function [ DataVecMC X IO R ] = Tiff2data4fit_multicut( imagefile,
sample )

IO = imread(imagefile);
IO = double(IO); % [X Width 2184, Y Height 1472] in MicroCCD
IO = IO';

%% Surface plot of data
figure1 = figure(1);
clf('reset');
axes1 = axes('Parent',figure1,'CLim',[0 1]);
view(axes1,[0 0]);
grid(axes1,'minor');
hold(axes1,'all');
surf1(IO)
shading interp
colormap copper
title(sample)
xlabel('row','VerticalAlignment','cap','HorizontalAlignment','center');
ylabel('column','Visible','off','HorizontalAlignment','center');

%% First cut of Data

% Rstart1 = 0;
% Rend1 = 500;

Rstart1 = input('\nInput start range for desired Row data (1st cut): ');
Rend1 = input('Input end range for desired Row data (1st cut): ');

for I = 1:Rend1-Rstart1+1
    T1(:,I) = IO(:,I+Rstart1);
end
IO = T1;

% Surface plot of data
clf('reset');
figure1 = figure(1);
axes1 = axes('Parent',figure1,'CLim',[0 1]);
view(axes1,[0 0]);
grid(axes1,'minor');
hold(axes1,'all');
surf1(IO)
shading interp
colormap copper
title(sample)
xlabel('row','VerticalAlignment','cap','HorizontalAlignment','center');
ylabel('column','Visible','off','HorizontalAlignment','center');

%% Second cut of data
Rstart2 = input('\nInput start range for desired Row data (2nd cut): ');
```

```

Rend2 = input('Input end range for desired Row data (2nd cut): ');

R=[Rstart1 Rend1 Rstart2 Rend2];

for I = 1:Rend2-Rstart2+1
    T2(:,I) = IO(:,I+Rstart2);
end
IO = T2;

% Surface plot of data
clf('reset');
figure1 = figure(1);
axes1 = axes('Parent',figure1,'CLim',[0 1]);
view(axes1,[89 15]);
grid(axes1,'minor');
hold(axes1,'all');
surf1(IO)
shading interp
colormap copper
title(sample)
xlabel('row','VerticalAlignment','cap','HorizontalAlignment','center');
ylabel('column','Visible','off','HorizontalAlignment','center');

%% Centering

Xmax = input('\nEnter the number of pixels to the right of the peak to
keep: ');
% Xmax = 1000;

[IO] = CenterCut_v2(IO,Xmax);

clf('reset');
figure1 = figure(1);
axes1 = axes('Parent',figure1,'CLim',[0 1]);
view(axes1,[0 0]);
grid(axes1,'minor');
hold(axes1,'all');
surf1(IO)
shading interp
colormap copper
title(sample)
xlabel('row','VerticalAlignment','cap','HorizontalAlignment','center');
ylabel('column','Visible','off','HorizontalAlignment','center');

pause

%% Setting max value to 1
IO = Norm4fit(IO);

clf('reset');
figure1 = figure(1);
axes1 = axes('Parent',figure1,'CLim',[0 1]);
view(axes1,[0 0]);

```

```

grid(axes1,'minor');
hold(axes1,'all');
surfl(IO)
shading interp
colormap copper
title(sample)
xlabel('row','VerticalAlignment','cap','HorizontalAlignment','center');
ylabel('column','Visible','off','HorizontalAlignment','center');

%% Average over 2 um

[DataVecMC]=finecut(IO);
DataVecMC=DataVecMC';

%% Create X vector

[X] = makeX(DataVecMC);

%% Creat X vector

% [X]=fineX(B);

%% Benediction
display(' ')
display('Goodbye!')
display(' ')

```

CenterCut_v2.m

```
function [ BB ] = CenterCut_v2( AA , Xmax)

% This will cut the matrix AA so that the columns will be of length
Xmax
% Position 1 of the AA matrix is the max value of that column

[M,N]= size(AA);

DV = mean(AA');
n1 = max(DV);
n2 = find((DV) == n1,1,'first');

for I = 1:N
    n3 = find(AA(:,I) == max(AA(n2-20:n2+20,I)),1,'last');
    BB(:,I) = AA(n3:n3+Xmax-1,I);
end

end
```

Norm4fit.m

```
function [ BB ] = Norm4fit( AA )

% For each row in AA, a background noise level is calculated by taking
a
% mean of the furthest 20 value counts away from the source and then
% subtracting this background noise level from each value in that row

% The rows are then normalized to a max value of '1'

[M,N] = size(AA);

for I = M-19:M
    n1(I-M+20) = mean(AA(I,1:N));
end
AA = AA-mean(n1);

for I=1:N
    n2=AA(1,I);
    BB(:,I)= AA(:,I)./(n2);
end

end
```

finecut.m

```
function [ B ] = finecut( IO )
% This function cuts averages the columns of the IO matrix in sets of
% 5 columns. Since each column represents 0.4 microns, this averages
% the data over 2 microns.

p=5; % pixel set size

[m,n] = size(IO);

B=zeros(m,n/p);

for i=1:m
    for k=1:n/p
        A(k)=mean(IO(i,(k-1)*p+1:p*k));
        B(i,k) = A(k);
    end
end

end
```

makeX.m

```
function [ X ] = makeX( DataVec )

% creates the X vector of same length as DataVec with .4 as stepsizes

% N - length of DataVec

[M,N] = size(DataVec);

[M,N] = size(DataVec);
X=0:N-1;
X = X*(.4e-6);

end
```

fit_LMA_LVA_v1_multicut.m

```
format short e
format compact

clc
clear

%% File Information

fileload = {...
    1, 'ST1_line1_180s_500x_6E-10A_10kV_8.12mm_295K_x492.png',
    'CZT(ST1)', 'L1', 'x492', '295K', '22NOV11';
    2, 'ST1_line1_180s_500x_6E-10A_10kV_8.12mm_295K_x391.png',
    'CZT(ST1)', 'L1', 'x391', '295K', '22NOV11';
    3, 'ST1_line1_180s_500x_6E-10A_10kV_8.12mm_295K_x732.png',
    'CZT(ST1)', 'L1', 'x732', '295K', '22NOV11';
    4, 'ST1_line2_180s_500x_6E-10A_10kV_8.15mm_295K_x322.png',
    'CZT(ST1)', 'L2', 'x322', '295K', '22NOV11';
    5, 'ST1_line2_180s_500x_6E-10A_10kV_8.15mm_295K_x199.png',
    'CZT(ST1)', 'L2', 'x199', '295K', '22NOV11'};

k = size(fileload,1);

for j=1:k
    index{j}=fileload{j,1};
    imagefile{j}=fileload{j,2};
    sample{j}=fileload{j,3};
    location{j}=fileload{j,4};
    line{j}=fileload{j,5};
    temp{j}=fileload{j,6};
    date{j}=fileload{j,7};
    datafile{j}=(['dataMC ' sample{j} ' ' location{j} ' ' line{j} ' '
temp{j} ' ' date{j}]);
end

%% Select file and analyze data

j=1;
file_name_2_load = datafile{j};
file = load(file_name_2_load);

%% INITIAL PARAMETERS
% initial inputs for parameters are to be entered for pvec_start vector

L = 10; % enter L in microns
V = 8; % enter V in 1/micron
Zo = 0.5; % enter Zo in microns
A = 40;

first_data_point_2_use = 11;
number_of_data_points_2_use = 115; % (11-40=4-20 um) (11-115=4-40 um)
```

```

pvec = [L V Zo A];
initial_pvec = pvec;

%%

n=20; % Must match the number of rows in the DataVecMC vector

for k=1:n

    Xvec = file.X*1e6;
    DataVec(k,:) = file.DataVecMC(k,:);
    Dvec = DataVec(k,:);

    cc=1e-5;

    xvec = Xvec(first_data_point_2_use:first_data_point_2_use+
number_of_data_points_2_use);
    dvec = Dvec(first_data_point_2_use:first_data_point_2_use+
number_of_data_points_2_use);

    display(' ');
    display('Start - new loop');
    display('----- ');
    jj=1;

    [ L V A phi]=LMA_LVA_v1(pvec(1),pvec(2),pvec(3),pvec(4), xvec,
dvec,cc );
    pvec(1)=L;
    pvec(2)=V;
    pvec(3)=Zo;
    pvec(4)=A;

    Lvec(k)=L;
    Yvec(k)=2*k-1;
    Diffvec(k,1) = Yvec(k);
    Diffvec(k,2) = Lvec(k);

    filename_4_save = ([ 'fit ' sample{jj} ' ' location{jj} ' ' temp{jj} '
' date{jj} ' cut ' num2str(k)]);

    fitPlot( pvec(1), pvec(2), pvec(3), pvec(4), xvec, dvec,
filename_4_save );

    save(filename_4_save,'pvec','first_data_point_2_use','number_of_data_po
ints_2_use','initial_pvec')

    display('Goodbye')

end

```

```
    save(['fit L data ' sample{j} ' ' location{j} ' ' temp{j} ' '
date{j}'], 'Diffvec')
```

LMA_LVA_v1.m

```
function [ L V A phi b] = LMA_LVA_v1(L,V ,Zo,A ,xvec, dvec, cc)
pvec=[L V Zo A];

format long e
% pvec - parameter vector [ L V Zo A]
% M - matrix of most recent 10 parameters [phi ; L ; V ; Zo ; A]
% phi - squarred error vector (evec.*evec)
% evec - error vector

% Dvec - vector of with all data points recorded
% dvec - vector in use for fitting of current data set

% Xvec - position vector of all the x-values
% xvec - position vector in use for fitting current data set

% Uest - Full length vector of fitted values with current parameters
% uest - vector of fitted values cut to desird length

% UpL - vector of partial derrivatives with respect to L
% UpV - wrt V
% UpZ - wrt Z
% UpA - wrt A

% Ln - normalized vector of partial derrivatives with respect to L
% Vn - wrt V
% Zn - wrt Z
% An - wrt A
% En - normalized error vector

% grad - gradient vector with the four paramter
% Ngrad - normalized gradient vector

% dp2skip - # of data points moving away from the source to skip
% dp2use - # of data points to be used in the fitting of the model

% M - Matrix that contains the last 10 values throught the iteration
% process for [phi pvec(1) pvec(2) pvec(3) pvec(4) phistep ]
% cc - is the percentage of change in each paramter of pvec allowed to
% determine convergence

% gM - AMatrix of 4 columes consiting of the normalized partials
derivatives
% for UpL,UpV,UpZ,UpA

% LMA - Levenberg-Marquardt-Algorithm step direction

% stepvec - vector used to gage a the best next step between the max
and
% min of the step vector
% stepVecVariance - the amount that will be used in varying phistep (as
a
```

```

%               percentage) when creating the next 'stepvec'
% stepvec_start - used to keep track of the initial stepvec so that if
%               max(stepvec) is greater than '1' stepvec will be
reset
%               to 'stepvec_start'

jj=0;
converge=0;
M = zeros(10,6);
tic

phistep = .9;
stop=7;
cc=1e-6;
see =5 ;
lambda = 1e0;
nu = 3;
phi=0;

while converge ==0;

    jj=jj+1;
    uest = Ueval_v8(pvec(1),pvec(2),pvec(3),pvec(4),xvec);
    UpL = UpartL_v7(pvec(1),pvec(2),pvec(3),pvec(4), xvec);
    UpV = UpartV_v8(pvec(1),pvec(2),pvec(3),pvec(4), xvec);
    UpA = uest/pvec(4);

    evec = (uest-dvec);
    Aphi = evec*evec';
    % a1 = [UpL ; UpV ; UpA ]';
    a1 = [UpL/norm(UpL) ; UpV/norm(UpV); UpA/norm(UpA)]';
    b = -(a1'*a1+lambda*diag(diag(a1'*a1)))\'(a1'*evec');
    LMA = b'/norm(b);

    Bpvec = [pvec(1)+LMA(1)*phistep*pvec(1)
    pvec(2)+LMA(2)*phistep*pvec(2) pvec(3) pvec(4)+LMA(3)*phistep*pvec(4)];
    Buest = Ueval_v8(Bpvec(1),Bpvec(2),Bpvec(3),Bpvec(4),xvec);
    Bevec = Buest-dvec;
    Bphi = Bevec*Bevec';
    phistepL=phistep;
    k=0;
    if Bphi<Aphi
        if lambda <1e-10
            Aphi=Bphi;
        end
        while Bphi<Aphi
            k=k+1;
            Aphi = Bphi;
            Blambda=lambda/(nu^k);
            b = -(a1'*a1+Blambda*diag(diag(a1'*a1)))\'(a1'*evec');
            LMA = b'/norm(b);
            phistep = polyEstimate( pvec, LMA,xvec,dvec,phistepL,stop
);

```

```

        Bpvec = [pvec(1)+LMA(1)*phistep*pvec(1)
pvec(2)+LMA(2)*phistep*pvec(2) pvec(3) pvec(4)+LMA(3)*phistep*pvec(4)];
        Buest = Ueval_v8(Bpvec(1),Bpvec(2),Bpvec(3),Bpvec(4),xvec);
        Bevec = Buest-dvec;
        Bphi = Bevec*Bevec';
        if Blambda <1e-10
            Aphi=Bphi;
        end
    end
    k=k-1;
else
    Clambda=lambda/(nu);
    b = -(a1'*a1+Clambda*diag(diag(a1'*a1)))\'(a1'*evec');
    LMA = b'/norm(b);
    phistep = polyEstimate( pvec, LMA,xvec,dvec,phistepL ,stop );
    Cpvec = [pvec(1)+LMA(1)*phistep*pvec(1)
pvec(2)+LMA(2)*phistep*pvec(2) pvec(3) pvec(4)+LMA(3)*phistep*pvec(4)];
    Cuest = Ueval_v8(Cpvec(1),Cpvec(2),Cpvec(3),Cpvec(4),xvec);
    Cevec = Cuest-dvec;
    Cphi = Cevec*Cevec';

    if Cphi<Aphi
        k=k+1;
        Bphi=Cphi;
        if lambda <1e-10
            Aphi=Bphi;
        end
        while Bphi<Aphi
            k=k+1;
            Aphi = Bphi;
            Blambda=lambda/(nu^k);
            b = -(a1'*a1+Blambda*diag(diag(a1'*a1)))\'(a1'*evec');
            LMA = b'/norm(b);
            phistep = polyEstimate( pvec, LMA,xvec,dvec,phistepL
,stop );
            Bpvec = [pvec(1)+LMA(1)*phistep*pvec(1)
pvec(2)+LMA(2)*phistep*pvec(2) pvec(3) pvec(4)+LMA(3)*phistep*pvec(4)];
            Buest =
Ueval_v8(Bpvec(1),Bpvec(2),Bpvec(3),Bpvec(4),xvec);
            Bevec = Buest-dvec;
            Bphi = Bevec*Bevec';
            if Blambda <1e-10
                Aphi=Bphi;
            end
        end
        k=k-1;
    else
        if lambda >1e10
            Aphi=Bphi;
        else
            k=k-1;
        end
        while Aphi<Bphi
            k=k-1;
            Bphi=min(Aphi,Bphi);

```



```

        Alambda=lambda/(nu^k);
        b = -(a1'*a1+Alambda*diag(diag(a1'*a1)))\'(a1'*evec');
        LMA = b'/norm(b);
        phistep = polyEstimate( pvec, LMA,xvec,dvec,phistepL
,stop );

        Apvec = [pvec(1)+LMA(1)*phistep*pvec(1)
pvec(2)+LMA(2)*phistep*pvec(2) pvec(3) pvec(4)+LMA(3)*phistep*pvec(4)];
        Auest =
Ueval_v8(Apvec(1),Apvec(2),Apvec(3),Apvec(4),xvec);
        Aever = Auest-dvec;
        Aphi = Aever*Aever';
        if Alambda >1e10
            Aphi=Bphi;
        end

    end

    Bpvec=Apvec;
    k=k+1;
end
end
lambda=lambda/(nu^k);
% a1 = [UpL/norm(UpL) ; UpV/norm(UpV); UpA/norm(UpA)]';
b = -(a1'*a1+lambda*diag(diag(a1'*a1)))\'(a1'*evec');
LMA = b'/norm(b);
phistep = polyEstimate( pvec, LMA,xvec,dvec,phistepL ,stop );

pvec = [pvec(1)+LMA(1)*phistep*pvec(1)
pvec(2)+LMA(2)*phistep*pvec(2) pvec(3) pvec(4)+LMA(3)*phistep*pvec(4)];
uest = Ueval_v8(Bpvec(1),Bpvec(2),Bpvec(3),Bpvec(4),xvec);
evec = uest-dvec;
phi = evec*evec';

M(1:9,1:6)=M(2:10,1:6);
M(10,:)=[phi pvec(1) pvec(2) pvec(3) pvec(4) phistep ];

converge = ConvergeCheck(M,cc);
%     if converge == 1
%         if stop <6
%             converge=0;
%             stop=stop+1;
%             cc=cc/5;
%             display(' ##### YAHOOOO
#####')
%             M = zeros(10,6);
%             M(10,:)=[phi pvec(1) pvec(2) pvec(3) pvec(4) phistep ];
%
%             Lname = 'L = ';
%             Vname = ', V = ';
%             Zname = ', Zo = ';
%             Aname = ', A = ';
%
%             p1 = 'step =';
%             p2 = ', phi =';

```

```

%           L1 = ',   LMA  = ';
%           lam = ',   time =';
%           lam1 = ',   jj count  =';
%           lam2 = ',   lambda =';
%           time1= toc;
%           fprintf('%s %1.4e %s %1.5e %s %1.4e %s %1.4e %s   %4.3f
%10s %4.3e  \n'...
%               ,Lname,pvec(1),Vname,pvec(2),Zname,pvec(3),
Aname,pvec(4), lam,time1,lam2,lambda')
%
%           fprintf('%s %1.10f %s %1.9e %s %3.3e %s %4.4e %4.4e %4.4e
\n \n \n'...
%               ,p1, phistep,p2, phi,lam1,jj, L1 , LMA(1) , LMA(2)
,LMA(3));
%           fitPlot( pvec(1), pvec(2) ,pvec(3),pvec(4)
,xvec,dvec,'test' );
%           pause(.01)
%
%
%           end
%       end

    if mod(jj,see)==1;
        Lname = 'L = ';
        Vname = ',   V = ';
        Zname = ',   Zo = ';
        Aname = ',   A = ';

        p1 = 'step =';
        p2 = ',   phi =';
        L1 = ',   LMA  = ';
        lam = ',   time =';
        lam1 = ',   jj count  =';
        lam2 = ',   lambda =';
        time1= toc;
        fprintf('%s %1.4e %s %1.5e %s %1.4e %s %1.4e %s   %4.3f %10s
%4.3e  \n'...
            ,Lname,pvec(1),Vname,pvec(2),Zname,pvec(3), Aname,pvec(4),
lam,time1,lam2,lambda')

        fprintf('%s %1.10f%s %1.9e %s %3.3e %s %4.4e %4.4e %4.4e  \n
\n \n'...
            ,p1, phistep,p2, phi,lam1,jj, L1 , LMA(1) , LMA(2)
,LMA(3));
        fitPlot( pvec(1), pvec(2) ,pvec(3),pvec(4) ,xvec,dvec,'test' );
        pause(.01)

    end

end

L = pvec(1);
V = pvec(2);
Zo = pvec(3);

```

```

A = pvec(4);

Lname = 'L = ';
Vname = ', V = ';
Zname = ', Zo = ';
Aname = ', A = ';

p1 = 'step =';
p2 = ', phi =';
L1 = ', LMA = ';
lam = ', time =';
lam1 = ', jj count =';
lam2 = ', lambda =';
time1= toc;
fprintf('%s %1.4e %s %1.5e %s %1.4e %s %1.4e %s %4.3f %10s %4.3e
\n'...
,Lname,pvec(1),Vname,pvec(2),Zname,pvec(3), Aname,pvec(4),
lam,time1,lam2,lambda')

fprintf('%s %1.10f %s %1.9e %s %3.3e %s %4.4e %4.4e %4.4e \n \n \n'...
,p1, phistep,p2, phi,lam1,jj, L1 , LMA(1) , LMA(2) ,LMA(3));

fitPlot( pvec(1), pvec(2) ,pvec(3),pvec(4) ,xvec,dvec,'test' );
pause(.01)

end

```

Ueval_v8.m

```
function [ Uest ] = Ueval_v8( L,V,Zo,A,xvec )
% evaluates U by the provided inputs
% this requires the evaluation of two integrals. 'f1' and 'f2'
% ef (easy function) is used to simplify f1 and f2

k = length(xvec);
U1 = zeros(1,k);
U2 = zeros(1,k);
U3 = zeros(1,k);

%%

parfor n=1:k
    a=1e-13;
    b=1e-13;

    x = xvec(n);
    %%
    LL= x/L;

    ef = @(t) sqrt( t.^2 - (x/L).^2 );
    f1 = @(t) bessellk(1,t).*ef(t);

    U1(n)=
quadgk(f1,LL,Inf, 'RelTol',a, 'AbsTol',b, 'MaxIntervalCount',9999999);

    %%

    % f3 = @(r) bessellk(0,sqrt(r+(x/L)^2)).*(exp(V*(Zo-L.*sqrt(r)))-
1)./(2.*sqrt(r));
    % LL=(Zo/L)^2;

    % f3 = @(r) bessellk(0,sqrt(r+x^2)/L).*( exp(V*(Zo-sqrt(r)))-1
)./(2*L.*sqrt(r));
    % LL=Zo^2;

    f3 = @(r) bessellk(0,sqrt(r.^2+x^2)/L).*( exp(V*(Zo-r))-1 )./L;
    LL=Zo;

    U3(n)=
quadgk(f3,LL,Inf, 'RelTol',a, 'AbsTol',b, 'MaxIntervalCount',9999999);

end

Uest=(U1+U3)*A;

end
```

UpartL_v7.m

```
function [ UpL ] = UpartL_v7( L,V,Zo,A,xvec )
% This function calculates the partial derrivative of
%   u(L,V,Z,A) with respect to L

% takes as inputs the value for each variable L,V,Z,A
%   and a vector of concerened x values

% sends as output a vector with the partial of u wrt L
%   evaluated at each of the x vaules in the xvec
%display('UparL')
%tic
k = length(xvec);
I1 = zeros(1,k);
I2 = zeros(1,k);
I3 = zeros(1,k);

a=1e-13;
b=1e-13;

parfor n=1:k
    x = xvec(n);
    LL= x/L;

    ef = @(t) sqrt( t.^2 - (x/L)^2 );
    f1 = @(t) bessellk(2,t).*ef(t).*(x^2/L^3)./t;

    I1(n)=
quadgk(f1,LL,Inf, 'RelTol',a, 'AbsTol',b, 'MaxIntervalCount',9999999);

%%

%       f2 = @(r) bessellk(0,sqrt(r+(x/L)^2)).*( (-
V*(r+(x/L)^2).exp(V*(Zo-L.*sqrt(r)))./(r) ) + ...
%       (1- exp(V*(Zo-L.*sqrt(r))) ).*x^2./(L^3*r.^(3/2)) )/2;
%       LL= (Zo/L)^2;

%       f2 = @(r) (1-exp(V.*(Zo-sqrt(r))))./(2*L^2.*sqrt(r)).*(
bessellk(1,sqrt(r+x^2)./L).*(sqrt(r+x^2)./L)-bessellk(0,sqrt(r+x^2)./L)
%       );
%       LL= Zo^2;

%       f2 = @(r) 1/(L^2)*(1-exp(V.*(Zo-
r))).*(bessellk(1,sqrt(r.^2+x^2)./(L)).*sqrt(r.^2+x^2)./(L)-
bessellk(0,sqrt(r.^2+x^2)./(L)));
    LL= Zo;
```

```
    I2(n)=  
quadgk(f2,LL,Inf,'RelTol',a,'AbsTol',b,'MaxIntervalCount',9999999);
```

```
end
```

```
UpL=(I1+I2)*A;
```

```
end
```

UpartV_v8.m

```
function [ UpV ] = UpartV_v8( L,V,Zo,A,xvec )
% This function calculates the partial derrivative of
%   u(L,V,Z,A) with respect to V

% takes as inputs the value for each variable L,V,Z,A
%   and a vector of concerened x values

% sends as output a vector with the partial of u wrt V
%   evaluated at each of the x vaules in the xvec
%display('UpartV')
%tic
k = length(xvec);
UpV = zeros(1,k);

%%

a=100*eps;
b=1e-23;

parfor n=1:k

    int1=0;
    x = xvec(n);

    tt = 3;

    if tt == 1
        LL = (Zo/L)^2;
        f1 = @(r) bessellk(0,sqrt(r+(x/L)^2)).*(Zo-
L.*sqrt(r)).*exp(V.*(Zo-L.*sqrt(r)))./(2.*sqrt(r));

    elseif tt== 2
        LL = Zo^2;
        f1 = @(r) bessellk(0,sqrt(r+x^2)/L).*exp(V*(Zo-sqrt(r))).*(Zo-
sqrt(r))./(2*L.*sqrt(r));

    else
        LL = Zo;
        f1 = @(r) bessellk(0,sqrt(r.^2+x^2)/L).*exp(V*(Zo-r)).*(Zo-
r)./(L);
    end

    %   acc1=10;
    %   ww=10;
    %   stop = min(LL*acc1,ww);
    %   c = 500;
    %
    %
    %   i=1;
    %   while LL<=stop;
    %       inc = log(1+(i)/c)^4;
```

```

%           int1 = int1 +
quadgk(f1,LL,LL+inc,'RelTol',a,'AbsTol',b,'MaxIntervalCount',9999999);
%
%
%           i=i+1;
%           LL=LL+inc;
%       end

UpV(n)= int1 +
quadgk(f1,LL,Inf,'RelTol',a,'AbsTol',b,'MaxIntervalCount',9999999);

%%

end
UpV=UpV*A;

end

```

polyEstimate.m

```
function [ phistep ] = polyEstimate( pvec, LMA,xvec,dvec ,a,b1)

% uses the elements of 'stepvec' to determine the best stepsize in the
% direction of 'LMA' for pvec.

% returns the estimated stepsize

% stepvec = [1e-5 1e-5+.05 1e-5+.1 ];
%
% ercheck=zeros(1,length(stepvec));
%
% for j=1:length(stepvec)
%     Pcheck=[pvec(1)+LMA(1)*stepvec(j)*pvec(1)
pvec(2)+LMA(2)*stepvec(j)*pvec(2) pvec(3)
pvec(4)+LMA(3)*stepvec(j)*pvec(4)];
%     Ucheck=Ueval_v8(Pcheck(1),Pcheck(2),Pcheck(3),Pcheck(4),xvec);
%
%     ercheck(j)=(dvec-Ucheck)*(dvec-Ucheck)';
% end
% phistep=errorfit3(stepvec,ercheck);
% end

a=min(a*100,.08);
%b=-7;
b=-b1;
stepvec = [10^b 3*10^b a/6 a/4 a/3 a];

%stepvec = [10^b (10^b)*1.845 max((a/219),(10^b)*2.5743)
max((a/111),(10^b)*2.8) max((a/10),(10^b)*3.9) max((a),(10^b)*5)];
%stepvec = [10^b 10^b+a 10^b+(a*2) 10^b+(a*3) ];

ercheck=zeros(1,length(stepvec));

for j=1:length(stepvec)
    Pcheck=[pvec(1)+LMA(1)*stepvec(j)*pvec(1)
pvec(2)+LMA(2)*stepvec(j)*pvec(2) pvec(3)
pvec(4)+LMA(3)*stepvec(j)*pvec(4)];
    Ucheck=Ueval_v8(Pcheck(1),Pcheck(2),Pcheck(3),Pcheck(4),xvec);

    ercheck(j)=(dvec-Ucheck)*(dvec-Ucheck)';
end
phistep=errorfit(stepvec,ercheck,b);
end
```

errorfit.m

```
function [t] = errorfit( a,f,b )
n1 = length(f);

S = zeros(n1,n1);
S(:,1)=f;
for i = 2:n1
    for j = 2:i
        S(i,j)=(S(i,j-1)-S(i-1,j-1))/(a(i)-a(i-j+1));
    end
end

f1 =@(x) S(1,1) +(x-a(1)).*S(2,2)+(x-a(1)).*(x-a(2)).*S(3,3)+...
        (x-a(1)).*(x-a(2)).*(x-a(3)).*S(4,4)+(x-a(1)).*(x-
a(2)).*(x-a(3)).*(x-a(4)).*S(5,5);

        x=min(a)/10^b:max(a)/10^b;
        x=x*10^b;
%         plot(x,f1(x))
t=x(find(f1(x)==min(f1(x)),1,'first'));

end
```

ConvergeCheck.m

```
function [ converge ] = ConvergeCheck( M,cc )

% This function uses matrix M and convergence criteria 'c' to determine
if
% the new pvec paramters are with in tolerance for convergence

% 'd' is used to set the previous itterations for checking note that a
% value of 7 will check the rows 7-9 against the 10th row or in other
% words the previous three iterations

d=7;
converge =0;

if abs(max(M(d:9,2))-M(10,2))<=M(10,2)*cc
    if abs(max(M(d:9,3))-M(10,3))<=M(10,3)*cc
        if abs(max(M(d:9,4))-M(10,4))<=M(10,4)*cc
            if abs(min(M(d:9,2))-M(10,2))<=M(10,2)*cc
                if abs(min(M(d:9,3))-M(10,3))<=M(10,3)*cc
                    if abs(min(M(d:9,4))-M(10,4))<=M(10,4)*cc

                        converge = 1;

                    end
                end
            end
        end
    end
end

end

end
```

fitPlot.m

```
function [ uest ] = fitPlot( L, V ,Zo ,A ,xvec,dvec, filenamesave )
%UNTITLED2 Summary of this function goes here
%   Detailed explanation goes here

acc=0;

uest=Ueval_v8(L,V,Zo,A,xvec);
evec = (uest-dvec);
phi  = evec*evec';

figure(20)
subplot(2,1,1)
plot(xvec,dvec,'o',xvec,uest,'MarkerSize',5)

legend('data','model')
title(strcat(filenamesave,' , 1st dp:',num2str(xvec(1)),'microns , last
dp:',num2str(xvec(length(xvec))), 'microns'),'FontSize',15);
xlabel('position (microns)','FontSize',13)
ylabel('Intensity (a. u.)','FontSize',13)
d = max(uest);
c= min(uest);
text(xvec(floor(length(xvec)/2)),(c+(d-c)*9/10),[' L = '
,num2str(round(L*1e2)*1e-2), ' microns'],'FontSize',15);
text(xvec(floor(length(xvec)/2)),(c+(d-c)*7/10),[' S/D = '
,num2str(round((V*100))/100), '/micron'],'FontSize',15);
text(xvec(floor(length(xvec)/2)),(c+(d-c)*5/10),[' Zo = '
,num2str(round(Zo*1e2)*1e-2), ' microns'],'FontSize',15);
text(xvec(floor(length(xvec)/2)),(c+(d-c)*3/10),[' Amplitude = '
,num2str(round(A*1e4)*1e-4)], 'FontSize',15);
text(xvec(floor(length(xvec)/6)),(c+(d-c)*9/10),[' phi = '
,num2str(round(phi*1e7)/1e3), '1e-4'],'FontSize',15)

subplot(2,1,2)
semilogy(xvec,dvec,'o',xvec,uest,'MarkerSize',5)
legend('data','model')
xlabel('position (microns)','FontSize',13)
ylabel('Intensity (a. u.)','FontSize',13)
saveas(gcf,strcat(filenamesave,'.jpg'))
end
```

plot_Ld.m

```
clc
clear
% format bank

%% Load Diffusion Length Data

load('fit L data CZT(ST1) L1 295K 22NOV11')
Y=Diffvec(:,1);
L=Diffvec(:,2);

k=size(L,1);

for j = 1:k
    MT(j) = mu_tau(L(j),5);
end;
MT=MT';

%% Plot Diffusion Length vs. Position

% Diffusion Length
figure(1); % Common Marker Types: o,+,*,.,s,d,p,h
plot(Y,L,':ob','MarkerSize',10,'MarkerEdgeColor','b','MarkerFaceColor','b');
xmin = 0; xmax = 40; xlim([xmin xmax])
ymin = 0; ymax = 10; ylim([ymin ymax])
xlabel('Position (\mum)','FontSize',20,'FontWeight','b')
ylabel('Diffusion Length (\mum)','FontSize',20,'FontWeight','b')
set(gca,'XTick',0:2:40)
set(gca,'Xgrid','on');
set(gca,'Ygrid','on');
set(gca,'FontSize',16,'FontWeight','b');
legend('CZT(ST1)')
fitsave = ([ 'plot L' ]);
saveas(gcf, [fitsave '.jpg']);

% Mobility-Lifetime Product
figure(2); % Common Marker Types: o,+,*,.,s,d,p,h
plot(Y,MT,':or','MarkerSize',10,'MarkerEdgeColor','r','MarkerFaceColor','r');
xlabel('Position (\mum)','FontSize',20,'FontWeight','b')
ylabel('\mu\tau Product (cm^2/ V)','FontSize',20,'FontWeight','b')
set(gca,'XTick',0:2:40)
set(gca,'Xgrid','on');
set(gca,'Ygrid','on');
set(gca,'FontSize',16,'FontWeight','b');
legend('CZT(ST1)')
fitsave = ([ 'plot MT' ]);
saveas(gcf, [fitsave '.jpg']);

% figure(3)
```

```

% plotyy(Y,L,Y,MT)

% figure(4)
% [AX,H1,H2] = plotyy(Y,L,Y,MT,'plot');
% set(get(AX(1),'Ylabel'),'String','Diffusion Length
(\mum)','FontSize',20,'FontWeight','b')
% set(get(AX(2),'Ylabel'),'String','\mu\tau Product (cm^2/
V)','FontSize',20,'FontWeight','b')
% xlabel('Position (\mum)','FontSize',20,'FontWeight','b')
% set(AX(1),'XTick',0:2:40,'FontSize',16,'FontWeight','b')
% set(AX(2),'XTick',0:2:40,'FontSize',16,'FontWeight','b')
% % set(AX(1),'YTick',0:0.1:3,'FontSize',16,'FontWeight','b')
% % set(AX(2),'YTick',0:0.0004:0.0048,'FontSize',16,'FontWeight','b')
% % set(AX(1),'YLim',[1.6 2.4])
% % set(AX(2),'YLim',[5.2E-5 11.2E-5])
%
set(H1,'LineStyle',':', 'Marker','o', 'MarkerSize',8, 'MarkerEdgeColor','b
', 'MarkerFaceColor','b')
%
set(H2,'LineStyle',':', 'Marker','s', 'MarkerSize',8, 'MarkerEdgeColor','g
', 'MarkerFaceColor','g')
% set(gca,'Xgrid','on');
% fitsave = (['plotyy_example']);
% saveas(gcf, [fitsave '.jpg']);

```

mu_tau.m

```

function [ MT ] = mu_tau(L,T)
% The function mu-tau(L,T) calculates the mobility-lifetime product.
% It accepts the diffusion length L in um and temperature T in K as its
% arguments and passes back the mobility-lifetime product MT

k_boltzman = 8.617e-5; % eV/K

MT = (L^2/(k_boltzman*T))*1e-8;

end

```

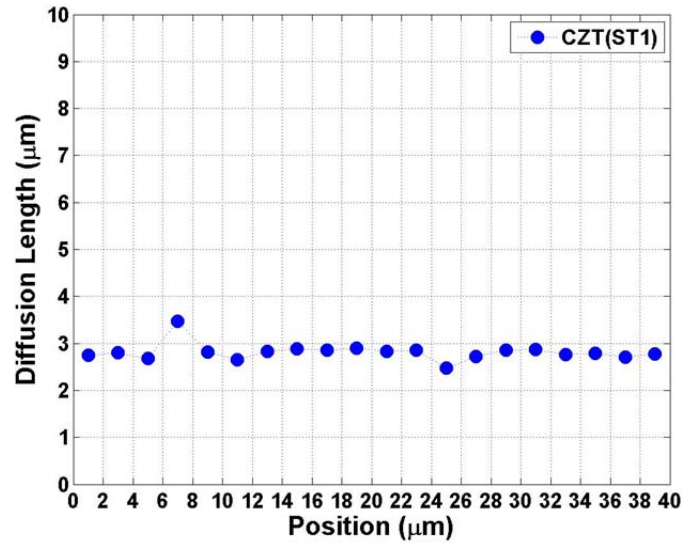


Figure D1. Plot of diffusion length as a function of position.

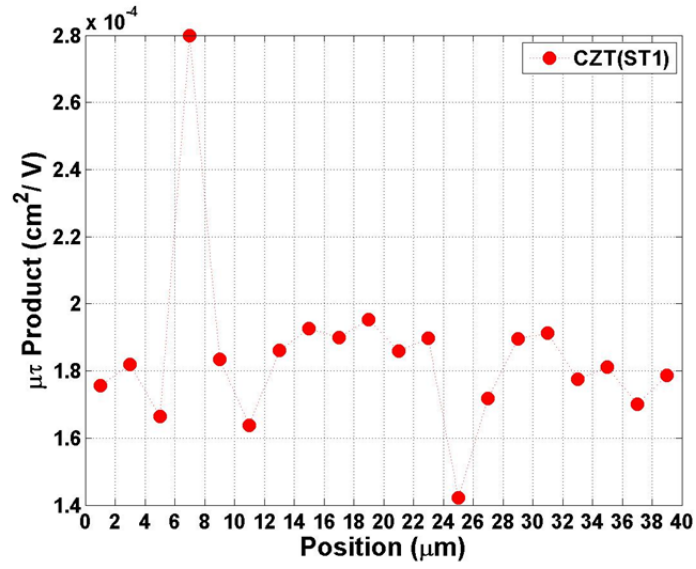


Figure D2. Plot of $\mu\tau$ product as a function of position.

THIS PAGE INTENTIONALLY LEFT BLANK

APPENDIX E. MONTE CARLO SIMULATIONS

Monte Carlo modeling was performed using CASINO v.2.4.8.1, with the following parameters:

Sample Definition: TlBr, 1×10^5 nm thickness, no substrate, density 7.56 g/cm^3

Microscope Setup: 20 keV beam, 1×10^5 electrons simulated, 50 nm beam radius

Distributions: Kanaya Okayama max range parameters, X Divisions: 250, Y Divisions: 250, Z Divisions: 250

Options: Default used

Change Physical Models: Defaults used

Once the simulation is complete, click on the “Export” button and save the data as a .dat file. The file may be opened with Notebook and saved in Excel.

The data may be analyzed in Matlab using the file **read_CASINO.m**. The file creates a 3x3x3 matrix, with the order of (z,x,y). There is a test tile, called **Test2_xyz.txt**, that may be run to understand how Matlab stores and displays the CASINO data. There is also an annotated version of Test2_xyz in Excel called **Test2_xyz.xlsx** that also shows how Matlab stores and displays the CASINO data.

To run the simulation, enter the filename in **read_CASINO.m** under the section “Load CASINO Energy Data.”

read_CASINO.m

```
-----
clc
clear

%% Load CASINO Energy Data

% Read XZ planes and build 3x3 CASINO matrix

% filename = 'Test2_xyz.txt';
% x = 5; y = 4; z = 6;
filename = 'TlBr_20keV_1E5nm_1E5H.dat';
x = 250; y = 250; z = 250;

CASINO = ones(z,x,y);

a = 11; % Row containing XZ Plane 0, where cell A1 = (0,0)

for n = 1:y
    RS = a+(2*n)+z*(n-1); RE = RS+(z-1);
    XZ = dlmread(filename, '\t', [RS,1,RE,x]);
    CASINO(:, :, n) = XZ;
```

```

        disp([num2str(n) '_done'])
    end

    % Sum through z-direction
    AA = ones(y,x);
    for j = 1:y
        XZ = CASINO(:, :, j);
        AA(j, :) = sum(XZ, 1);
    end

    % Find indices of maximum value in matrix
    [maxA, ind] = max(AA(:));
    [R, C] = ind2sub(size(AA), ind);

    % Normalize AA matrix
    M = max(max(AA));
    AA = AA/M;

    save([filename '.mat'])

    %% Load CASINO CL data
    %%
    %% filename2 = 'CL_by_R.dat';
    %%
    %% b = 2; % Row containing Radius = 0, where cell A1 = (0,0)
    %%
    %% Rstart = b; Rend = Rstart+(x-1);
    %%
    %% CL = dlmread(filename2, '\t', [Rstart, 0, Rend, 1]);
    %%
    %% radius_LR = CL(:, 1); % Creates column vector of position (radius)
    data
    %% radius_RL = -flipud(radius_LR); % Flips position vector
    %% radius = [radius_LR; radius_RL]; % Concatenates radius vectors
    %%
    %% offset = x/2;
    %% radius = radius+offset;
    %%
    %% intensity_LR = CL(:, 2); % Creates column vector of CL intensity data
    %% intensity_LR = intensity_LR/(max(intensity_LR)); % Normalizes CL
    intensity vector
    %% intensity_RL = flipud(intensity_LR); % Flips position vector
    %% intensity = [intensity_LR; intensity_RL]; % Concatenates radius
    vectors

    %% Plot data

    figure(1)
    X = -x/2:1:x/2-1;
    Y = -y/2:1:y/2-1;
    surf(X, Y, AA)
    % view([0 90]) % XY
    % view([0 0]) % XZ
    view([-37.5, 30]) % oblique

```

```

shading interp
xlabel('Position (nm)','FontSize',20,'FontWeight','b')
ylabel('Position (nm)','FontSize',20,'FontWeight','b')
zlabel('Energy Density (Arb. units)','FontSize',20,'FontWeight','b')
set(gca,'FontSize',16,'FontWeight','b')
% colorbar
xlim([-x/2 x/2]); ylim([-x/2 x/2])
% saveas(gca,'Planar.jpg')
saveas(gca,'Oblique.jpg')

%%

figure(2)
BB = AA(R,:);
X = -x/2:1:x/2-1;
% X = 1:1:x;
plot(X,BB,'-.b','MarkerSize',4)
legend('Energy Density')
xlim([min(X) max(X)])

% figure(3)
% plot(radius, intensity,'sk','MarkerSize',4)
% legend('CL Intensity (%)')
% xlim([0 300])

% figure(4)
% hold on
% plot(X,BB,'ob','MarkerSize',4); legend('Energy Density')
% plot(radius, intensity,'sk','MarkerSize',4); legend('CL Intensity (%)')
% xlim([0 300])

figure(5)
mesh(CASINO(:,:,R));
view([0,-90])
% xlim([35 65]); ylim([0 25])

figure(6)
contourf(CASINO(:,:,R),6);
view([0,-90])
xlim([100 200]); ylim([0 100])
% xlim([35 65]); ylim([0 25])

% figure(5)
% [C,h] = contour(CASINO(:,:,R),6);
% clabel(C,h)
% view([0,-90])
% xlim([100 200]); ylim([0 100])

%%

syms r

```

```

r = -x/2:1:x/2-1;
% r = 0:0.1:x;
r0 = 0;

% Lorentzian
g = 3;
L = g./((r-r0).^2+g^2);
Lmax = max(L);
L = L/Lmax;
% figure(5)
% plot(r,L,'r');
% legend('Lorentzian');

% Gaussian
a = 2;
G = exp(-((abs((r-r0)/a^2)).^2));
% figure(6)
% plot(r,G,'g');
% title('Gaussian');

% Comparison
figure(7)
hold on
plot(X,BB,'ob','MarkerSize',5,'LineWidth',2)
plot(r,G,'g','LineWidth',2);
plot(r,L,'r','LineWidth',2);
% plot(radius,intensity,'sk','MarkerSize',4)
xlabel('Position (nm)','FontSize',20,'FontWeight','b')
ylabel('Energy Density (Arb. units)')
set(gca,'FontSize',16,'FontWeight','b')
legend('Energy Density','Gaussian','Lorentzian')
% legend('Energy Density','Gaussian','Lorentzian','CL Intensity (%)')
xlim([-125 125])
hold off
saveas(gca,'Fit.jpg')

%%

% plane = 100;
%
% figure(1)
% surf(CASINO(:,:,plane));
% view([180,90])

% figure(2)
% contour(CASINO(:,:,plane));
% view([180,90])
%
% figure(3)
% [C,h] = contour(CASINO(:,:,plane),10);
% clabel(C,h)
% view([180,90])
%
% figure(4);

```

```
% offset = max(CASINO(:));
% hold on;
% for i = 1:50:y
%     surf(CASINO(:, :, i) + offset*(i-1))
% end
```

Two sample output graphs are shown below.

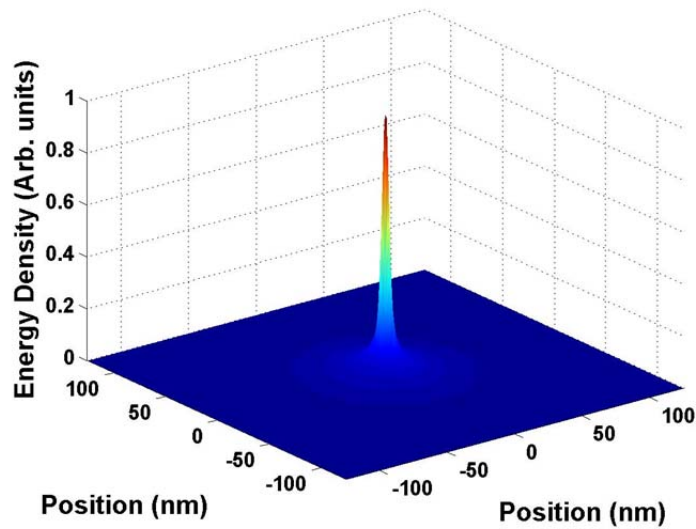


Figure E1. Oblique view.

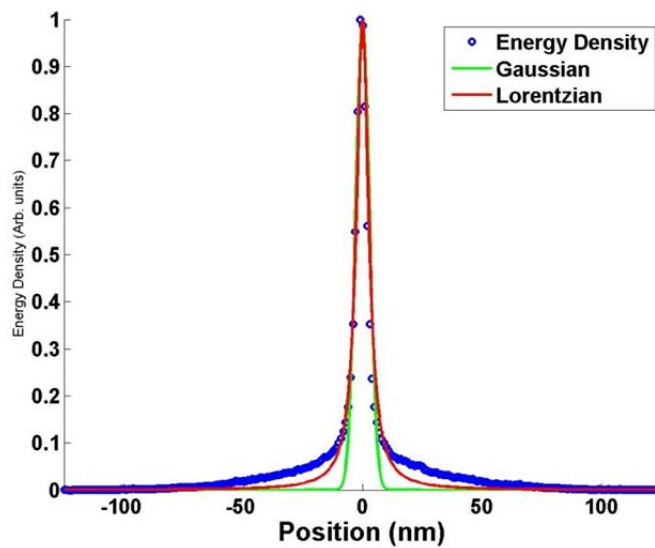


Figure E2. Side view with Gaussian and Lorentzian fits.

THIS PAGE INTENTIONALLY LEFT BLANK

LIST OF REFERENCES

- [1] CRS Report RL32595, “Nuclear terrorism: A brief review of threats and responses,” Updated 10FEB05, <http://www.dtic.mil/cgi-bin/GetTRDoc?Location=U2&doc=GetTRDoc.pdf&AD=ADA437865>, accessed 7FEB12.
- [2] IAEA Report GOV/2011/65, “Implementation of the NPT safeguards agreement and relevant provisions of security council resolutions in the Islamic Republic of Iran,” 8NOV11, <http://www.iaea.org/Publications/Documents/Board/2011/gov2011-65.pdf>, accessed 8FEB12.
- [3] UN Resolution 1696, “Security Council demands Iran suspend uranium enrichment by 31 August, or face possible economic, diplomatic sanctions,” <http://www.un.org/News/Press/docs/2006/sc8792.doc.htm>, 31JUL06, accessed 7FEB12.
- [4] BBC News, “Q&A: Iran nuclear issue,” <http://www.bbc.co.uk/news/world-middle-east-11709428>, 23JAN12, accessed 7FEB12.
- [5] U.S. national commission on terrorist attacks upon the United States, “Overview of the enemy, staff statement no. 15,” June 2004, <http://govinfo.library.unt.edu/911/hearings/hearing12.htm>, accessed 8FEB12.
- [6] IAEA Report GOV/2006/46-GC(50)/13, “Nuclear security – measures to protect against nuclear terrorism,” 16AUG2006, http://www.iaea.org/About/Policy/GC/GC50/GC50Documents/English/gc50-13_en.pdf, accessed 8FEB12.
- [7] D. Albright, K. Buehler, and H Higgins, “Bin Laden and the bomb,” *Bulletin of the Atomic Scientists*, January/February 2002, <http://www.isis-online.org/publications/terrorism/binladenandbomb.pdf>, accessed 8FEB12.
- [8] GAO Report 05-840T, “Combating nuclear smuggling – Efforts to deploy radiation detection equipment in the United States and other countries,” 21JUN05, <http://www.gao.gov/new.items/d05840t.pdf>, accessed 8FEB12.
- [9] CRS Report RL32839, “Border and transportation security: The complexity of the challenge,” 29MAR05, <http://www.fas.org/sgp/crs/homesec/RL32839.pdf>, accessed 21MAY12.
- [10] GAO Report 03-297T, “Container security – Current efforts to detect nuclear materials, new initiatives, and challenges,” 18NOV02, <http://www.gao.gov/new.items/d03297t.pdf>, accessed 8FEB12.

- [11] R. Vartabedian, “U.S. to install new nuclear detectors at ports,” *LA Times*, 15 July 2006, <http://articles.latimes.com/2006/jul/15/nation/na-radiation15>, accessed 21MAY12.
- [12] A. Glaser, “Detection of special nuclear materials,” Lecture, Princeton University, April 16, 2007, http://www.princeton.edu/~aglaser/lecture2007_detection.pdf, accessed 10 May 2012.
- [13] J. McDonald, B. Coursey, and M. Carter, “Detecting illicit radioactive sources,” *Physics Today*, pp. 36–41, November 2004.
- [14] Applied Research Associates, “Detecting the nuclear terrorist,” http://www.ara.com/Newsroom_Whatsnew/press_releases/pr_nuclear_terr.html, accessed 9FEB12.
- [15] J. P. Ahern, Testimony in “Hearings before the permanent subcommittee on investigations of the committee on homeland security and governmental affairs,” *Neutralizing the Nuclear and Radiological Threat: Securing the Global Supply Chain*, Senate Hearing 109-548, March 28 and 30, 2006, <http://www.gpo.gov/fdsys/pkg/CHRG-109shrg27754/html/CHRG-109shrg27754.htm>, accessed 22MAY12.
- [16] B.D. Milbrath, A. J. Peurrung, M. Bliss, and W. J. Weber, “Radiation detector materials: An overview,” *J. Mat. Res.*, vol. 23, no. 10, pp. 2561–2581, 2008.
- [17] P. N. Luke and M. Amman, “Room-temperature replacement for Ge detectors—Are we there yet?” *IEEE Trans. Nucl. Sci.*, vol. 54, no. 4, pp. 834–842, 2007.
- [18] T. E. Schlesinger and R. B. James, “Introduction and overview,” in *Semiconductors for Room Temperature Nuclear Detector Applications*, T. E. Schlesinger and R. B. James, Eds. New York: Academic Press, Inc., vol. 43, pp. 1–11, 1995.
- [19] V. Gerrish, “Characterization and quantification of detector performance,” in *Semiconductors for Room Temperature Nuclear Detector Applications*, T. E. Schlesinger and R. B. James, Eds. New York: Academic Press, vol. 43, pp. 493–530, 1995.
- [20] G. Knoll, *Radiation Detection and Measurement*. New York: John Wiley & Sons, 2000.
- [21] A. Owens and A. Peacock, “Compound semiconductor radiation detectors,” *Nucl. Instr. and Meth. A*, vol. 531, pp. 18–37, 2004.
- [22] A. Ruzin and Y. Memirovsky, “Methodology for evaluation of mobility-lifetime product by spectroscopy measurements in CdZnTe spectrometers,” *J. Appl. Phys.*, vol. 82, no. 9, pp. 4177–4171, 1997.

- [23] K. Hecht, "Zum mechanismus des lichtelektrischen primaerstromes in isolierenden kristallen," *Z. Phys.*, vol. 77, p. 235, 1932.
- [24] M. Amman, J. S. Lee, P. N. Luke, H. Chen, S. A. Awadalla, R. Redden, and G. Bindley, "Evaluation of THM-grown CdZnTe material for large-volume gamma-ray detector applications," *IEEE Trans. Nucl. Sci.*, vol. 56, no. 3, pp. 795–799, 2009.
- [25] A. G. Kozorezov, J. K. Wigmore, A. Owens, R. den Hartog, A. Peacock, and H. A. Al-Jawari, "Resolution degradation of semiconductor detectors due to carrier trapping," *Nucl. Instr. and Meth. A*, vol. 546, pp. 209–212, 2005.
- [26] M. Amman, J. S. Lee, P. N. Luke, "Electron trapping nonuniformity in high-pressure-Bridgeman-grown CdZnTe," *J. Appl. Phys.*, vol. 92, no. 6, pp. 3198–3206, 2002.
- [27] G. A. Carini, A. E. Bolotnikov, G. S. Camarda, and R. B. James, "High-resolution X-ray mapping of CdZnTe detectors," *Nucl. Instr. and Meth. A*, vol. 579, pp. 120–124, 2007.
- [28] A. Lohstroh, P. J. Sellin and A. Simon, "High-resolution mapping of the mobility-lifetime product in CdZnTe using a nuclear microprobe," *J. Phys. Condens. Matter*, vol. 16, pp. S67–S73, 2004.
- [29] G. Vízkelethy, B. A. Brunett, D. S. Walsh, R. B. James, R. W. Olsen, and B. L. Doyle, "Ion microbeam studies of cadmium zinc telluride radiation detectors by IBICC," *Nucl. Instr. And Meth. B*, vol. 158, pp. 437–444, 1999.
- [30] N. M. Haegel, J. D. Fabbri, and M. P. Coleman, "Direct transport imaging in planar structures," *Appl. Phys. Lett.*, vol. 84, no. 8, pp. 1329–1331, 2004.
- [31] Z. He, G. F. Knoll, and D. K. Wehe, "Direct measurement of product of the electron mobility and mean free drift time of CdZnTe semiconductors using position sensitive single polarity charge sensing detectors," *J. App. Phys.*, vol. 84, no. 10, pp. 5566–5569, 1998.
- [32] K. E. Blaine, "Contact free measurement of mobility-lifetime ($\mu\tau$) product using transport imaging," M.S. thesis, Naval Postgraduate School, 2011.
- [33] K. E. Blaine, D. J. Phillips, C. L. Frenzen, C. Scandrett, and N. M. Haegel, "Three-dimensional transport imaging for the spatially resolved determination of carrier diffusion length in bulk materials," *Rev. Sci. Instrum.*, vol. 83, pp. 043702-1–043702-7, 2012.
- [34] N. M. Haegel, S. E. Williams, C. L. Frenzen, and C. Scandrett, "Minority carrier lifetime variations associated with misfit dislocation networks in heteroepitaxial GaInP," *Semicond. Sci. Technol.*, vol. 23, no. 5, pp. 055017-1–055017-6, 2010.

- [35] N. M. Haegel, T. J. Mills, M. Talmadge, C. Scandrett, C. L. Frenzen, H. Yoon, C. M. Fetzter, and R. R. King, "Direct imaging of anisotropic minority-carrier diffusion in ordered GaInP," *J. Appl. Phys.*, vol. 105, pp. 023711-1–023711-5, 2009.
- [36] L. Baird, G. H. Ang, C. H. Low, N. M. Haegel, A. A. Talin, Q. Li, G. T. Wang, "Imaging minority carrier diffusion length in GaN nanowires using near field optical microscopy," *Physics B*, vol. 404, pp. 4933–4936, 2009.
- [37] H. J. Leamy, "Charge collection scanning electron microscopy," *J. Appl. Phys.*, vol. 53, no. 6, pp. R51–R80, 1982.
- [38] J. S. Blakemore, *Solid State Physics*. New York: Cambridge University Press, 1985.
- [39] M. Shorohov, M. Kouznetsov, I. Lisitskiy, V. Ivanov, V. Gostilo, and A. Owens, "Recent results in TlBr detector crystal performance," *IEEE Trans. Nucl. Sci.*, vol. 56, no. 4, pp. 1855–1858, 2009.
- [40] H. Kim, A. Churilov, G. Ciampi, L. Cirignano, W. Higgins, S. Kim, P. O. Dougherty, F. Olschner, and K. Shah, "Continued development of thallium bromide and related compounds for gamma-ray spectrometers," *Nucl. Instr. and Meth. A*, vol. 629, pp. 192–196, 2011.
- [41] K. Hitomi, T. Tada, S. Kim, Y. Wu, T. Tanaka, T. Shoji, H. Yamazaki, and K. Ishii, "Recent development of TlBr gamma-ray detectors," *IEEE Trans. Nucl. Sci.*, vol. 58, no. 4, pp. 1987–1991, 2011.
- [42] A. V. Churilov, W. M. Higgins, G. Ciampi, H. Kim, L. J. Cirignano, F. Olschner, and K. S. Shah, "Purification, crystal growth and detector performance of TlBr," *Proc. of SPIE*, vol. 7079, pp. 70790K-1–70790K-8, 2008.
- [43] K. Hitomi, M. Matsumoto, O. Muroi, T. Shoji, and Y. Hiratate, "Thallium bromide optical and radiation detectors for X- and gamma-ray spectroscopy," *IEEE Trans. Nucl. Sci.*, vol. 49, no. 5, pp. 2526–2529, 2002.
- [44] E. S. Elshazly, G. Tepper, A. Burger, "Charge trapping in detector grade thallium bromide and cadmium zinc telluride: Measurement and theory," *Nucl. Instr. and Meth. A*, vol. 620, pp. 279–284, 2010.
- [45] M. Du, "First-principles study of native defects in TlBr: Carrier trapping, compensation, and polarization phenomenon," *J. Appl. Phys.*, vol. 108, pp. 053506-1–053506-4, 2010.
- [46] M. Du, "First principles study of impurities in TlBr," *J. Appl. Phys.*, vol. 111, pp. 073519-1–073519-4, 2012.

- [47] M. Grundmann, *The Physics of Semiconductors*. New York: Springer, 2010.
- [48] T. E. Schlesinger, J. E. Toney, H. Yoon, E. Y. Lee, B. A. Brunett, L. Franks, and R. B. James, "Cadmium zinc telluride and its use as a nuclear radiation detector material," *Mat. Sci. and Eng.*, vol. 32, pp. 103–189, 2001.
- [49] M. Chu, S. Terterian, D. Ting, G. A. Carini, G. S. Camarda, A. E. Bolotnikov, R. B. James, D. Xu, and Z. He, "Effects of material improvement on CZT detectors," *Proc. Of SPIE*, vol. 6319, pp. 631905-1–631905-9, 2006.
- [50] C. Szeles, S. E. Cameron, J. Ndap, and W. Chalmers, "Advances in the crystal growth of semi-insulating CdZnTe for radiation detector applications," *IEEE Trans. Nucl. Sci.*, vol. 49, no. 5, pp. 2535–2540, 2002.
- [51] N. B. Smirnov, I. S. Lisitsky, M. S. Kuznetsov, A. V. Govorkov, E. A. Kozhukhova, "Electrophysical characteristics of TlBr crystal grown in various ambients," *IEEE Trans. Nucl. Sci. Symp. Conf. Rec.*, pp. 3700–3704, 2006.
- [52] K. Hayakawa, K. Hitomi, T. Shoji, and C. Onodera, "Photoluminescence analysis of TlBr crystals for radiation detector applications," *Conf. Rec. 2009 IEEE Nucl. Sci. Symp.*, pp. 1647–1648.
- [53] R. Shimizu, T. Koda, and T. Murahashi, "Exciton luminescence in TlBr and TlCl," *J. Phys. Soc. Jpn.*, vol. 36, pp. 161–168, 1974.
- [54] Evans Analytical Group (EAG), "Energy dispersive X-ray spectroscopy (EDS)," <http://www.eaglabs.com/mc/energy-dispersive-x-ray-spectroscopy.html>, accessed 14MAY12.
- [55] Evans Analytical Group (EAG), "Time-of-flight secondary ion mass spectrometry (TOF-SIMS)," <http://www.eaglabs.com/mc/time-of-flight-secondary-ion-mass-spectrometry.html>, accessed 2MAY12.
- [56] A. Owens, M. Bavdaz, G. Brammertz, V. Gostilo, H. Graafsma, A. Kozorezov, M. Krumrey, I. Lisjutin, A. Peacock, A. Puig, H. Sipila, and S. Zatoloka, "The X-ray response of TlBr," *Nucl. Instr. And Meth. A*, vol. 497, pp. 370–380, 2003.
- [57] T. Onodera, K. Hotomi, and T. Shoji, "Temperature dependence of spectroscopic performance of thallium bromide X- and gamma-ray detectors," *IEEE Trans. Nucl. Sci.*, vol. 54, no. 4, pp. 860–863, 2007.
- [58] A. V. Churilov, G. Ciampi, H. Kim, L. J. Cirignano, W. M. Higgins, F. Olschner, and K. Shah, "Thallium bromide nuclear radiation detector development," *IEEE Trans. Nucl. Sci.*, vol. 56, no. 4, pp. 1875–1881, 2009.

- [59] K. Hitomi, T. Onodera, and T. Shoji, "Influence of zone purification process on TlBr crystals for radiation detector fabrication," *Nucl. Instr. And Meth. A*, vol. 579, pp. 153–156, 2007.
- [60] D. J. Phillips, K. E. Blaine, L. J. Cirignano, G. Ciampi, and N. M. Haegel, "Cathodoluminescence and spatial variation in mobility-lifetime ($\mu\tau$) product in bulk doped thallium bromide," *IEEE Trans. Nucl. Sci.*, submitted.
- [61] H. M. Smith, D. J. Phillips, I. D. Sharp, J. W. Beeman, D. C. Chrzan, N. M. Haegel, E. E. Haller, G. Ciampi, H. Kim, and K. S. Shah, "Electronic effects of Se and Pb dopants in TlBr," *Appl. Phys. Lett.*, vol. 100, no. 20, pp. 202102-1–202102-4, 2012.
- [62] A. Castaldini, A. Cavallini, B. Fraboni, "Deep energy levels in CdTe and CdZnTe," *J. Appl. Phys.*, vol. 83, no. 4, pp. 2121–2126, 1998.
- [63] S. D. Sordo, L. Abbene, E. Carroll, A. M. Mancini, A. Zappettini, and P. Ubertini, "Progress in the development of CdTe and CdZnTe semiconductor radiation detectors for astrophysical and medical applications," *Sensors*, vol. 9, pp. 3491–3526, 2009.
- [64] H. Chen, S. A. Awadalla, J. Mackenzie, R. Redden, G. Bindley, A. E. Bolotnikov, G. S. Camarda, G. Carini, and R. B. James, "Characterization of travelling heater method (THM) grown Cd_{0.9}Zn_{0.1}Te crystals," *IEEE Trans. Nucl. Sci.*, vol. 54, no. 4, 2007.
- [65] T. Takahashi and S. Watanabe, "Recent progress in CdTe and CdZnTe detectors," *IEEE Trans. Nucl. Sci.*, vol. 48, no. 4, pp. 950–959, 2001.
- [66] P. J. Sellin, G. Prekas, J. Franc, and R. Grill, "Electric field distribution in CdZnTe due to reduced temperature and X-ray irradiation," *Appl. Phys. Lett.*, vol. 96, pp. 133509-1–133509-3, 2010.
- [67] G. Sato, T. Takahashi, M. Sugiho, M. Kouda, T. Mitani, K. Nakazawa, Y. Okada, and S. Watanabe, "Characterization of CdTe/CdZnTe detectors," *IEEE Trans. Nucl. Sci.*, vol. 49, no. 3, pp. 1258–1263, 2012.
- [68] A. E. Bolotnikov, N. M. Abdul-Jabbar, O. S. Babalola, G. S. Camarda, Y. Cui, A. M. Hossain, E. M. Jackson, H. C. Jackson, J. A. James, K. T. Kohman, A. L. Luryi, and R. B. James, "Effects of Te inclusions on the performance of CdZnTe radiation detectors," *IEEE Trans. Nucl. Sci.*, vol. 55, no. 5, pp. 2757–2764, 2008.
- [69] A. E. Bolotnikov, G. C. Camarda, G. W. Wright, and R. B. James, "Factors limiting the performance of CdZnTe detectors," *IEEE Trans. Nucl. Sci.*, vol. 52, no. 3, pp. 589–598, 2005.

- [70] E. Rzepka, A. Lusson, A. Riviere, A. Aoudia, Y. Marfaing, and R. Triboulet, "Defect study by photoluminescence and cathodoluminescence in vanadium doped CdZnTe," *J. Crys. Growth*, vol. 161, pp. 286–291, 1996.
- [71] J. Rodriguez-Fernandez, V. Carcelen, P. Hidalgo, N. Vihayan, J. Piqueras, N. V. Sochinskii, J. M. Perez, and E. Dieguez, "Relationship between the cathodoluminescence emission and resistivity in In doped CZT crystals," *J. Appl. Phys.*, vol. 106, pp. 044901-1–044901-3, 2009.
- [72] R. K. Ahrenkiel, D. J. Dunlavy, B. Keyes, S. M. Vernon, T. M. Dixon, S. P. Tobin, K. L. Miller, and R. E. Hayes, "Ultralong minority-carrier lifetime epitaxial GaAs by photon recycling," *Appl. Phys. Lett.*, vol. 55, no. 11, pp. 1088–1090, 1989.
- [73] R. Baba, R. Watanabe, K. Asano, F. Koyama, and K. Iga, "Theoretical and experimental estimations of photon recycling effect in light emitting devices with a metal mirror," *Jpn. J. Appl. Phys.*, vol. 35, pp. 97–100, 1996.
- [74] V. Badescu and P. T. Landsberg, "Theory of some effects of photon recycling in semiconductors," *Semicond. Sci. Technol.*, vol. 8, pp. 1267–1276, 1993.
- [75] V. Badescu and P. T. Landsberg, "Influence of photon recycling on solar cell efficiencies," *Semicond. Sci. Technol.*, vol. 12, pp. 1491–1497, 1997.
- [76] P. Renauld, F. Raymond, B. Bensaid, and C. Verie, "Influence of photon recycling on lifetime and diffusion coefficient in GaAs," *J. Appl. Phys.*, vol. 71, no. 4, pp. 1907–1913, 1992.
- [77] S. M. Durbin and J. L. Gray, "Numerical modeling of photon recycling in solar cells," *IEEE Trans. Electron. Dev.*, vol. 41, no. 2, pp. 239–245, 1994.
- [78] P. Asbeck, "Self-absorption effect on the radiative lifetime in GaAs-GaAlAs double heterostructures," *J. Appl. Phys.*, vol. 48, no. 2, pp. 820–822, 1977.
- [79] T. Kuriyama, T. Kamiya, and H. Yanai, "Effect of photon recycling on diffusion length and internal quantum efficiency in $\text{Al}_x\text{Ga}_{1-x}\text{As}$ -GaAs heterostructures," *Jpn. J. Appl. Phys.*, vol. 16, pp. 465–477, 1977.
- [80] J. Goldstein, D. Newbury, D. Joy, C. Lyman, P. Echlin, E. Lifshin, L. Sawyer, and J. Michael, *Scanning Electron Microscopy and X-ray Microanalysis*, 3rd Ed., New York: Kluwer Academics, 2003.
- [81] D. R. Lubber and N. M. Haegel, "Direct imaging of electron-beam interaction region," *J. Appl. Phys.*, vol. 99, pp. 083508-1–083508-5, 2006.

- [82] D. Drouin, A. R. Couture, D. Joly, X. Tastet, V. Aimez, and R. Gauvin, “CASINO V2.42 – A fast and easy-to-use modeling tool for scanning electron microscopy and microanalysis users,” *Scanning*, vol. 29, pp. 92–101, 2007.

INITIAL DISTRIBUTION LIST

1. Defense Technical Information Center
Ft. Belvoir, Virginia
2. Dudley Knox Library
Naval Postgraduate School
Monterey, California
3. Dr. Andres Larraza
Naval Postgraduate School
Monterey, California
4. Dr. Nancy Haegel
Naval Postgraduate School
Monterey, California
5. Dr. Craig Smith
Naval Postgraduate School
Monterey, California
6. Dr. Gamani Karunasiri
Naval Postgraduate School
Monterey, California
7. Dr. Sebastian Osswald
Naval Postgraduate School
Monterey, California
8. Dr. Christopher Frenzen
Naval Postgraduate School
Monterey, California
9. LTC David J. Phillips
Naval Postgraduate School
Monterey, California
10. MAJ Kevin Blaine
United States Military Academy
West Point, New York
11. Len Cirignano
Radiation Monitoring Devices
Watertown, Massachusetts

12. Dr. Henry Chen
Redlen Technologies
Saanichton, British Columbia, Canada
13. Dr. Mark Wrobel
Domestic Nuclear Detection Office
Washington, District of Columbia